学位論文

Mechanism of Angular Momentum Transport in Collisional and Collisionless Accretion Disks

（衝突性および無衝突性の降着円盤における
角運動量輸送メカニズムに関する研究）

平成 28 年 12 月博士（理学）申請

東京大学大学院理学系研究科

地球惑星科学専攻

平林　孝太

Abstract

This thesis explores anomalous transport mechanism of angular momentum transport via magnetohydrodinamic (MHD) turbulence driven by magnetorotational instabilities (MRIs) in accretion disks. To trigger mass accretion onto a central compact object and resultant release of gravitational binding energy, which is believed to be an energy source for a wide variety of astrophysical phenomena, the angular momentum of the gas must be transported outwardly; otherwise the matter keeps to rotate around the central object by the strong centrifugal barrier. However, it is known that the classical Spitzer-type viscosity carried by Coulomb collision provides a merely much smaller transport efficiency than an observationally constrained estimate. While Shakura & Sunyaev (1973) successfully advanced accretion disk theories by introducing the well-known α-viscosity, which parameterizes the anomalous turbulent viscosity, the origin of the turbulence sustained in an accretion disk had been unknown for a long time. Since Balbus & Hawley (1991) indicated astrophysical importance of the MRI as a strong driver of MHD turbulence, a number of authors have investigated the nature of the MRI intensively, mainly by nonlinear MHD simulations. We still, however, suffer from discrepancy between transport efficiencies estimated from observations and MHD simulations. In this thesis, the generation of MHD turbulence is discussed by numerical simulations to seek for mechanisms which can further enhance the angular momentum transport. In particular, collisional and collisionless accretion disks are investigated separately.

In chapter 2, we focus on a *collisional* accretion disk, where the standard MHD approximation is applicable. Since a toroidal magnetic field becomes dominant through the so-called Ω-dynamo commonly in a differentially rotating system, it is of importance to investigate local behavior of the gas threaded by external toroidal magnetic flux. While the conventional MRI mode can grow from the seed toroidal field only for essentially vertically propagating waves, we have found that unstable eigenmodes completely confined within an equatorial plane can be present and drive MHD turbulence if the background toroidal flux has radial non-uniformity. This instability is termed a magneto-gradient driven instability (MGDI). It can provide sufficiently large α-viscosity mainly contributed by the Maxwell stress when the imposed toroidal flux is comparable to the saturation amplitude of three-dimensional local MRIs. The MGDI may work as a new possible path to drive MHD turbulence in accretion disks in a complementary manner with the toroidal MRI modes rather than in a competitive manner, and may play a role of significance in

transport process by coupling with magnetic reconnection occurring along the equatorial plane.

In contrast, chapters 3 and 4 are devoted to turbulent transport in *collisionless* accretion disks, where the gas is so dilute that the mean free path of charged particles exceeds the scale size of an accretion disk. In this regime, the standard MHD approximation is no longer valid, and anisotropy in a velocity distribution function plays an important role to transport the angular momentum. Chapter 3 is designed to construct a new numerical framework to deal with this anisotropy precisely, which is interpreted as an anisotropic pressure tensor in a fluid-based model, by extending the classical double adiabatic approximation. By combination of the second-order moment of the Vlasov equation and a gyrotropization model for the pressure tensor, we have successfully developed a new kinetic, scale-free MHD model. In particular, the natural assumption that the gyrotropization rate is proportional to a local magnetic field strength enables us to solve magnetized and unmagnetized regions seamlessly without any numerical difficulty, which cannot be accomplished by the classical model involving singularity at null points. While we apply this model particularly to the problem of accretion disks in this thesis, the application also includes other large-scale collisionless plasmas such as the Earth's magnetosphere and solar winds.

Chapter 4 works on the first approach to large-scale, collisionless disk simulations using the model developed in the previous chapter. Specifically, the local assumption is relaxed in the vertical direction. It yields a *stratified* shearing box model and involves the concept of the disk's scale height, which cannot be resolved by fully kinetic approaches such as particle-in-cell (PIC) and Vlasov simulations. We found that the resultant transport efficiency averaged over the whole simulation domain remains at the same level as that obtained in the standard MHD. The anisotropic stress, however, localizes near the mid-plane with relatively weak vertical gravity and reaches a comparable value to the Maxwell stress, which is consistent with previous work without stratification. This localization indicates the strong dependence of angular momentum transport to the background disk structure when the stress by thermal pressure anisotropy cannot be neglected, and emphasizes the necessity of global simulations in the future, to which our scale-free kinetic MHD model could contribute significantly.

Another result of importance is an enhancement of the Maxwell stress by taking a gyrotropization rate close to a dynamical time scale. Since this parameter is propor-

tional to the magnetic field, a finite non-gyrotropy remains selectively in the vicinity of current sheets, where magnetic reconnection takes place. Our result implies that this non-gyrotropy tends to suppress the magnetic reconnection, which is qualitatively consistent with the test problem of one-dimensional reconnection provided in chapter 3. This suppression effect by non-gyrotropy suggests a mechanism to enhance the angular momentum transport in a different way from the assertion by Hoshino (2013), where the suppression of the magnetic reconnection was explained by parallel pressure enhancement by reconnection itself and only the role of gyrotropic anisotropy was taken into account. While we have to take care of the difference of the suppression mechanisms in PIC and the present kinetic model, this thesis certainly contributes to fill the significant gap between the fully kinetic approach and the existing fluid models, and sheds new light on theoretical understanding of the collisionless accretion disks.

Acknowledgments

I would like to express my special appreciation and thanks to my supervisor Professor Masahiro Hoshino. You have been a tremendous mentor for me. Your encouraging advice both on research as well as on my career have been gracious and invaluable. I would not complete writing this thesis if it were not your successive support and education over my Ph.D. course. I would also like to thank Associate Professor Takanobu Amano. Discussions with you have always been very insightful. Especially your brilliant understanding on a wide range of numerical techniques helped and encouraged me considerably. I want to thank the laboratory members, Dr. Makoto Takamoto and Mr. Masanori Iwamoto, and also to my seniors who graduated our laboratory previously, Dr. Keisuke Shirakawa, Dr. Katsuaki Higashimori and Dr. Tatsuhiko Saito for an enjoyable moment and a fruitful discussion.

A special thanks to my family. Words cannot express how grateful I am to my parents for all of the supports you have made on my behalf. It was your great deal of trust in me that sustained me to strive toward my goal. At the end, thank you to Shiho Taniguchi, for all your love and support.

Contents

1 General Introduction **1**

1.1 Basics of accretion power 1

1.2 Accretion disk models 2

1.2.1 Thin Keplerian disks and α-viscosity 3

1.2.2 Thick disks 5

1.2.3 Slim disks 8

1.2.4 Advection dominated accretion flows (ADAFs) 10

1.2.5 Summary of accretion disk models 12

1.3 Constraints on α 13

1.4 Origin of α-viscosity 16

1.4.1 Magnetorotational instabilities (MRIs) 17

1.4.2 Collisionless MRIs 21

1.5 Goal of this thesis 25

1.5.1 Motivation 25

1.5.2 Structure of this thesis 26

2 Instability of Toroidal Magnetic Field in Collisional Accretion Disks **29**

2.1 Introduction 29

2.2 Linear analysis 31

2.2.1 Equilibrium state and linearized equations 32

2.2.2 Growth rates 33

2.2.3 Eigenfunctions 36

2.3 Nonlinear simulations 39

2.3.1 Basic equations and simulation codes 40

2.3.2 A single localized magnetic field 41

2.3.3 Multiple localized magnetic fields 44
2.4 Discussion and summary 51

3 New Fluid Model for Collisionless Magnetohydrodynamic Simulations with Anisotropic Pressure 53

3.1 Introduction 53
3.2 Formulation 56
3.2.1 Generalized energy conservation law 56
3.2.2 Gyrotropization model 58
3.3 Numerical implementation 61
3.3.1 Conservative part 61
3.3.2 Energy exchange part 64
3.3.3 Effective collision part 64
3.3.4 Summary of the numerical method 65
3.4 Test problems 67
3.4.1 Circularly polarized Alfvén waves 67
3.4.2 Shock tube problem 68
3.4.3 One-dimensional reconnection layer 73
3.4.4 Field loop advection 79
3.4.5 Magnetorotational instability 82
3.5 Discussion and summary 85

4 Stratified Simulations of Collisionless Accretion Disks 89

4.1 Introduction 89
4.2 Simulation setup 92
4.2.1 Basic equations 92
4.2.2 Initial and boundary conditions 93
4.2.3 Code 95
4.3 Results 95
4.3.1 Fiducial run 96
4.3.2 Resolution dependence 105
4.3.3 Dependence on gyrotropization model 106
4.4 Discussion and summary 112

5 General Discussion **117**

5.1 Summary of this thesis 117

5.2 Future prospects 119

A Higher Order Implementation **123**

B Isotropization Model **126**

C Orbital Advection Scheme with Anisotropic Pressure **128**

List of Figures

1.1 Equipotential surfaces in the thick disk model. Each label indicates the value of the normalized effective potential $2\Psi_{eff}/c^2$. Both axes are measured in unit of the Schwarzschild radius $R_S = 2GM/c^2$. 7

1.2 Dependence of temperature for ions and electrons on radial distance from a central black hole, predicted by the advection dominated accretion flow model. Reprinted with permission from Macmillan Publishers Ltd: Narayan et al. (1995) ©1995. 12

1.3 Thermally equilibrium solutions on the $(\dot{M}, \alpha\Sigma)$-plane. Assumed disk parameters are $M/M_\odot = 10$, $R = 5R_S$, and (a) $\alpha = 0.1$ while (b) $\alpha = 0.01$. Reprinted with permission from Abramowicz et al. (1995) ©2016 American Astronomical Society. 13

1.4 Growth rates of the MRI as a function of wave vectors lying on the meridian plane. The Keplerian rotation with $d\ln\Omega/d\ln R = -3/2$ is adopted. The fastest growing mode with $\gamma/\Omega = 3/4$ appears at $\mathbf{k}v_A/\Omega = \pm\left(\sqrt{15}/4\right)\hat{\mathbf{e}}_z$, indicated by white plus signs. 20

1.5 Growth rates of MRIs for various combination of plasma beta, $\beta_{||,\perp} = c^2_{||,\perp}/v_A^2$. Panels (e) and (f) show appearance of the firehose and the mirror instabilities under 5% of pressure anisotropy. 24

2.1 The color contour of growth rates as a function of the plasma beta and the wavenumber normalized by d, which is the width of the localized toroidal field. The gradient of the angular velocity, q, is set to unity. 34

2.2 Schematic view of first-order Lorentz forces. In the left panel, the background current ($\mathbf{J}_0$; gray circles) makes expansive Lorentz force (black arrows) combined with the perturbed magnetic field ($\mathbf{B}_1$; black lines). The resultant force works to increase the perturbation, like shown by the red arrows. In the right panel, on the other hand, a cross product of the first-order current ($\mathbf{J}_1$; black circles), which is generated by the perturbed magnetic field, and the background magnetic field ($\mathbf{B}_0$; gray lines) makes the inward Lorentz force, which always works as the restoring force. 36
2.3 The color contour of growth rates in a rigid-rotating plasma, $q = 0$, with the same format as in Fig. 2.1. 37
2.4 Two-dimensional views of an unstable eigenfunction with the wavenumber $k_y d = 0.223$, superposed on the background plasma with $\beta = 100$. The corresponding growth rate is 0.039Ω. The color contour, the solid lines, and the vector map indicate the gas pressure, the magnetic field lines, and the velocity, respectively. The first-order eigenfunction $\mathbf{U}_1$ is normalized by $|\mathbf{U}_1| = 1$. From left to right, the amplitude of the eigenfunction increases $2e$-fold. 38
2.5 Unstable eigenfunction with $\beta = 10$ and $k_y d = 0.223$. The format is same as in Fig. 2.4. The growth rate is 0.430Ω. 39
2.6 Unstable eigenfunction with $\beta = 1$ and $k_y d = 0.223$. The format is same as in Fig. 2.4. The growth rate is 0.675Ω. 40
2.7 Snapshots of the MHD simulations at twenty times the orbital period. The color contours, solid lines, and arrows represent the gas pressure, the lines of magnetic force, and the in-plane velocity, respectively. 42
2.8 Time histories of the box-averaged stress. The left and right panels show the xy-components of the Reynolds stress and the Maxwell stress normalized by the averaged initial gas pressure, that is, the α parameters. 43
2.9 Snapshots of the simulation started from a wavy toroidal field with $\beta = 100$, taken at 50, 100, and 200 orbits. The format of each panel is the same as in Fig. 2.7. 45
2.10 Snapshots of the case of $\beta = 10$, with the same format as in Fig. 2.9. 46
2.11 Snapshots of the case of $\beta = 1$, with the same format as in Fig. 2.9. 47

2.12 Temporal development of the box-averaged energy divided into the contribution from the x and y directions, all of which are normalized by the gas pressure measured in a magnetized region. Each panel shows the results for (a) $\beta = 100$, (b) $\beta = 10$, and (c) $\beta = 1$, respectively. 48
2.13 The xy-components of the (a) Reynolds and (b) Maxwell stress tensors as functions of time. 49
2.14 The Maxwell stress averaged during the saturated stage as a function of the initial β. 50
2.15 Time histories of the Reynolds and Maxwell stress normalized box averages of the instantaneous gas pressure in the elongated simulation box, $(x, y) \in (2L_x, 4\pi L_x)$, for different initial β. 50

3.1 Brio-Wu shock tube problem under an isotropic MHD limit. The data have been taken at $t = 0.2$. The solid line overplotted in each panel is the reference solution, calculated using the Athena code with 20000 grid points. In the reference run, a Roe approximate Riemann solver, piecewise constant interpolation, and a corner-transport upwind integrator are employed. . . . 70
3.2 Brio-Wu shock tube problem under the gyrotropic MHD limit. The data have been taken at $t = 0.2$. 71
3.3 Brio-Wu shock tube problem with no gyrotropization. The data have been taken at $t = 0.2$. 74
3.4 Results of a one-dimensional Riemann problem set up to imitate a self-similar reconnection layer, assuming fast isotropization. The data have been taken at $t = 3500$ 75
3.5 Results of a one-dimensional Riemann problem set up to imitate a self-similar reconnection layer, assuming fast gyrotropization. The data have been taken at $t = 3500$. 76
3.6 Results for a one-dimensional Riemann problem at $t = 3500$, without inclusion of gyrotropization or isotropization effects. 78
3.7 Results of the one-dimensional Riemann problem at $t = 100$, without inclusion of gyrotropization or isotropization effects. 79
3.8 Snapshot at $t = 2$ for the field-loop advection problem. All variables are normalized by the initial magnetic pressure inside the field loop, $B_0^2/2$. Relatively slow gyrotropization is assumed with $\nu_g = 10\,|B|\,/B_0$. 81

3.9 Volume-averaged energy density and stress, normalized by the initial thermal pressure, as functions of time. The two left-hand panels (a) show the results for an isotropic MHD limit, while the right-hand panels (b) show the results for anisotropic MHD models with pitch-angle scattering. 84

3.10 Slices of the density and pressure anisotropy distributions along $y = 0$ at time $\Omega t/2\pi = 4.2$, just before the largest channel flow structure breaks down. The rightmost panel shows the occurrence frequency as a function of the density and the anisotropy, which demonstrates that the dense current sheet consists of a relatively isotropic plasma or a slightly anisotropic plasma with $P_{||} > P_{\perp}$. 86

4.1 Snapshots during the initial phase of the MRI from Run A32a. The left and right halves in each panel show contours of the mass density and the azimuthal magnetic field, normalized by the mid-plane density and the maximum field strength at the initial state, respectively. 97

4.2 Time variation of α-parameters averaged over the whole simulation domain in Runs A32a (left) and I32 (right). Contribution from Reynolds (blue), Maxwell (green), anisotropic (red, only in the anisotropic run), and total (cyan) stress are plotted with different colors. 99

4.3 Dependence of each stress on instantaneous magnetic energy. The solid lines are results of linear fitting. 100

4.4 Horizontally averaged structure of various quantities in the anisotropic run as functions of vertical position and time in Run A32a. From top to bottom, we plot the plasma beta, the radial magnetic field, the azimuthal magnetic field, the Maxwell stress, and the anisotropic stress. 101

4.5 Spacetime diagrams in the isotropic Run I32 with the same format as in Fig. 4.4. 102

4.6 Comparison of vertical structure of horizontally and temporally averaged stress between Runs A32a and I32. 103

4.7 Horizontally and temporally averaged profiles of the variables related to anisotropic stress, p_{xy}. 104

4.8 Occurrence frequencies of a measure of non-gyrotropy and magnetic field strength, for Runs A32a, A32d and A32e using different gyrotropization frequencies. 107

4.9 Results of the one-dimensional Riemann problem at $t = 3500$ including only the rotation term with $\Omega_{c0} = 10^0$. 109
4.10 Results of the one-dimensional Riemann problem at $t = 3500$ including only the rotation term with $\Omega_{c0} = 10^{-2}$. 110
4.11 Results of the one-dimensional Riemann problem at $t = 3500$ including only the rotation term with $\Omega_{c0} = 10^{-4}$. 110
4.12 Dependence of stress and plasma beta on a gyrotropization and cyclotron frequency. The circles connected with solid lines are the cases with only gyrotropization, and the squares connected with dashed lines indicate the result of the gyrotropization and rotation model. 112
4.13 A schematic picture of a reconnection layer expected in a shearing box simulation. 113

List of Tables

3.1 Circularly polarized Alfvén waves for five periods 69

4.1 Simulation summary 96
4.2 Statistics for Runs A32a and I32 99
4.3 Simulation summary for rotation + gyrotropization model 111

5.1 Summary of simulation studies of MRIs. 120

Chapter 1

General Introduction

1.1 Basics of accretion power

Accretion disks are one of the most ubiquitous astrophysical objects, where gravitational binding energy of an accretion flow is converted into heat, radiation, and in some cases, directed bulk flows. In general, the more massive and the more compact the central object is, the more efficiently the accretion disk can extract energy from the accreted matter. Thus many of the highly energetic astrophysical phenomena are thought to involve accretion flows at the center of which a neutron star (NS) or a black hole (BH) is present. To make a rough estimate, let us consider an accreted element with mass m onto a central body of mass M and radius R_*. The gravitational potential released through the accretion process onto the surface of the central object is

$$\Delta E_{acc} = \frac{GMm}{R_*}. \tag{1.1}$$

In the case of a NS with $R_* \sim 10$ km and solar mass $M \sim M_\odot$, equation (1.1) shows that the released energy per accreted mass is

$$\frac{\Delta E_{acc}}{m} \sim 0.15c^2 \sim 1.3 \times 10^{20} \text{ erg/g}.$$

The same estimate for a stellar mass BH yields a rather larger value, $\Delta E_{acc}/m \sim 0.49c^2$, but with the surface radius of the central body replaced by the Schwarzschild radius $R_* = 2GM/c^2 \sim 3(M/M_\odot)$ km. This is an order-of-magnitude estimate, and a reasonable guess for the case of a stellar mass BH appears to be $\sim 0.1c^2$. Anyway, by comparison

with another energy production process, for example, nuclear reaction, which can provide at most $\Delta E_{nuc}/m \sim 0.007c^2$ attained in hydrogen burning, the above rough estimates of conversion efficiency suggest that an accretion disk does work as a quite powerful engine to fuel a luminous object.

The released energy in accreted matter will ultimately be radiated away from a system in a wide range of wavebands, except for the energy dragged by matter swallowed up at the event horizon of a BH. The predicted shape of a spectrum emitted from each accreting object strongly depends on an applied accretion disk model. However, a classical maximum luminosity, integrated over all wavelengths, may not depend on the accretion model under the assumption of a steady and spherically symmetric accretion flow. Suppose the accreted gas consists of a fully ionized proton-electron plasma. The gas at the distance r from the central object is gravitationally pulled inward with the force $f_{in} = GM\left(m_p + m_e\right)/r^2 \simeq GMm_p/r^2$, where m_p and m_e are the proton and electron masses, respectively. On the other hand, the radiant energy flux $S = L/4\pi r^2$ emitted spherically from the accreting object with the luminosity L imposes radial momentum upon the gas through scattering processes. The exerted force arises mainly by Thomson scattering of free electrons with the cross-section σ_T, which results in the outward force $f_{out} = \sigma_T S/c$. This force apparently acts on the electrons, but the ions are also dragged by the accelerated electrons due to the strong electrostatic Coulomb force between them. By balancing the inward and the outward forces, then, we obtain a critical luminosity

$$L_{Edd} = \frac{4\pi GMm_p c}{\sigma_T} \simeq 1.3 \times 10^{38} \left(\frac{M}{M_\odot}\right) \text{ erg/s}. \tag{1.2}$$

This limiting value is the so-called classical Eddington luminosity, at the luminosity above which accreted matter will be blown off by too strong radiation pressure, and a steady accretion flow cannot be accomplished. In spite of a lot of simplification, the Eddington limit has played a role to explain observed luminosity of accreting BHs like quasars, and has been of great importance to provide us standard candles.

1.2 Accretion disk models

The spherically symmetric accretion flow mentioned in the previous section occurs only when accreted gas, which should be provided from a companion star in a binary system and from a host galaxy or an intergalactic medium in an active galactic nucleus, possesses

little angular momentum; it is natural that an axisymmetric accretion *disk* will arise preferentially, rather than an accretion *sphere*. There has been proposed various kinds of accretion disk models in the literature. In this section we briefly review some of the representative models by focusing ourselves to steady accretion flow solutions according to which terms are dominant in a radial momentum equation following Frank et al. (2002).

Let us consider a steady, axisymmetric flow in a cylindrical coordinate system (R, ϕ, z). Suppose the toroidal or azimuthal velocity is described purely by rotation, $v_\phi = R\Omega$, where Ω is the angular velocity as a function of R and z. The momentum equation for the remaining poloidal component of the velocity $\mathbf{v}_p = (v_R, v_z)$ (we require $v_R < 0$ for accretion) is something as follows:

$$(\mathbf{v}_p \cdot \nabla)\, \mathbf{v}_p = -\frac{1}{\rho}\nabla P - \nabla\Phi + \Omega^2 R\hat{\mathbf{e}}_R + (\nabla \cdot \sigma)_p\,, \tag{1.3}$$

with the mass density ρ, the sum of the thermal and radiation pressures P, the gravitational potential Φ, and the stress tensor σ. Although the last stress term related to a dissipation process has great importance, in particular, when discussing an energy equation using the balance between heating and cooling effects, we will neglect its dynamical role. A further assumption we make here is that the gravitational potential is dominated by contribution from the central star; in other words, the total mass of the accreted matter is sufficiently smaller than that of the central object. This simplification allows us to set the functional form of Φ *a priori*. By keeping in equation (1.3) at least two dominant terms which always include gravity, we will classify several accretion disk models in the following sections.

1.2.1 Thin Keplerian disks and α-viscosity

The first obvious solution arises when only the effects of advection and gravity are kept; $(\mathbf{v}_p \cdot \nabla)\, \mathbf{v_p} = -\nabla\Phi$. This corresponds to simple gravitational collapse, or free fall of matter onto a central attractor. Another natural solution involves stars and stellar envelopes, where the gravity is supported purely by the pressure gradient force; $0 = -\rho\nabla\Phi - \nabla P$, i.e., in hydrostatic equilibrium.

An important disk solution appears in the case that the gravity is radially balanced by the centrifugal force (e.g., Shakura & Sunyaev, 1973; Lynden-Bell & Pringle, 1974;

Pringle, 1981),

$$0 = -\frac{\partial}{\partial R}\left(\frac{GM}{\sqrt{R^2+z^2}}\right) + \Omega^2 R, \tag{1.4}$$

where we have made use of the assumption of a light disk. At this point, let the disk being geometrically thin, which requires $|z| \ll R$. Then the radial momentum equation (1.4) yields the Keplerian rotation, $\Omega = \sqrt{GM/R^3}$. Considering the vertical force balance, on the other hand, since the centrifugal force acts only in the radial direction, we retain the pressure gradient to support the gravity. Denoting the typical scale height of the disk H, we may set $|\partial P/\partial z| \sim P/H$. The z-component of equation (1.3) results in the relation

$$\frac{1}{\rho}\frac{P}{H} \sim \frac{GM}{R^3}H = \Omega^2 H.$$

If we define the speed of sound $c_s = \sqrt{P/\rho}$ and the azimuthal Mach number $\mathcal{M}_\phi = v_\phi/c_s$, we finally obtain

$$\frac{H}{R} \sim \frac{c_s}{v_\phi} \sim \mathcal{M}^{-1} \ll 1.$$

This relation shows that the geometrically thin assumption requires that the local Keplerian velocity is highly supersonic, which is clearly a constraint on the temperature strongly dependent on heating and cooling mechanisms. In many cases this requirement is satisfied, but at the inner region of the disk, for example, where irradiation from a central object raises the local temperature, the thin disk approximation will break down.

In the remaining of this section, we shall make mention of the radial, or accretion, velocity, and its connection with viscous physics. Suppose small perturbative poloidal velocity $\mathbf{v}_p$ in equation (1.3) deviated from the equilibrium described by equation (1.4). With the radial pressure gradient neglected, and under the axisymmetry, the R-component of the momentum equation yields

$$v_R\frac{\partial v_R}{\partial R} = \frac{1}{\rho}\left[\frac{\partial \sigma_{RR}}{\partial R} + \frac{\sigma_{RR}-\sigma_{\phi\phi}}{R} + \frac{\partial \sigma_{Rz}}{\partial z}\right], \tag{1.5}$$

where the viscous stress are

$$\sigma_{RR} = 2\rho\nu\frac{\partial v_R}{\partial R}, \quad \sigma_{\phi\phi} = 2\rho\nu\frac{v_R}{R}, \quad \sigma_{Rz} = \rho\nu\left(\frac{\partial v_z}{\partial R} + \frac{\partial v_R}{\partial z}\right),$$

with the kinematic viscosity in the accreted matter ν. In an order-of-magnitude estimate, therefore, we obtain $v_R \sim \nu/R$ using the reasonable assumption that $v_z \sim (H/R)\, v_R \ll v_R$.

1.2.1.1 α-viscosity model

Thus far, we did not concern any physical mechanism to determine a specific value of the viscosity ν. It is known that applying classical molecular viscosity (Spitzer, 1956) evaluated using typical parameters expected in an accretion flow yields a radial velocity v_R, which is directly connected with an accretion rate $\dot{M} = 2\pi R \int (-\rho v_R)\, dz$, much smaller than estimates on observational grounds. In order to make further advances in accretion theories without entering deeply into the physics of the required anomalous viscosity, Shakura & Sunyaev (1973) introduced crude parameterization where the viscosity is assumed to be proportional to the product of a local speed of sound and a typical scale height;

$$\nu = \alpha c_s H. \tag{1.6}$$

This is the noted "α-viscosity" model. The non-dimensional coefficient α is a model parameter describing the magnitude of the viscous transport of momentum and, in particular, angular momentum. In practical applications, $0 < \alpha < 1$ is assumed generally; otherwise a too large viscous drift velocity could lead to formation of shock waves and the picture of a steady accretion flow cannot be associated any longer. We shall leave some more issues on this α-viscosity to sections 1.3 and 1.4, and here we finally note the estimate on the radial velocity

$$v_R \;\sim\; \alpha c_s \frac{H}{R} \;\sim\; \alpha c_s \mathcal{M}^{-1} \ll c_s,$$

which shows that v_R is small in the thin disk approximation self-consistently.

1.2.2 Thick disks

If two different terms, in addition to the gravity, are kept in equation (1.3), we get three types of solutions: Bondi accretion, thick disks, and slim disks. Bondi accretion is a spherically symmetric accretion flow, which is obtained with the centrifugal force omitted (Bondi, 1952). In this solution, matter within the Bondi radius, at which the escape velocity from a central object $v_{esc} = \sqrt{2GM/R}$ coincides with the thermal speed of particles $v_{th} \sim c_s$, accretes directly without a substantial centrifugal barrier. This and the following

subsections are devoted to describe other *disk* solutions.

Suppose that a rotating cloud is supported by pressure gradient force;

$$\frac{1}{\rho}\nabla P = -\nabla\Phi + \Omega^2 R\hat{\mathbf{e}}_R \equiv \mathbf{g}_{eff}, \tag{1.7}$$

where $\mathbf{g}_{eff}$ is the effective gravity defined as the sum of the gravitational force and the centrifugal force. Equation (1.7) implies that, if the cloud is embedded in an external medium of constant pressure, the effective gravity becomes perpendicular to the isosurface of the pressure everywhere. By expressing the isosurface by $z_s = z_s(R)$ as a function of the radial position, and combining the definition of the effective gravity and the orthogonality $\mathbf{g}_{eff} \cdot d\mathbf{s} = 0$, where $d\mathbf{s}$ is a line element along the isosurface, we obtain

$$\Omega^2(R, z_s) R = \left(\frac{\partial\Phi}{\partial R}\right)_s + \left(\frac{\partial\Phi}{\partial z}\right)_s \frac{\partial z_s}{\partial R}, \tag{1.8}$$

where $()_s$ indicates differentiation along $d\mathbf{s}$. If we assume again that the cloud does not contribute to the gravitational potential significantly, equation (1.8) provides us the relation between the surface of constant pressure and the rotation profile of the cloud; once the geometry of the isosurface z_s is given, one can immediately obtain the angular velocity $\Omega(R, z_s)$ by solving equation (1.8), and vice versa.

For an illustrative purpose, let us consider the case that an equation for a certain cross-section of the disk is given by a straight line with an elevation angle θ, i.e., let us assume $z_s(R) = \pm R\tan\theta$, and the gravitational potential is that of the point mass, $\Phi = -GM/r$, where $r = \sqrt{R^2 + z^2}$ is the distance from the central point mass M. Keeping in mind that Φ must be differentiated along the surface, we obtain from equation (1.8)

$$\Omega^2(R, z_s) = \frac{GM\cos\theta}{R^3}.$$

Note that this is the Keplerian rotation, but corresponding to the reduced mass $M\cos\theta$. If we take $\theta \to 0$, we retain the thin Keplerian disk discussed in section 1.2.1. By the further assumption that the angular velocity is vertically constant in the disk, $\Omega = \Omega(R)$, the above rotation profile can be extended to the entire disk, which allows us to define the effective potential

$$\Psi_{eff} = \Phi - \int^R \Omega^2(\xi)\,\xi\, d\xi, \tag{1.9}$$

such that $\mathbf{g}_{eff} = -\nabla\Psi_{eff}$ and $\Psi_{eff} = 0$ on the surface z_s. Then we can draw the equipotential surfaces Ψ_{eff} = constant, which are, as already mentioned, identical to the isosurfaces of the pressure. The picture of the stratification is sketched in Fig. 1.1, where several equipotential surfaces are shown by solid lines. In particular, the shaded region with $\Psi_{eff} < 0$ corresponds to the geometrically thick disk with $H \sim R$, contrary to the previous thin disk, where the short scale height $H \ll R$ was initially assumed. The discussion here is a special case of the theory of rotating masses. See Tassoul (1978, 2000) for a good summary.

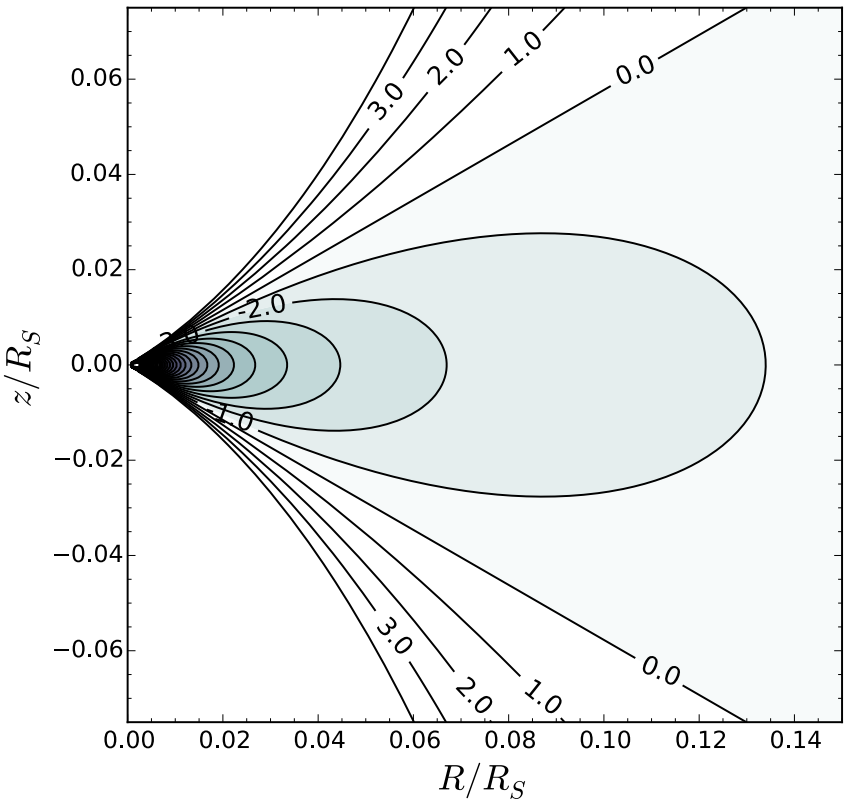

Figure 1.1: Equipotential surfaces in the thick disk model. Each label indicates the value of the normalized effective potential $2\Psi_{eff}/c^2$. Both axes are measured in unit of the Schwarzschild radius $R_S = 2GM/c^2$.

If we allow a small poloidal velocity superposed on the thick disk model, and if the α-viscosity is responsible for the radial drift, equation (1.6) holds again. In this case, however, because of the large thickness of the disk $H \sim R$, the requirement of a subsonic accretion flow implies $\alpha \ll 1$, which is more severe restriction than in the thin disk model. In thick disks, in general, α would be more like a function of both R and z than a spatially uniform constant; nevertheless, there has been no accepted model which enables specific

choice of such viscosity.

1.2.3 Slim disks

Another type of solutions arises when a substantial radial velocity is assumed. This solution is called a *slim* disk, in the sense that the geometrical thickness of the disk is small $H < R$ for a relatively small accretion rate, while the thickness approaches $H \sim R$ when the accretion rate is near, or slightly larger than, the critical value $\dot{M}_{crit}$, at which the luminosity reaches the Eddington limit. This moderately super-Eddington model was first proposed in Abramowicz et al. (1988), on which most part of the following discussion is based. Recent progress by Sądowski (2009) extended the slim disk solution so that it can be applied to Kerr BHs.

In the previous two models, i.e., the geometrically thin and thick disks, we implicitly assumed that thermal energy generated by viscous heating is eventually radiated away from the disk at the same rate as the heating rate in a steady state. The dominant effect of advection due to nonnegligible v_R in the slim disk solution, however, allows the dissipated heat to be advected and carried away from the disk, which provides another cooling mechanism. To make an estimate of the condition that the advective cooling rate Q_{adv} dominates the radiative cooling rate Q_{rad}, let us consider the vertically integrated energy balance,

$$Q_{vis} = Q_{adv} + Q_{rad},$$

where Q_{vis} is the dissipation rate by viscosity per unit surface area. Denoting the surface density by $\Sigma = \int \rho dz$, and assuming optically thick emission, we roughly obtain

$$Q_{vis} \simeq \nu\Sigma \left(R\frac{\partial\Omega}{\partial R} \right)^2, \tag{1.10}$$

$$Q_{adv} \simeq \frac{\dot{M}}{2\pi R^2} c_s^2, \tag{1.11}$$

$$Q_{rad} \simeq \frac{4\sigma T_c^4}{3\kappa_R \Sigma}, \tag{1.12}$$

where $\dot{M} = 2\pi R\Sigma(-v_R)$ is an accretion rate, T_c is a mid-disk temperature, σ is the Stefan-Boltzmann constant, and κ_R is the Rosseland mean opacity. These estimates suggest that, if the accretion rate satisfies $\dot{M} > \left(8\pi\sigma T_c^4 c_s^2 / 3\kappa_R \Sigma\right) R^2$, the advection cooling works dominantly and the structure should be modified from the standard thin disk approximation.

In this sense, the slim disk is a more general model of the optically thick, geometrically thin Keplerian disk extended to all accretion rates, and has been associated with bright objects whose luminosities are close to or above the Eddington values.

The spatial structure of a slim disk for specific values of $\dot{M}$, α, and so on, are, in general, calculated numerically, so here we shall only show a simple equation to describe the relation between the rotation profile $\Omega(R)$ and the surface density $\Sigma(R)$. Taking the toroidal component of the momentum equation yields

$$\frac{v_R}{R}\frac{\partial\left(R^2\Omega\right)}{\partial R}+v_z\frac{\partial\left(R\Omega\right)}{\partial z}=\frac{1}{\rho}\left[\frac{1}{R^2}\frac{\partial\left(R^2\sigma_{R\phi}\right)}{\partial R}+\frac{\partial\sigma_{\phi z}}{\partial R}\right], \tag{1.13}$$

where

$$\sigma_{R\phi}=\rho\nu R\frac{\partial\Omega}{\partial R},\quad \sigma_{\phi z}=\rho\nu\frac{\partial\left(R\Omega\right)}{\partial z}.$$

Under the condition of rotation on cylinders $\Omega=\Omega(R)$, which is a reasonable assumption in many cases, integrating equation (1.13) vertically leads to

$$\left(\Sigma v_R R\right)\frac{\partial\left(R^2\Omega\right)}{\partial R}=\frac{\partial}{\partial R}\left(\nu\Sigma R^3\frac{\partial\Omega}{\partial R}\right).$$

By noticing that the inside of the leftmost parentheses is proportional to the accretion rate $\dot{M}$ and is constant from the equation of continuity, this equation can be further integrated by R as follows

$$\left[-2\pi\nu\Sigma R^3\frac{\partial\Omega}{\partial R}\right]_{R_{\rm in}}^{R}=\dot{M}\left(R^2\Omega-R_{\rm in}^2\Omega_{\rm in}\right)=\dot{M}\left(l-l_{\rm in}\right),$$

where l is the specific angular momentum, and the subscript "in" indicates the value at the inner edge of the disk. If no torque is exerted at the inner edge, i.e., $\left(\partial\Omega/\partial R\right)_{\rm in}=0$, as in the case of an accreting BH, we finally obtain

$$-2\pi\nu\Sigma\frac{\partial\ln\Omega}{\partial\ln R}=\dot{M}\left(1-\frac{l_{\rm in}}{l}\right). \tag{1.14}$$

Combined with the vertically integrated equations for poloidal momentum and energy balance, and with appropriate boundary conditions, this relation is integrated to determine the rotation profile in the slim disk.

1.2.4 Advection dominated accretion flows (ADAFs)

The last model we discuss here is an advection dominated accretion flow (ADAF), which appears when all terms in the momentum equation are retained. The ADAF solution was first predicted by Ichimaru (1977). As its name indicates, the viscous heating rate Q_{vis} is balanced by the advection cooling Q_{adv}, as well as in slim disks. The major difference is that an accretion rate assumed in the ADAF is relatively small, contrary to a rate more or less close to the critical value in the slim disk. A smaller $\dot{M}$ simply results in a smaller surface density, and in turn, an optically thin disk with $\tau < 1$ arises in this regime.

Suppose that the fraction f of the viscously generated energy is advected before radiated away. The energy equation is then (see equations (1.11) and (1.10))

$$\frac{\dot{M}}{2\pi R^2} c_s^2 = f\nu\Sigma \left(R\frac{\partial\Omega}{\partial R} \right)^2 . \tag{1.15}$$

This relation and three conservation laws of mass, momentum, and angular momentum determine the radial profiles of Ω, v_R, Σ, and c_s^2 completely, with the help of the α-viscosity model; $\nu = \alpha c_s H = \alpha c_s^2/\Omega_K$, where Ω_K is a Keplerian angular velocity. Under the assumption of power-law dependence on R for four variables, one can obtain the simple relations (Narayan & Yi, 1994)

$$v_R \propto R^{-1/2}, \quad \Sigma \propto R^{-1/2}, \quad c_s^2 \propto R^{-1} \quad \text{and} \quad \Omega \propto R^{-3/2}.$$

More detailed analysis for seeking a full set of solutions reveals that $c_s = \tilde{c} v_\phi$ with, in general, $\tilde{c} \simeq 1$, which implies $H \simeq R$, since $c_s/v_\phi = \mathcal{M}^{-1} \sim H/R$. Thus the ADAF is a geometrically thick accretion disk; the difference from the thick disk model previously discussed in section 1.2.2 is a non-vanishing radial velocity $v_R = \tilde{v} v_\phi$ with $\tilde{v} \simeq 1$.

1.2.4.1 Collisionless accretion disks

The low surface density in the ADAF has given rise to the idea of *collisionless* accretion disks. If we assume that the energy exchange between protons and electrons is due to the Coulomb collision, its timescale can be estimated by

$$t_E\,(i\text{-}e) \simeq \left(\frac{m_p}{m_e} \right) \frac{m_e^{1/2}\,(kT)^{3/2}}{2\pi N e^4 \ln\Lambda},$$

where $m_{p,e}$, k, T, N, e, and $\ln\Lambda$ denote the proton and electron mass, the Boltzmann constant, the temperature, the number density, the elementary charge, and the Coulomb logarithm, respectively. This timescale is compared with the infall time $t_{infall} = R/v_R \simeq R/\left(\alpha c_s^2/v_\phi\right)$. Taking the ratio between these two timescales, and assuming some typical values, viz., $T \sim 10^{10}$K, $\ln\Lambda \simeq 20$, $R = 3R_S$, and $c_s \sim v_{th}$, we obtain

$$\frac{t_E\,(i\text{-}e)}{t_{infall}} \;\sim\; 3\times 10^{10}\,\frac{\alpha}{N}\left(\frac{M}{4\times 10^6 M_\odot}\right)^{-1}, \tag{1.16}$$

with N measured in unit of cm^{-3}. The mass is normalized by the value for the BH at the Galactic center, Sagitarius A* (Sgr A*), whose mass has been confirmed by a number of astronomical observations based on, for example, motions of gas surrounding Sgr A* (e.g., Wollman et al., 1977), and motions of stars (e.g., Genzel et al., 1996; Schödel et al., 2002; Ghez et al., 2003). Equation (1.16) suggests that, when $\alpha \simeq 0.1$, for example, sufficient relaxation between ions and electrons cannot occur before the entropy is gotten rid of by advection if $N \lesssim 10^9$cm^{-3}. Then the resultant disk may become a two-temperature ADAF. In this sense, it is a collisionless system for the ion-electron collision. The condition for collisionless behavior for electron-electron and ion-ion collision requires more severe constraints by factors of (m_p/m_e) and $(m_p/m_e)^{1/2}$, respectively.

Fig. 1.2 shows the radial dependence of the ion and electron temperatures $T_{i,e}$ predicted from the framework of the two-temperature ADAF model, reproduced with permission from Narayan et al. (1995). At large radii outside 10^3 times the Schwarzschild radius R_S, the ions and the electrons well couple with each other via Coulomb collision, and have the almost equal virial temperature. As we move to inner orbits $R < 10^2 R_S$, on the other hand, the electrons cool efficiently mainly by the optically thin synchrotron emission and the inverse Compton scattering, while the ions keep their virial temperature. Thus we naturally get a large temperature difference $T_i \gg T_e$, which implies that the gas pressure is dominated by the ion contribution, and therefore, only a small deviation of the ion pressure from its thermal equilibrium, e.g., anisotropy and off-diagonal components in a pressure tensor, can have a non-negligible dynamical role on the disk behavior. We will investigate the impact of this effect on accretion flows in detail in Chapter 4.

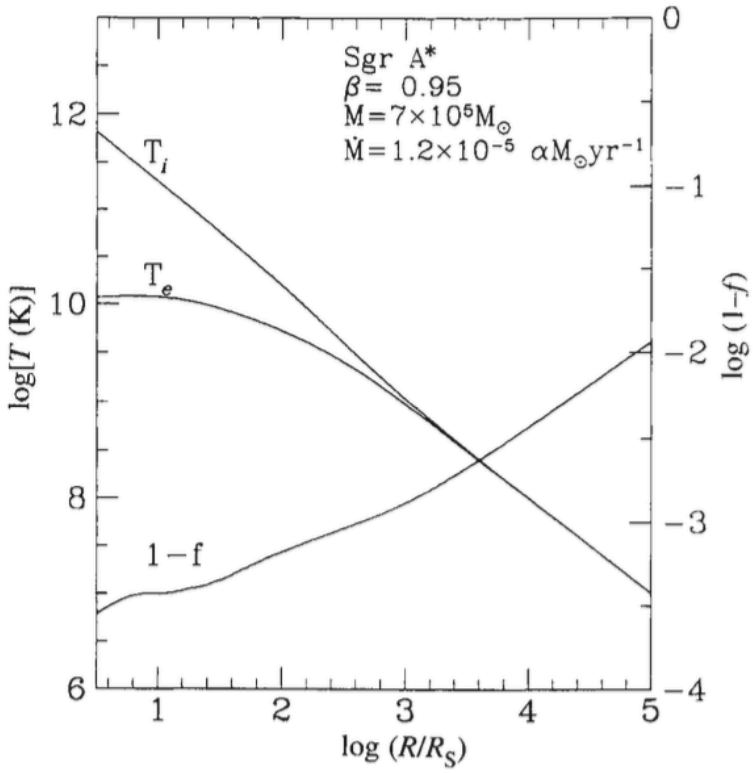

Figure 1.2: Dependence of temperature for ions and electrons on radial distance from a central black hole, predicted by the advection dominated accretion flow model. Reprinted with permission from Macmillan Publishers Ltd: Narayan et al. (1995) ©1995.

1.2.5 Summary of accretion disk models

To summarize this section on the accretion theories, we show several thermally equilibrium disks on the $(\dot{M}, \alpha\Sigma)$-plane in Fig. 1.3 reprinted with permission from Abramowicz et al. (1995). Fundamental assumptions made in this figure are as follows: opacity is given by electron scattering, radiation cooling is due to bremsstrahlung emission, and disk parameters are $M = 10M_{\odot}$, $R = 5R_S$, and (a) $\alpha = 0.1$ or (b) $\alpha = 0.01$. Other minor differences from the discussion in this section would lead to no qualitative changes. Optically thick and optically thin accretion disk solutions are shown by the right solid S-shaped curve and the left solid curve, respectively. The optically thick branch can be further separated into two stable solutions with positive slopes. The branch at an intermediate accretion rate sandwitched by two stable branches is viscously and thermally unstable and breaks up into discrete rings by small perturbation. The lower branch corresponds to the thin Keplerian disk, while the upper one belongs to the slim disk model. The left optically thin equilibrium, on the other hand, shows an ADAF solution. However, the branch corresponding to a lower accretion rate for a certain surface density suffers from a thermal

instability. Thus only the upper equilibrium would be present in nature. For more details on the thermal and viscous instabilities, see Lightman & Eardley (1974); Piran (1978); Ciesielski et al. (2012) for example.

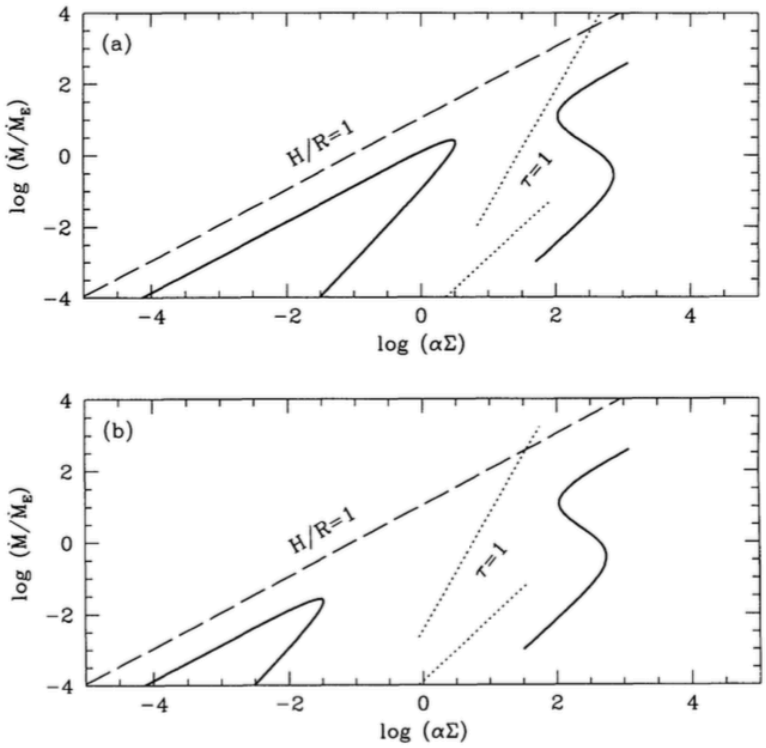

Figure 1.3: Thermally equilibrium solutions on the $(\dot{M}, \alpha\Sigma)$-plane. Assumed disk parameters are $M/M_\odot = 10$, $R = 5R_S$, and (a) $\alpha = 0.1$ while (b) $\alpha = 0.01$. Reprinted with permission from Abramowicz et al. (1995) ©2016 American Astronomical Society.

1.3 Constraints on α

The steady thin Keplerian disk model has achieved great success in explaining observed characteristics of many systems. It is mainly because the most properties in the thin disk model show fairly weak dependence on an actual value of α. In the solution derived by Shakura & Sunyaev (1973), for example, $T_c \propto \alpha^{-1/5}$ for the mid-plane temperature, $\tau \propto \alpha^{-4/5}$ for the optical thickness, and all other variables also have the power indices less than unity. Ignorance of the detailed physics related to viscosiy, therefore, does not lead to any severe divergence of the resulting α-disk solutions. This fact, on the other hand, gives rise to a limitation on the direct way to determine α; an estimate on α from observations inevitably involves a large extent of uncertainty, as long as we make use of the steady disk structure to compare with observed properties, because similar values of

α lead to quite similar structures. Thus, to find a reliable value of α on the observational ground, time-dependent phenomena should be handled apparently.

One class of such phenomena is dwarf nova outbursts, which belong to a subclass of cataclysmic variables, and repeat sudden increase and decrease in luminosity within the timescale of 10-3000 days (Warner, 2003). This outburst is considered to arise in association with transition between cool, poorly ionized state and hot, highly ionized state of an accretion disk in a close binary system possessing a white dwarf. Since the hot state disk evolves with the viscous timescale

$$t_{vis} \sim \frac{R^2}{\nu}, \tag{1.17}$$

by measuring the time taken by transition from the outburst light curves, a reasonable estimate on an underlying value of α can be made, if the disk geometry and the disk temperature are known from other observational efforts. Based on several different techniques and different objects, all papers in the literature conclude that α in hot phases must be in the similar range $\alpha \simeq 0.1$–0.3 (e.g., Smak, 1998, 1999; Buat-Ménard et al., 2001; Schreiber et al., 2003).

Another class of candidates from which information on viscous process may be extracted is outburst of soft X-ray transients (SXTs), which have longer duration compared with the dwarf nova case. The SXT outburst possesses a BH or a NS as the central accreting object rather than a white dwarf, so the SXT outbursts are observed in low-mass X-ray binaries. It would be possible that strong X-rays emitted from the central region irradiate the outer part of the accretion disk. King & Ritter (1998) proposed that this irradiation may keep the most part of the disk in hot, highly ionized state while brightening with large luminosity, until substantial mass of the disk have accreted. This model naturally explains long duration of SXT outbursts. From detailed analysis of light curves, the viscosity required for SXT outbursts are estimated to lie within $\alpha \simeq 0.2$–0.4 (Dubus et al., 2001). These two estimates from dwarf nova and SXT outbursts are in good agreement that $\alpha \simeq 0.1$–0.4 is required to explain the transient phenomena within the framework of the standard thin disk model.

When we focus on optically thin ADAFs like Sgr A*, on the other hand, $\alpha < 0.1$ might be concluded from consideration about the maximum luminosity. A correspondence of the optically thin ADAF for a stellar mass BH is likely to have the maximum luminosity of

a few per cent of its Eddington limit (Zdziarski et al., 2004). This value is sufficiently smaller than the theoretical largest luminosity inferred from Fig. 1.3 for $\alpha = 0.1$ and several assumptions (Abramowicz et al., 1995), which implies $\alpha \gtrsim 0.1$ may not be necessarily required to explain the observed luminosity. However, there still remains an expectation for rather large α from a theoretical point of view for another population of disks. Some active galactic nuclei (AGNs), such as blazars, are thought to be combination of accretion disks and collimated relativistic jets emanated from the central objects with the bulk Lorentz factors ranging roughly within 10–100 (e.g., Marscher, 2006), while the formation of moderate non-relativistic jets has been theoretically obtained in global magetohydrodynamic (MHD) simulations of optically thin BH accretion flows (e.g., Machida et al., 2000, 2001). Observations of some AGNs imply that the energy output exceeds the Eddington limit of the BH, which suggests an underlying mechanism of very efficient energy conversion from the input rest mass energy into jets. Blandford-Znajek (BZ) process is one of the plausible mechanisms to achieve such a high conversion rate by extracting the rotation energy of the central BH and to produce an ultra-relativistic flow (Blandford & Znajek, 1977). For BZ process to operate, however, it is required to keep a substantial magnetic field around the rotation axis of the central BH, which should be rapidly dragged along with the accreting matter from the surrounding disk. Apparently this rapid concentration of the magnetic flux is driven by efficient angular momentum transport, and the actual efficiency in an AGN is a controversial issue.

Tchekhovskoy et al. (2011) demonstrated by their general relativistic MHD simulations that if large-scale magnetic flux is dragged efficiently toward the black hole, a jet with an extremely high energy conversion rate may be generated by a magnetically arrested disk (MAD; Narayan et al., 2003). To achieve the MAD state, where $\alpha \gtrsim 0.1$ is expected (e.g., McKinney et al., 2014), they assumed in their simulations rapid advection of the magnetic flux via more efficient angular momentum transport in a geometrically thick ADAF-like disk than in a standard thin disk. Note that there have been attempts to obtain efficient transport of the angular momentum with the help of large-scale magnetic fields rather than local behavior as in the picture of local α-prescription. Matsumoto et al. (1996), for example, showed by two-dimensional global MHD simulations without radiation that if the accretion disk is threaded by a large-scale magnetic field parallel to the rotation axis, the differential rotation of the disk generates torsional Alfvén waves emitted along the field lines, which efficiently carry the angular momentum away from the disk. Nowadays

this mechanism is known as magnetic braking, where the large-scale magnetic field plays a role of importance. Another example is fully three-dimensional study of global accretion disks including vertical magnetic flux by Suzuki & Inutsuka (2014). They reported inward dragging of the vertical magnetic field intensively around the surface regions, which would also contribute to rapid concentration of the field. Nevertheless, it is still an open question whether or not such efficient transport can be sustained by a process of high compatibility with the description of α-viscosity, which is expected to be related to local, or small-scale, behavior.

1.4 Origin of α-viscosity

In section 1.2, we have reviewed several accretion disk models. In particular, the viscosity was assumed to be proportional both to the local speed of sound and to the disk scale height, together with a dimensionless parameter α (cf. equation (1.6)). The α-viscosity is useful to obtain a closure of the set of equations without going into details of background viscous physics. It is, however, equally of great significance to disclose the physical mechanism(s) which can produce the required anomalous viscosity, and to validate, quantify, and if needed, modify the α-prescription.

Another role of critical importance played by viscosity is efficient transport of angular momentum, which was implicitly assumed in all the accretion flow models. In fact, for accretion to occur, the angular momentum must be transported outwardly and eventually extracted from the accreted matter; otherwise the conserved angular momentum would yield a substantial centrifugal barrier as the matter falls inward, and the outward force would be inevitably balanced against the attraction of central gravity at the radius

$$r = \frac{l^2}{GM},$$

with the specific angular momentum l. Once the viscosity is given by equation (1.6), the efficiency of the angular momentum transport in the radial direction, which is described by the $R\phi$–component of the stress tensor, can be expressed as

$$\sigma_{R\phi} = \rho\nu R\frac{\partial\Omega}{\partial R} \simeq \alpha P. \tag{1.18}$$

1.4.1 Magnetorotational instabilities (MRIs)

After the realization that simple molecular viscosity cannot provide sufficient α required to explain observational values, the origin of the strong viscosity has been sought for in turbulent motion driven by instabilities in a shearing medium (e.g., Lynden-Bell & Pringle, 1974; Pringle, 1981). In spite of various attempts, however, hydrodynamic shear flow instabilities have failed to lead to a highly turbulent accretion disk. The major problem was the Rayleigh criteria for stability

$$\frac{\partial}{\partial R}\left(R\Omega^2\right) > 0, \tag{1.19}$$

which shows that a differentially rotating medium is unstable only if the specific angular momentum decreases outwardly; most accretion flows satisfy the stability condition.

A radical change of the stability criteria occurs when the effect of a magnetic field is taken into account. The MHD instability in a weakly magnetized, differentially rotating plasma, first discussed by Velikov (1959) and Chandrasekhar (1960), was *rediscovered* to be a potential source of turbulence in the astrophysical context (Balbus & Hawley, 1991). By linear analysis, this instability, which is known as the magnetorotational instability (MRI) nowadays, is shown to be able to grow within the rotational timescale of the disk Ω^{-1}, if the angular velocity decreases outwardly. Namely the stability criteria in the MHD is

$$\frac{\partial \Omega}{\partial R} > 0, \tag{1.20}$$

contrary to equation (1.19) in the hydrodynamic case. Subsequent studies using fully-nonlinear numerical simulations (e.g., Hawley & Balbus, 1991, 1992; Hawley et al., 1995), furthermore, show that the MRI can surely be a powerful driver of MHD turbulence in its saturated stage. In this section, the basic properties and the physical picture of the MRI are illustrated.

We employ the ideal MHD approximation with a polytropic equation of state under

the effect of gravity of a central point mass. The basic equations are then as follows:

$$\frac{\partial \rho}{\partial t} + (\rho \mathbf{v}) = 0, \tag{1.21}$$

$$\rho \left(\frac{\partial \mathbf{v}}{\partial t} + \mathbf{v} \cdot \nabla \mathbf{v} \right) = -\nabla \left(P + \frac{B^2}{8\pi} \right) + \frac{\mathbf{B} \cdot \nabla \mathbf{B}}{4\pi} - \nabla \Phi, \tag{1.22}$$

$$\frac{\partial \mathbf{B}}{\partial t} = \nabla \times (\mathbf{v} \times \mathbf{B}), \tag{1.23}$$

$$P \propto \rho^{\gamma}, \tag{1.24}$$

where γ is a polytropic index and other notations are standard. Let us confine ourselves to considering the local behavior of the MRI, that is, suppose a typical lengthscale of a disturbance under consideration, λ, is much smaller than the radial distance; $\lambda/R \ll 1$. This assumption invokes a shearing box model, which will be used later in chapters 2 and 4. By picking up a fiducial radius R_0, and moving on to the frame of reference co-rotating with the orbital motion at R_0, equation (1.22) can be rewritten in the local Cartesian coordinates as follows

$$\frac{\partial \mathbf{v}}{\partial t} + \mathbf{v} \cdot \nabla \mathbf{v} = -\frac{1}{\rho} \nabla \left(P + \frac{B^2}{8\pi} \right) + \frac{\mathbf{B} \cdot \nabla \mathbf{B}}{4\pi\rho} - 2\mathbf{\Omega} \times \mathbf{v} + 2q\Omega^2 x \hat{\mathbf{e}}_x, \tag{1.25}$$

where $\mathbf{\Omega} = \Omega \hat{\mathbf{e}}_z$ is the angular velocity vector measured at $R = R_0$, $x = R - R_0$ is the radial distance from the fiducial radius, and $q = -d \ln \Omega / d \ln R$ is the power index of a given rotation profile, $\Omega \propto R^{-q}$. The vertical component of the gravity is omitted for simplicity. The differential rotation is then described in this system by a linearly varying velocity $\mathbf{v}_0 = -q\Omega x \hat{\mathbf{e}}_y$.

1.4.1.1 Linear dispersion

Suppose that a plasma of the uniform mass density ρ_0 and thermal pressure P_0, rotating with $\mathbf{v}_0$, is threaded by a weak vertical magnetic field $\mathbf{B} = B_0 \hat{\mathbf{e}}_z$, which is an equilibrium state in the shearing box. As in the standard procedure of linear analysis, we divide each variable into the equilibrium value and the small deviation from it, like $X = X_0 + X_1$. By keeping only first order terms, and by expanding them into plane waves propagating on the meridian plane, i.e., $X_1 \propto \exp(-i\omega t + i\mathbf{k} \cdot \mathbf{x})$ with $\mathbf{k} = k_x \hat{\mathbf{e}}_x + k_z \hat{\mathbf{e}}_z$, the basic equations in the form of partial differential equations are converted into linear algebraic equations about ρ_1, $\mathbf{v}_1$, $\mathbf{B}_1$, and P_1. Eventually, they can be reduced to a single dispersion formula

to relate the frequency ω and the wavenumber $\mathbf{k}$,

$$\begin{aligned}\left(\omega^2 - k_z^2 v_A^2\right)\left(\omega^4 - k^2\left(c_s^2 + v_A^2\right)\omega^2 + k^2 k_z^2 c_s^2 v_A^2\right) \\ = \left(\omega^2 - k_z^2 c_s^2\right)\left(\kappa^2\omega^2 - k_z^2 v_A^2 \frac{d\Omega^2}{d\ln R}\right),\end{aligned} \tag{1.26}$$

where $v_A = B_0/\sqrt{4\pi\rho_0}$ is the Alfvén velocity, and κ is the epicyclic frequency, such that $\kappa^2 = 4\Omega^2 + d\Omega^2/d\ln R$. Note that, in the non-rotating case with the right-hand side vanished, equation (1.26) just tells the dispersion relation of MHD waves in a uniform medium.

It is useful to take the incompressible approximation by assuming $c_s^2 \gg (\omega/k)^2, v_A^2$, the consistency of which will be justified *a posteriori* after we find growth rates of the MRI. Then the dispersion relation can be further reduced to

$$\left(\frac{\omega}{\cos\theta}\right)^4 - \left(\kappa^2 + 2k^2 v_A^2\right)\left(\frac{\omega}{\cos\theta}\right)^2 + k^2 v_A^2\left(k^2 v_A^2 + \frac{d\Omega^2}{d\ln R}\right) = 0, \tag{1.27}$$

where $\theta = \cos^{-1}(k_z/k)$ is the angle between the magnetic field and the direction of the wave propagation. Once the rotation profile is given, this equation can be solved analytically to find an exponentially growing, unstable solution with $\omega^2 < 0$. The growth rates of the unstable modes under the Keplerian rotation, $q \equiv -d\ln\Omega/d\ln R = 3/2$, are illustrated in Fig. 1.4 on the (k_x, k_z)-plane. The MRIs appear for wavenumbers which satisfy $k^2 v_A^2 < 2q\Omega^2$ for any propagation angle, but the parallel mode with $\theta \simeq 0$ grows faster than oblique or perpendicular modes. The maximum growth rate,

$$\frac{\gamma_{max}}{\Omega} = \frac{q}{\sqrt{2q\Omega + (\kappa^2/\Omega^2)}} = \frac{3}{4}, \tag{1.28}$$

occurs at the wavenumber satisfying

$$\frac{k_{max} v_A}{\Omega} = \sqrt{q\frac{\kappa^2 + q\Omega^2}{\kappa^2 + 2q\Omega^2}} = \frac{\sqrt{15}}{4}, \tag{1.29}$$

and, we have obtained $\mathcal{O}\left(\omega^2/k^2\right) \sim \mathcal{O}\left(v_A^2\right)$, which validates the incompressible assumption made above, when $c_s^2 \gg v_A^2$. The stability condition $k^2 v_A^2 > 2q\Omega^2$ implies that, if q is a negative number, the MRI modes cannot be present. Thus the stability criteria in a differentially rotating, magnetized medium becomes equation (1.20), as we expected.

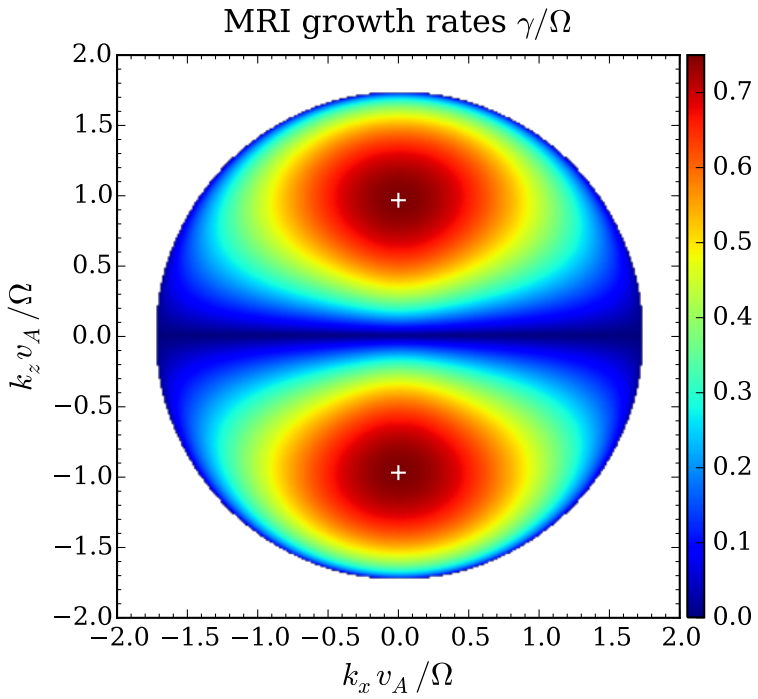

Figure 1.4: Growth rates of the MRI as a function of wave vectors lying on the meridian plane. The Keplerian rotation with $d\ln\Omega/d\ln R = -3/2$ is adopted. The fastest growing mode with $\gamma/\Omega = 3/4$ appears at $\mathbf{k}v_A/\Omega = \pm\left(\sqrt{15}/4\right)\hat{\mathbf{e}}_z$, indicated by white plus signs.

1.4.1.2 Nonlinear simulations

The linear theory successfully predicts the presence of instabilities in a differentially rotating medium. To make a quantitative estimate of proper values of α provided by MRI-driven MHD turbulence, however, three-dimensional fully-nonlinear numerical simulations are required. Hawley et al. (1995) performed a series of local shearing box simulations including externally imposed B_z, and showed that the strong MRI-driven turbulence leads to $\alpha \sim \mathcal{O}\,(0.01\text{-}0.1)$ depending on the magnitude of the imposed magnetic flux. This value of α is calculated by the net angular momentum transport due to turbulent stress,

$$\langle \sigma_{R\phi} \rangle = \alpha P = \langle \rho v_x \left(v_y - v_{y0}\right) \rangle + \left\langle -\frac{B_x B_y}{4\pi} \right\rangle, \tag{1.30}$$

where $\langle \cdot \rangle$ denotes an ensemble average. It is in general agreement that, in MRI-driven turbulence, the great body of α is carried by the Maxwell stress related to magnetic tension force, rather than the Reynolds stress arising from bulk motion. This configuration with an external B_z has been furthered by many subsequent publications, and a scaling law

to make an empirical estimate for *isothermal* gas is suggested as $\alpha \sim 2\pi\beta_z^{-1/2}$, where $\beta_z = 8\pi P/B_z^2$ is a plasma beta measured by the gas pressure and the initially assumed vertical magnetic field (Sano et al., 2004; Pessah et al., 2007). In the case of adiabatic gas, the resultant α becomes smaller by one or two orders of magnitude when normalized by gradually increasing thermal pressure.

It appears that α obtained from the shearing box simulations with net vertical magnetic flux is sufficient to explain observed values if the equation of state is close to isothermal and β_z ranges around 250–4000. There is, however, no obvious ground for the presence of such an external magnetic field threading an accretion disk, and thus it would be more appropriate to consider a local domain with no net magnetic flux. There also have been zero-net-flux simulations by a number of authors with and without vertical gravity (e.g., Brandenburg et al., 1995; Stone et al., 1996; Sano et al., 2004; Davis et al., 2010), and, unfortunately, almost all papers report the values of α smaller than observations by at least one order of magnitude, $\alpha \lesssim 0.02$. It is, therefore, still an open question whether or not the magnetorotational instability is really able to produce a sufficient rate of angular momentum transport in fully-ionized, collisional accretion disks.

1.4.2 Collisionless MRIs

As already discussed in section 1.2.4 and section 1.3, there is a strong implication of collisionless accretion disks on both observational and theoretical grounds. The low-collisionality of accreted matter leads to significant deviation from its thermal equilibrium state, which means the standard MHD approach taken in previous studies becomes no longer valid. The first attempt to investigate the nature of angular momentum transport in a collisionless disk beyond the standard MHD description was made by Quataert et al. (2002), where kinetic theory was applied to the MRI with wavelength much longer than the proton Larmor radius. They assumed a gyrotropic pressure tensor with the form of

$$\mathbf{p} = p_\perp \mathbf{I} + \left(p_{||} - p_\perp\right) \hat{\mathbf{b}}\hat{\mathbf{b}}, \tag{1.31}$$

where $p_{||,\perp}$ denote the pressures measured in the direction parallel and perpendicular to a local magnetic field, $\mathbf{I}$ is the unit tensor, and $\hat{\mathbf{b}} = \mathbf{B}/B$ is the unit vector directed to the magnetic field. By combining this pressure with the second moment of the linearized drift-kinetic equation (e.g., Snyder et al., 1997), they confirmed the linear growth of kinetic

MRIs, the properties of which largely depend on the orientation of the magnetic field and the wavevector, and also on the ratio of the gas pressure to the magnetic pressure. The key issues of the kinetic MRI are the destabilization effect and additional angular momentum transport via anisotropic pressure gradient force, which is not present in MHD.

For the purpose of illustrating the impact of anisotropic pressure on linear growth of MRIs, let us consider a simplified case; we adopt the double adiabatic equations of state to describe the linear response of $p_{||}$ and $p_\perp$ (Chew et al., 1956; Kulsrud, 1983) instead of self-consistent kinetic treatment,

$$\rho B \frac{D}{Dt}\left(\frac{p_\perp}{\rho B}\right) = -\nabla\cdot\mathbf{q}_\perp - q_\perp \nabla\cdot\hat{\mathbf{b}} = 0, \tag{1.32}$$

$$\frac{\rho^3}{B^2}\frac{D}{Dt}\left(\frac{p_{||}B^2}{\rho^3}\right) = -\nabla\cdot\mathbf{q}_{||} + 2q_\perp \nabla\cdot\hat{\mathbf{b}} = 0, \tag{1.33}$$

which are obtained by the neglect of heat flux in the kinetic MHD, $\mathbf{q}_\perp$ and $\mathbf{q}_{||}$. Following the procedure described in section 1.4.1, in particular for the parallel mode with $\theta = 0$, we obtain quite similar dispersion relation,

$$\omega^4 - \left(\kappa^2 + 2\varepsilon k^2 v_A^2\right)\omega^2 + \varepsilon k^2 v_A^2\left(\varepsilon k^2 v_A^2 + \frac{d\Omega^2}{d\ln R}\right) = 0, \tag{1.34}$$

where $\varepsilon = 1 - 4\pi\left(p_{||} - p_\perp\right)/B^2$ is a dimensionless parameter to characterize anisotropy of the background velocity distribution function. This equation is the almost same one as equation (1.27) except that the Alfvén speed v_A is replaced by a modified value $\sqrt{\varepsilon}v_A$. This fact implies that a change in ε simply elongates (shortens) an unstable wavelength of the MRI for $\varepsilon < 1$ ($\varepsilon > 1$), while the maximum growth rate remains at a same value. This is because the effective magnetic tension force under an anisotropic pressure is corrected by a factor of ε. For small ε, centrifugal force of fast particle motion along a bent magnetic field line tends to reduce the original tension force. Under the opposite anisotropy, on the other hand, fast cyclotron motion makes the line of magnetic force more rigid.

Showing behavior of oblique modes requires more general treatment, which includes the effect of compressibility explicitly, and the effect of heat flux as well. We adopt the

Landau closure model (e.g., Snyder et al., 1997),

$$q_{||} = -\sqrt{\frac{8}{\pi}}\rho_0 c_{||0}\frac{ik_{||}\left(p_{||}/\rho\right)}{\left|k_{||}\right|}, \tag{1.35}$$

$$q_{\perp} = -\sqrt{\frac{2}{\pi}}\rho_0 c_{||0}\frac{ik_{||}\left(p_{\perp}/\rho\right)}{\left|k_{||}\right|} + \sqrt{\frac{2}{\pi}}c_{||0}\frac{p_{\perp 0}}{B_0}\left(1-\frac{p_{\perp 0}}{p_{||0}}\right)\frac{ik_{||}B}{\left|k_{||}\right|}, \tag{1.36}$$

which can correctly capture the *linear* Landau dumping. Fig. 1.5 illustrates linear growth rates for various combination of $\beta_{||}$ and $\beta_{\perp}$, which are defined as ratios of phase speeds rather than pressures, with the same format as in Fig. 1.4. Panels (a) and (b) compare the dependence on β. In spite of the isotropic pressure, i.e. $\beta_{||} = \beta_{\perp}$, the highly unstable regimes are squeezed along the magnetic field, especially for the high-β case, where the difference in the linear response between the parallel and perpendicular pressures is reflected more significantly. As mentioned in the case of the parallel and adiabatic mode, panels (c) and (d) show the shifts of unstable wavelengths. Note that the maximum growth rate takes the same value $\gamma = 0.75\Omega$ among these four cases. Panel (e) shows the appearance of a different unstable mode for a negative ε, which is the firehose instability modulated by the differential rotation. Panel (f), on the other hand, represents another instability in the oblique direction occurring under opposite anisotropy, i.e., the mirror instability. It is not surprising that the firehose and the mirror instabilities exhibit larger growth rates without bound as the wavenumber increases, because any stabilizing effect, such as finite Larmor radius effect or pitch-angle scattering, is not included in the present system.

To make further quantitative discussion, Sharma et al. (2006) performed a series of nonlinear simulations of the collisionless MRI with the kinetic MHD framework, paying special attention to the angular momentum transport due to the anisotropic pressure gradient force. They employed the shearing box model threaded by an externally imposed vertical magnetic field without vertical gravity. Although the collisionless MRI has quite different properties from those in the collisional regime, their simulations reveal that the total efficiency of the angular momentum transport is qualitatively similar to that in the standard MHD, while α maintained by anisotropic pressure stress reaches a value comparable to the magnetic stress. Note that, under the assumption of a gyrotropic pressure tensor, the transport efficiency of the angular momentum can be written as

$$\langle\sigma_{R\phi}\rangle = \alpha P = \langle\rho v_x\left(v_y - v_{y0}\right)\rangle + \left\langle -\frac{B_x B_y}{4\pi}\right\rangle + \left\langle\left(p_{||}-p_{\perp}\right)\frac{B_x B_y}{B^2}\right\rangle. \tag{1.37}$$

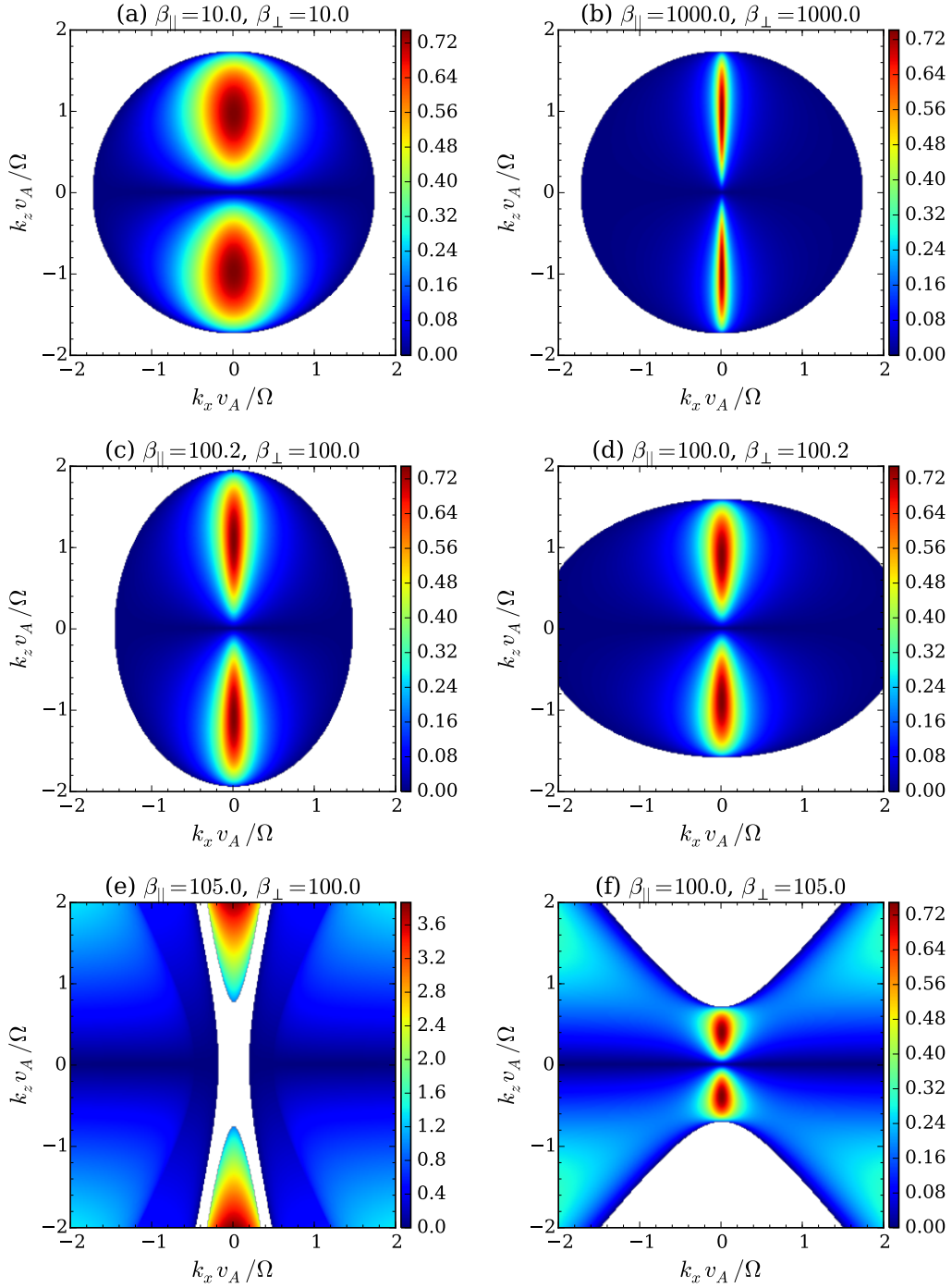

Figure 1.5: Growth rates of MRIs for various combination of plasma beta, $\beta_{||,\perp} = c^2_{||,\perp}/v^2_A$. Panels (e) and (f) show appearance of the firehose and the mirror instabilities under 5% of pressure anisotropy.

The results, however, still involve a lot of uncertainty. Examples include dependence on the isotropization model they assumed, which is related to micro-instabilities expected to occur in an anisotropic plasma, turbulence intensity achieved without external magnetic

flux, the effect of radial and vertical stratification, and the influence of boundless increase in thermal energy resulting from exclusion of all possible cooling mechanisms.

Meanwhile, recent increase in computational power has enabled us to solve the kinetic equation self-consistently by means of the particle-in-cell (PIC) method, where a velocity distribution function is represented by an ensemble average of Lagrangian particles. Two-dimensional full PIC [1] (Riquelme et al., 2012; Hoshino, 2013) and hybrid PIC [2] (Kunz et al., 2014; Shirakawa & Hoshino, 2014) simulations have been reported in this context, and the growth of MRIs in a collisionless shearing plasma is generally confirmed. For quantitative investigation of MRI-driven turbulence, however, three-dimensional calculation is apparently required. The only report adequate for estimates of α during the saturated stage of the MRI was given by Hoshino (2015), where they solved the three-dimensional shearing box without stratification using a full PIC code. They demonstrate that the rate of angular momentum transport is enhanced in collisionless MRI turbulence to the order of $\alpha \sim \mathcal{O}(0.1)$ even when normalized by gradually increasing instantaneous pressure. This α is larger than values measured in the same way both in standard and kinetic MHD simulations without cooling mechanism by at least one order of magnitude. While MHD simulations employing an isothermal equation of state happen to predict similar values of $\alpha \sim \mathcal{O}(0.1)$ for the same range of an initial plasma beta $\beta \sim 10^3$ (Sano & Inutsuka, 2001; Minoshima et al., 2015), the relation with the kinetic study is quite ambiguous. It is also unknown whether the high efficiency of transport in collisionless MRI turbulence can be maintained without externally imposed magnetic flux.

1.5 Goal of this thesis

1.5.1 Motivation

In this chapter, we have reviewed that the progress in accretion disk theories largely relies on the crude assumption of α-viscosity. The underlying physics of turbulence hidden behind the α-viscosity has been gradually disclosed since the rediscovery of the magnetorotational instability, with the great help of numerical simulations. As we already discussed, however, there is still large amount of uncertainty in theoretical estimates on α, which strongly depend on the magnetic configuration and strength, presence of the vertical grav-

[1] Both ions and electrons are treated as discrete particles.

[2] Ions are treated as particles, while electrons are fluid with large or infinite mobility to ensure the charge neutrality.

ity, an equation of state, collisionality, and so on. In addition, we have a substantial discrepancy between observationally estimated values and those obtained from MHD simulations. In that sense, we have not yet reached full agreement about the mechanism of the angular momentum transport in accretion disks. Motivated by the theoretical insufficiency of turbulent viscosity, in the prior part of this thesis, we will seek a new possible path to drive MHD turbulence in a differential rotating plasma, which could contribute to the angular momentum transport in addition to the MRI.

In collisionless disks expected to realize in ADAFs, on the other hand, PIC and kinetic MHD simulations shows that the anisotropic pressure gradient force seems to contribute to the angular momentum transport to the extent comparable to the contribution of the Maxwell stress. In particular, the PIC simulations demonstrate a possibility for MRI turbulence in the collisionless regime to provide sufficiently large viscosity close to an observationally expected level. Nevertheless, to the same degree or more than in the collisional disk cases, substantial theoretical uncertainty that must be elucidated remains. In the posterior part of this thesis, we will tackle numerical investigation to give new insight into the transport process of angular momentum in collisionless disks from the viewpoint of large-scale dynamics. In particular, we focus ourselves on the effect of vertical disk structure, or the stratification, by inclusion of the vertical component of the gravity. For this purpose, the fully kinetic approach, like a PIC simulation, is unable to be applied, because there is a large scale gap between disk scales which are of interest and kinetic scales to be resolved in kinetic simulations. Instead, we adopt a variant of the kinetic MHD model. The fluid-based approach, which possesses a scale-free property as in the standard MHD, gives us a powerful tool to study the large-scale behavior of the collisionless disks. We will work out the role of an anisotropic pressure tensor in the context of viscous and transport process, and furthermore, make attempts to give an integrated knowledge.

1.5.2 Structure of this thesis

This thesis consists of five chapters. Here in chapter 1, we provide general introduction related to various accretion disk theories, the role of α-viscosity in them, and its possible origin. In chapter 2, we propose a new type of instability which is expected to occur in collisional accretion disks dominated by toroidal magnetic field, to compete/cooperate with the conventional MRIs, and to contribute to the angular momentum transport. Results in this chapter is reported in Hirabayashi & Hoshino (2016). Chapter 3 explains our numeri-

cal technique newly developed to carry out collisionless MHD simulations accompanied by sufficient test problems, most part of which is published in Hirabayashi et al. (2016). By using the method introduced in chapter 3, we discuss the angular momentum transport in collisionless accretion disks in the framework of local shearing box including the effect of vertical gravity in chapter 4. This is the first attempt to approach the large-scale dynamics of collisionless disks. Finally, chapter 5 is devoted to general discussion and concluding remarks.

Chapter 2

Instability of Toroidal Magnetic Field in Collisional Accretion Disks

2.1 Introduction

Accretion disks are one of the most ubiquitous astrophysical objects, comprising dynamics such as astrophysical jets, disk winds, and particle acceleration. It is widely believed that these dynamical phenomena are driven by the anomalous transport of angular momentum and the subsequent release of gravitational binding energy. Several mechanisms have been proposed in attempts to explain the origin of this angular momentum transport. Examples include magnetic braking by external, large-scale magnetic fields (e.g., Blandford & Payne, 1982; Stone & Norman, 1994), non-axisymmetric wave excitation (e.g., Fragile & Blaes, 2008), and hydrodynamic/hydromagnetic turbulence (e.g., Papaloizou & Pringle, 1984; Balbus & Hawley, 1998). In this chapter, we consider a mechanism related to the third example, which is the sole candidate that possesses a high correlation with conventional α-viscosity model (Shakura & Sunyaev, 1973). In the α-viscosity model, the efficiency of angular momentum transport, which is determined by the $R\phi$-component of the stress tensor, is determined as the product of the pressure and a given parameter α. The value of α depends significantly on viscosity physics, but the simple molecular viscosity in an accretion disk cannot provide a high efficiency of angular momentum transport suggested by observations (Cannizzo et al., 1988). Since the astrophysical importance of

magnetorotational instability (MRI) as the origin of required turbulence was pointed out (Balbus & Hawley, 1991, 1998), a number of authors have investigated the nature of MRIs and the resultant turbulence in accretion disks over a wide range of plasma parameters (e.g., Stone et al., 1996; Sano & Stone, 2002; Kunz & Lesur, 2013; Hoshino, 2015; Bai, 2015; Zhu et al., 2015; Simon & Hawley, 2009; Simon et al., 2012).

In order to study the basic behavior behind the nonlinear time evolution of MRIs, most numerical studies on the local properties of MRI-induced turbulence have adopted the shearing box model (Hawley et al., 1995; Sano & Inutsuka, 2001; Sharma et al., 2006), which can capture the wave vector toward an arbitrary direction in a differentially rotating plasma. Since an MRI with a vertical wave vector has the maximum growth rate for an axisymmetric perturbation when the background magnetic field is purely poloidal, fully three-dimensional simulations, or at least two-dimensional ones including a vertical axis, are necessary. (Note that the final states in two- and three-dimensional cases are rather different from each other, and that the three-dimensional simulations are required to investigate the saturation stage.)

The situation is similar when the unperturbed magnetic field is purely toroidal. For example, Balbus & Hawley (1992) investigated the linear stability of an accretion disk threaded by a uniform toroidal magnetic field assuming three-dimensional wavevectors in the cylindrical coordinates, whose R-component varies with time because of the background shear velocity. They showed that the perturbation satisfying $\mathbf{k} \cdot \mathbf{V}_A \lesssim \Omega$ can become unstable, in the sense that the amplitude of oscillation increases with time. Moreover, a finite vertical wavenumber, k_z, is required for the instability to occur, and the larger k_z leads to the faster amplification. The nonlinear evolution of this oscillatory instability was also examined by Hawley et al. (1995) using three-dimensional ideal MHD simulations, and the contribution to turbulence generation was confirmed.

Other examples include linear eigenvalue analyses and the corresponding MHD simulations by Matsumoto & Tajima (1995). They revealed that purely growing eigenmodes can exist in a shearing plasma, in contrast to the above oscillatory unstable modes. For a Keplerian disk, only the non-axisymmetric perturbations with $k_y^2/k_z^2 < 0.015$ become purely growing modes, where k_y and k_z are the azimuthal and vertical wavenumbers, respectively. The vertical waves, therefore, again contribute to the unstable modes most significantly, although a finite azimuthal wavenumber is required.

Such a situation, where the toroidal magnetic field is dominant, is thought to appear

easily in the nonlinear stage of an MRI even when starting from a poloidal field. For understanding the dynamics and the nature of turbulence in well-developed disks, therefore, it should be important to investigate a plasma stability under a purely toroidal field. On the other hand, the toroidal magnetic field is subject to parasitic instabilities such as a Kelvin-Helmholtz and a tearing instabilities, which is expected to induce spatially non-uniform magnetic field. We found that, once the non-uniformity in a toroidal field is taken into account, a new type of unstable modes which does not require any finite k_z appears, in contrast to the previous studies that always required $k_z^2 > k_y^2$ under a uniform field. In this chapter, we provide the results of linear and nonlinear analyses on this issue, and suggest another possible path leading to turbulence generation. We will call the unstable modes proposed here as "magneto-gradient driven instability (MGDI)" reflecting its driving source as shown in the succeeding sections. An instability bound to the equatorial plane may play a crucial role in plasma transport, as it could potentially couple with magnetic reconnection occurring in the plane and contribute to the saturation mechanism of MRIs.

The outline of this chapter is as follows. In section 2.2, we briefly introduce the setup of our theoretical study and show the existence of unstable eigenmodes by linear analysis. Section 2.3 discusses the results of the fully-nonlinear two-dimensional numerical simulations. The nonlinear calculations corresponding to the linear study and ones which can lead to more turbulent states are presented. Finally, section 2.4 is devoted to the summary and conclusion of our results.

2.2 Linear analysis

In this section we investigate the linear stability of a non-uniform toroidal magnetic field in a differentially rotating plasma. In particular, a simplified situation with a localized toroidal magnetic field channel is considered to extract the physical essence of underlying unstable modes.

2.2.1 Equilibrium state and linearized equations

The ideal MHD equations incorporated with the standard shearing box model are employed as the basic equations (Stone & Gardiner, 2010):

$$\frac{\partial \rho}{\partial t} + \mathbf{v} \cdot \nabla \rho = -\rho \nabla \cdot \mathbf{v}, \tag{2.1}$$

$$\rho \left(\frac{\partial \mathbf{v}}{\partial t} + \mathbf{v} \cdot \nabla \mathbf{v} \right) = -\nabla \left(p + \frac{B^2}{2} \right) + \mathbf{B} \cdot \nabla \mathbf{B} - 2\rho \mathbf{\Omega} \times \mathbf{v} - 2\rho \Omega x v'_{y0} \hat{\mathbf{e}}_x, \tag{2.2}$$

$$\frac{\partial \mathbf{B}}{\partial t} = \nabla \times (\mathbf{v} \times \mathbf{B}), \tag{2.3}$$

$$\frac{\partial p}{\partial t} + \mathbf{v} \cdot \nabla p = -\gamma p \nabla \cdot \mathbf{v}. \tag{2.4}$$

The radial and azimuthal directions are then interpreted as the x- and y-axes in the local Cartesian coordinate system, where the differential rotation is described by a linearly changing background velocity defined as $v_{y0}(x) = -q\Omega x$, using an angular velocity at the center of the computational domain, Ω, and a positive constant, q. Since $\cdot'$ denotes the radial dirivative, $v'_{y0} = -q\Omega$ is a constant. Note that the factor $1/\sqrt{4\pi}$ is absorbed into the definition of a magnetic field. The specific heat ratio, γ, is set to be $5/3$, and the other notations are standard.

When a purely toroidal magnetic field is imposed, the background shearing plasma is kept in an equilibrium state as long as the total pressure is spatially constant. We can, therefore, choose an arbitrary magnetic structure with a finite gradient. Here, we focus on the idealized case with a simple localized toroidal field,

$$B_{y0}(x) = B_0 \cosh^{-2}(x/d), \tag{2.5}$$

where B_0 is the field strength at $x = 0$ and d is the typical width of the localized field. The gas pressure is determined so as to satisfy the total pressure balance, and the background density is distributed so as to keep the temperature uniform.

Next, we linearize the MHD equations around this equilibrium state, assuming the functional form of a small perturbation as

$$f_1(x, y, t) = f_1(x) \exp(-i\omega t + ik_y y). \tag{2.6}$$

The vertical dependence is ignored to pick up horizontally confined modes. Using the vector potential instead of the magnetic field, linearization of the basic equations leads to

the following eigenvalue problem:

$$\omega \mathbf{U}_1 = \mathbf{M}\mathbf{U}_1, \tag{2.7}$$

where $\mathbf{U}_1 = (v_{x1} \;\; v_{y1} \;\; A_{z1} \;\; p_1)^T$ is a first-order perturbation vector, and $\mathbf{M}$ is a coefficient matrix whose components are given as follows,

$$\mathbf{M} = k_y v_{y0}\mathbf{I} + \mathbf{D},$$

$$\mathbf{D} = \begin{pmatrix} 0 & 2i\Omega & D_{13} & -(i/\rho_0)\,\partial_x \\ D_{21} & 0 & -k_y B'_{y0}/\rho_0 & k_y/\rho_0 \\ iB_{y0} & 0 & 0 & 0 \\ D_{41} & \gamma k_y p_0 & 0 & 0 \end{pmatrix},$$

$$D_{13} = (i/\rho_0)\left[B_{y0}\left(\partial_x^2 - k_y^2\right) + B'_{y0}\partial_x\right],$$

$$D_{21} = -iv'_{y0} - 2i\Omega,$$

$$D_{41} = -ip'_0 - i\gamma p_0 \partial_x.$$

Here, $\mathbf{I}$ is the identity matrix, and ∂_x and $\cdot'$ indicate differentiation operators by x. Note that the equations for v_{z1} and B_{z1} are decoupled as ordinary shear Alfvén waves. Although the density perturbation, ρ_1, appears to disappear from the basic equations, compressional modes remain in the system and ρ_1 can be obtained passively from $\nabla \cdot \mathbf{v}_1$.

Finally, equation (2.7) is discretized in the computational domain $|x/L_x| \leq 1$ with 400 grid points using a fourth-order central difference. The width of the localized field is set to be $d = 0.05L_x$. As a boundary condition, a conducting wall is assumed at $|x/L_x| = 1$. The eigenvalues, ω, and the eigenvectors, $\mathbf{U}_1$, are then computed numerically.

2.2.2 Growth rates

From our calculations of the eigenvalue problem described above, we obtained at most one growing mode of the MGDI for each particular wavenumber. The results are summarized in Fig. 2.1, where the color contour shows the imaginary parts of the eigenvalues as a function of the wavenumber, normalized by the width of the localized field, and the plasma beta, $\beta = 2p/B^2$, measured at $x = 0$. Note that the real parts are zero in a machine precision.

Fig. 2.1 indicates that the purely growing mode appears if β is lower than about 100, and that the growth rate becomes larger with the initial magnetic field strength. When β

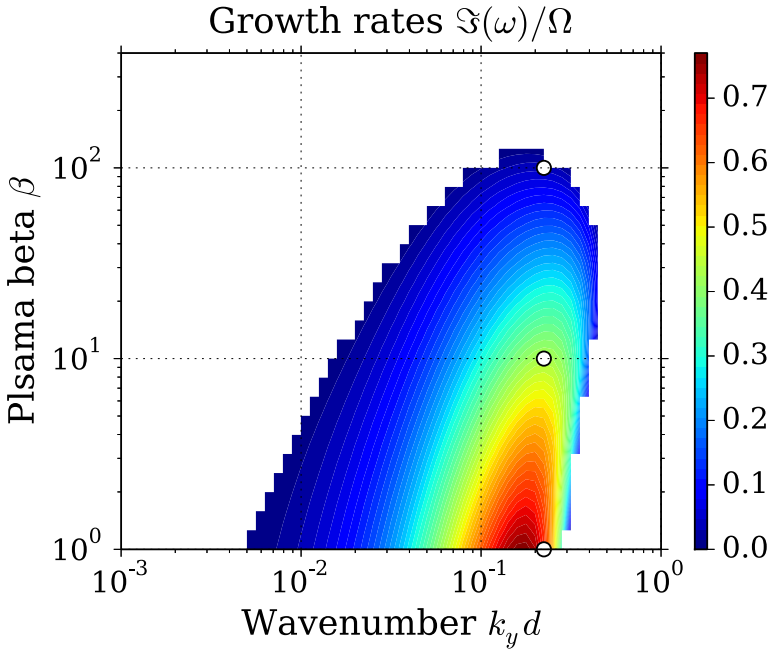

Figure 2.1: The color contour of growth rates as a function of the plasma beta and the wavenumber normalized by d, which is the width of the localized toroidal field. The gradient of the angular velocity, q, is set to unity.

is equal to unity, the maximum growth rate reaches 0.765Ω, which is comparable to that of the axisymmetric MRI, i.e., 0.75Ω, as far as the linear approximation is appropriate. We emphasize here that the magnitude of the velocity shear, q, is assumed to be unity in Fig. 2.1 for theoretical simplicity, which is smaller than in the case of Keplerian rotation, where $q = 1.5$. In the Keplerian rotation case, we expect more unstable eigenmodes due to the stronger shear motion.

A physical picture of the MGDI can be explained as follows. Let us consider an outward going perturbation in v_{x1} away from $x = 0$, i.e., positive for $x > 0$ and negative for $x < 0$. Since the linearized equation for the azimuthal magnetic field can be written as

$$\frac{dB_{y1}}{dt} = -B_{y0}\frac{\partial v_{x1}}{\partial x} - B'_{y1}v_{x1} - q\Omega B_{x1}, \tag{2.8}$$

where $d/dt = \partial/\partial t + \mathbf{v}_0 \cdot \nabla$ is a Lagrangian derivative, such outward v_{x1} directly induces the increment in B_{y1} through the second term in the right-hand side. This term comes from the linearized advection, which represents the fact that a fluid element brings the frozen-in magnetic field line from the original position of the stronger magnetic field. On the other hand, a linearized version of the equation of motion for the radial velocity is as

follows,

$$\rho_0 \frac{dv_{x1}}{dt} = -\frac{\partial p_1}{\partial x} - \frac{\partial}{\partial x}\left(B_{y0}B_{y1}\right) + B_{y0}\frac{\partial B_{x1}}{\partial y} + 2\rho_0 \Omega v_{y1}. \tag{2.9}$$

Note that the tidal force term is exactly canceled by the Coriolis force working on the zeroth-order velocity. The second and third terms in the right-hand side represent the magnetic pressure gradient and the magnetic tension force, respectively. The magnetic pressure can be further decomposed into two contribution from $-B'_{y0}B_{y1}$ and $-B_{y0}\partial_x B_{y1}$. The increase in B_{y1}, then, leads to further expansion force via the first component of the magnetic pressure, which implies a positive feedback. This feedback process will continue to work as long as the finite gradient in the background magnetic field is available.

As well as the growth rates, the range of unstable wavenumbers also tends to broaden as the plasma beta decreases, especially toward the long-wavelength side. The smallest scale, on the other hand, seems to always be limited roughly by $k_y d < 0.5$, which corresponds to the wavelength one order of magnitude larger than d. This bound could be understood qualitatively by competition between the magnetic pressure gradient force, which is a driver here, and the magnetic tension force working as restoring force. For the feedback mechanism described above to work, it is clear that the expansive nature of the magnetic pressure needs to dominate over the tension effect. These promoting and restoring effects can be rearranged into the form of the Lorentz force, $\mathbf{J}_1 \times \mathbf{B}_0$ and $\mathbf{J}_0 \times \mathbf{B}_1$. The schematic view of the situation is illustrated in Fig. 2.2. Then, the condition that the expansive term outpaces the restoring force is roughly estimated as

$$\left|\frac{\partial B_{y0}}{\partial x} B_{y1}\right| > \left|\frac{\partial B_{x1}}{\partial y} B_{y0}\right|.$$

Replacing the derivatives by typical scales like $1/d$ and k_y, we obtain the rough estimate, $1/d > k_y$, which is consistent with the unstable range in Fig. 2.1. The situation seems similar to the case of a magnetic bouyancy instability, where the magnetic buoyancy plays a role of a driver instead(e.g., Parker, 1955; Moffatt, 1978). Although the non-uniformity of a magnetic field is essential in both instabilities, the present mode is related to radial velocity perturbation, rather than the vertical velocity as in the magnetic buoyancy mode.

The destabilization mechanism described above seems not to be related to the differential rotation. For the comparison purpose, growth rates in a rigid-rotating plasma, which is described by $q = 0$, are shown in Fig. 2.3 with the same format as in Fig. 2.1. This panel

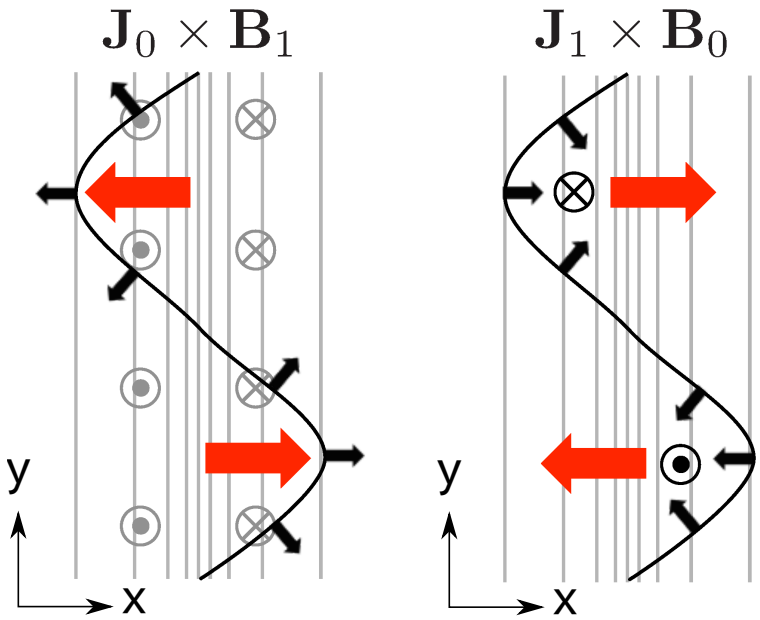

Figure 2.2: Schematic view of first-order Lorentz forces. In the left panel, the background current ($\mathbf{J}_0$; gray circles) makes expansive Lorentz force (black arrows) combined with the perturbed magnetic field ($\mathbf{B}_1$; black lines). The resultant force works to increase the perturbation, like shown by the red arrows. In the right panel, on the other hand, a cross product of the first-order current ($\mathbf{J}_1$; black circles), which is generated by the perturbed magnetic field, and the background magnetic field ($\mathbf{B}_0$; gray lines) makes the inward Lorentz force, which always works as the restoring force.

indicates the existence of unstable modes over a range similar to that in the differentially rotating case. The qualitative dependence on k_y and β also resembles that in Fig. 2.1, but the magnitude of the growth rate becomes smaller by a factor of 2 for $\beta = 1$, and much more for larger β. Therefore, it can be concluded that this instability arises originally from the gradient of the magnetic field itself, and can attain a large growth rate comparable to that of the standard MRI only when incorporated with the shearing motion.

2.2.3 Eigenfunctions

Let us discuss the structure of the eigenfunctions. Fig. 2.4 shows two-dimensional representation of the Fourier decomposed eigenfunction, $\mathbf{U}_1$, superposed on the background equilibrium state, $\mathbf{U}_0$, where $\mathbf{U}_1$ is normalized to satisfy $|\mathbf{U}_1| / |\mathbf{U}_0| = 1$. Based on the normalized case in panel (b), the states before and after twice the e-folding time are shown in panels (a) and (c), respectively. The plasma beta and the wavenumber are chosen to be $\beta = 100$ and $k_y d$=0.223, and the corresponding point on the k_y-β diagram is plotted in Fig. 2.1 by an outlined circle. In each panel, the color contour, the solid lines, and the

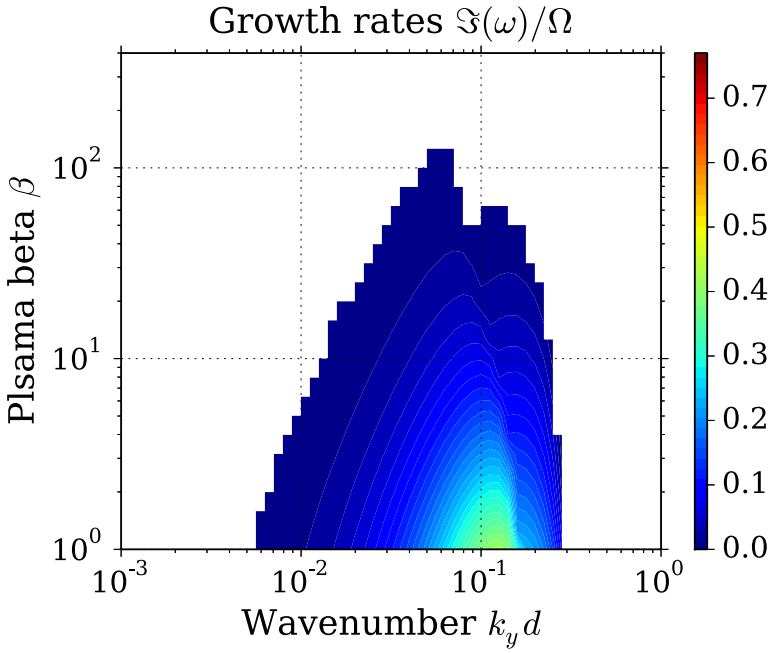

Figure 2.3: The color contour of growth rates in a rigid-rotating plasma, $q = 0$, with the same format as in Fig. 2.1.

vector field show the gas pressure distribution, the lines of magnetic force, and the bulk velocity, respectively.

Fig. 2.4 shows that bending of the field line broadens with time, and eventually spreads out beyond the initial width of the equilibrium field, $d = 0.05L_x$. This broadening of the field line is explained by the destabilization process described in the previous subsection, i.e., the outward magnetic pressure gradient force exceeding the inward magnetic tension force may further expand the magnetic field explosively. In addition to the expansion in the x-direction, the field lines are also stretched in the y-direction by the so-called Ω-effect due to the background shear motion, and thus the magnetic field lines become inclined downward to the right. In other words, B_x and B_y tend to have negative correlation. It can, therefore, be expected that the MGDIs have the potential to contribute to powerful angular momentum transport, creating the averaged Maxwell stress, $\langle -B_x B_y \rangle$, once they develop to nonlinear turbulence.

Other features of importance include vortex structure around the nodes of the magnetic field lines in panel (c). In particular, the clockwise vortices at every other node, which align with the differential rotation, are selectively enhanced. Since the Coriolis force works rightward to the direction of motion, the inside of the clockwise vortex is compressed, and the other is expanded. The selective enhancement, on the other hand, makes the magnetic

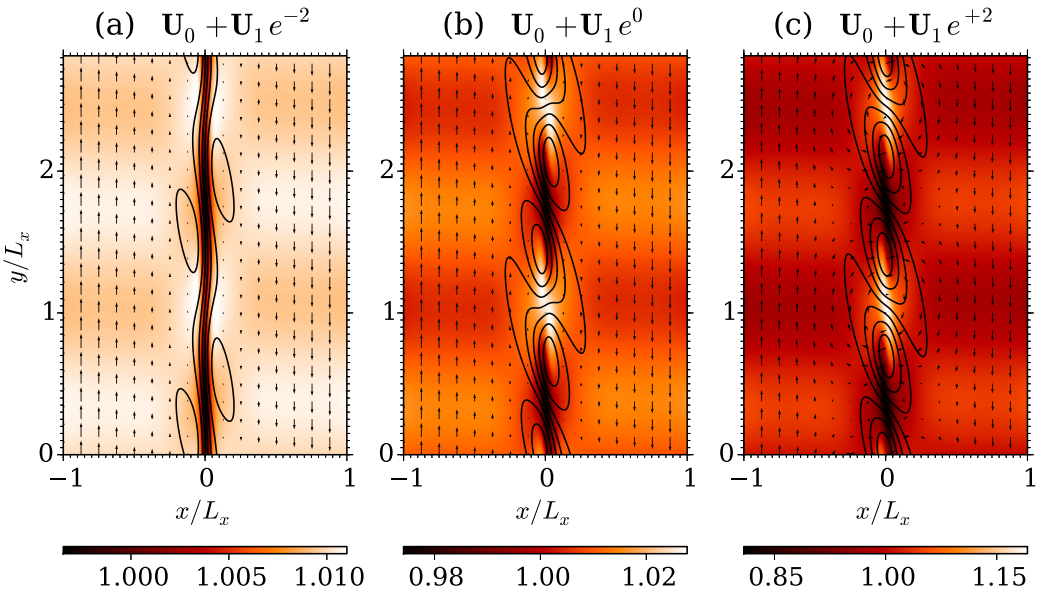

Figure 2.4: Two-dimensional views of an unstable eigenfunction with the wavenumber $k_y d = 0.223$, superposed on the background plasma with $\beta = 100$. The corresponding growth rate is 0.039Ω. The color contour, the solid lines, and the vector map indicate the gas pressure, the magnetic field lines, and the velocity, respectively. The first-order eigenfunction $\mathbf{U}_1$ is normalized by $|\mathbf{U}_1| = 1$. From left to right, the amplitude of the eigenfunction increases $2e$-fold.

field lines loosened around the clockwise vortex as if a tightly stretched rope is reeled up. This leads to the negative correlation between the gas pressure and the magnetic pressure, which implies that the present unstable mode is essentially related to slow-magnetosonic waves.

Looking at Fig. 2.4, one may associate the MGDIs with current-driven instabilities (CDIs), which are thought to contribute fast dissipation of magnetic energy in various astrophysical contexts (e.g., Mignone et al., 2010; O'Neill et al., 2012; Mizuno et al., 2014). Although the characteristic that both unstable modes are driven by magnetic non-uniformity is common, we consider the MGDI as a fundamentally different mode from the CDI. To clarify the difference, for example, notice that the wavevector of the CDI is essentially parallel to the background electric current, which drives the instability. In the case of the MGDI, on the other hand, the background current has only an out-of-plane component, which is obviously perpendicular to wavevector of the perturbation.

Figs. 2.5 and 2.6 show the eigenfunctions for the cases with β=10 and 1, respectively, in the same format as in Fig. 2.4. The wavenumber is again assumed to be $k_y d$=0.223.

Since the magnetic tension force, working as a restoring force, becomes stronger with an increase in the magnetic field strength, it becomes more and more difficult to bend the magnetic field lines significantly, and the unstable mode seems to localize around the initial channel. It should be noted that the localization of the eigenfunction and its growth rate is a different matter. The growth rate actually becomes greater with the background magnetic field strength increased, as shown in Fig. 2.1, due to a large gradient of the field.

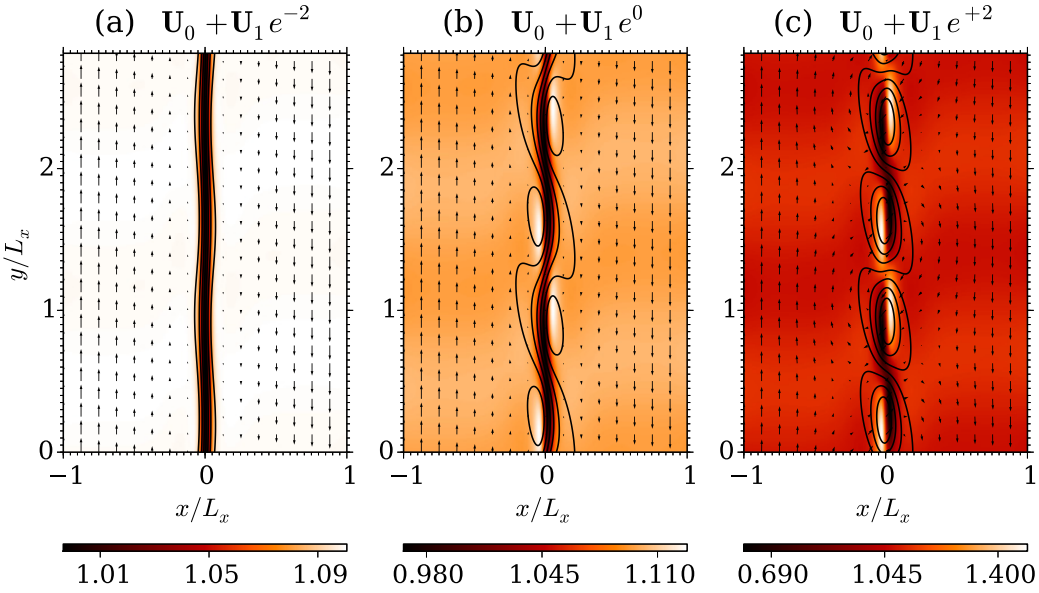

Figure 2.5: Unstable eigenfunction with $\beta = 10$ and $k_y d = 0.223$. The format is same as in Fig. 2.4. The growth rate is 0.430Ω.

While this localization implies a small B_{x1} compared with the initial B_y, how it affects the average value of the Maxwell stress is not trivial. The estimate of the efficiency of the angular momentum transport is tightly connected with the nonlinear behavior and the problem of the saturation mechanism. In the next section, we will discuss the significant contribution of the present instability to the stress, using nonlinear simulations.

2.3 Nonlinear simulations

This section provides the results of fully-nonlinear MHD simulations designed to validate the presence of MGDIs suggested in the previous section and to investigate the nonlinear time evolution. Specifically, we focus on the efficiency of angular momentum transport.

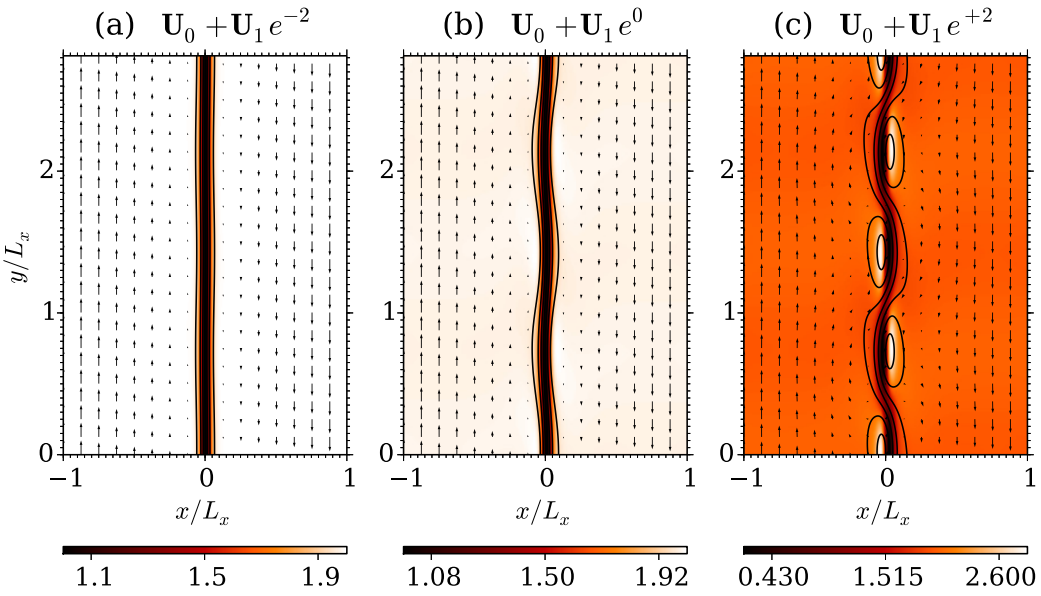

Figure 2.6: Unstable eigenfunction with $\beta = 1$ and $k_y d = 0.223$. The format is same as in Fig. 2.4. The growth rate is 0.675Ω.

2.3.1 Basic equations and simulation codes

We solve the same equations as used in the previous section, i.e., from equation (2.1) to (2.4), but rewritten in the semi-conservative form:

$$\frac{\partial \rho}{\partial t} + \nabla \cdot (\rho \mathbf{v}) = 0, \tag{2.10}$$

$$\frac{\partial (\rho \mathbf{v})}{\partial t} + \nabla \cdot \left[\rho \mathbf{v}\mathbf{v} + \left(p + \frac{B^2}{2} \right) \mathbf{I} - \mathbf{B}\mathbf{B} \right] = -2\rho \boldsymbol{\Omega} \times \mathbf{v} - 2\rho \Omega x v'_{0y} \hat{\mathbf{e}}_x, \tag{2.11}$$

$$\frac{\partial \mathbf{B}}{\partial t} = \nabla \times (\mathbf{v} \times \mathbf{B}), \tag{2.12}$$

$$\frac{\partial e}{\partial t} + \nabla \cdot \left[\left(e + p + \frac{B^2}{2} \right) \mathbf{v} - (\mathbf{v} \cdot \mathbf{B}) \mathbf{B} \right] = -2\rho \Omega x v'_{0y} v_x, \tag{2.13}$$

where $e = \rho v^2/2 + p/(\gamma - 1) + B^2/2$ is the total energy density, and the other notation is same as in the linear analysis. The specific heat ratio is again set to be $\gamma = 5/3$. All quantities are spatially discretized by using the finite difference approach in a computational domain, $(x, y) \in [-L_x, L_x] \times [0, 2\pi L_x]$, which is resolved with 200×600 grid points.

We calculate the flux with the help of the HLL approximate Riemann solver (Harten et al., 1983) at the face center, where the primitive variables, i.e., ρ, $\mathbf{v}$, $\mathbf{B}$, and p, are evaluated as point values by combining a 5th-order weighted essentially non-oscillatory (WENO)

interpolation (Liu et al., 1994; Jiang & Shu, 1996) and the monotonicity preserving limiter (Suresh & Huynh, 1997). The point-value flux is then converted to the appropriate numerical flux with a 6th-order formula (Shu & Osher, 1988). The cell-centered conservative variables are finally updated using the 3rd-order TVD Runge-Kutta method (Shu & Osher, 1988). To avoid a spurious magnetic monopole, the HLL-upwind constrained transport (UCT; Londrillo & del Zanna (2004)) treatment is employed for updating the face-centered magnetic field, in which the edge-centered electric field is evaluated using WENO interpolation and the HLL average. Note that the results to be shown in this section will not largely change, even if the HLLD Riemann solver, which is more accurate than the HLL Riemann solver especially in high-β plasmas (Mignone et al., 2007, 2009), is employed instead. The quantitative behavior of statistics, however, slightly differs due to the higher resolution of each wave mode. In particular, less diffusivity is preferable to larger stress related to turbulent motion in small scales.

2.3.2 A single localized magnetic field

Our initial condition is set to be a superposition of exactly the same equilibrium state considered in the linear analysis and a random perturbation of the in-plane velocity, the amplitude of which is fixed to 1% of the sound speed measured in an unmagnetized region. Without the random perturbation, the system would remain in the initial equilibrium state. To calculate the long time evolution of the system, we implement the standard shearing periodic boundary condition. Even if one adopts a conducting wall boundary, the results do not change in the early stage, before the distorted magnetic fields approach the radial boundary.

From left to right in Fig. 2.7, snapshots of the simulations with β=100, 10, and 1 taken at time $\Omega t/2\pi = 20$ are shown. The format of each panel is same as in Figs. 2.4 to 2.6 except for the range of the y-coordinates. All of these cases show the negative correlation between B_x and B_y reflected as the downward-sloping magnetic field lines, which contributes to angular momentum transport. While the linear theory discussed in the previous section predicts broadband growth for a stronger initial field, the typical scale of the bending of the field line is clearly larger for smaller β, which suggests that the magnetic tension force works more efficiently in nonlinear evolution and then the growth of short waves is suppressed. In larger β cases, on the other hand, the bent mean structure and other small-scale magnetic structures appear. Such structures first grow along the both

sides of the initial field, where the large gradient $|\partial B_y/\partial x|$ exists, and then they are torn off from the mean field by magnetic reconnection. (Note that magnetic reconnection occurs via numerical resistivity, but the nonlinear evolution does not change by assuming a finite resistivity.) In any case, the nonlinear growth up to torsion of the localized magnetic field is ascertained. Note that the stage where the linear theory is applicable finishes instantly, since the growing perturbed field quickly breaks the background structure of the initial magnetic field.

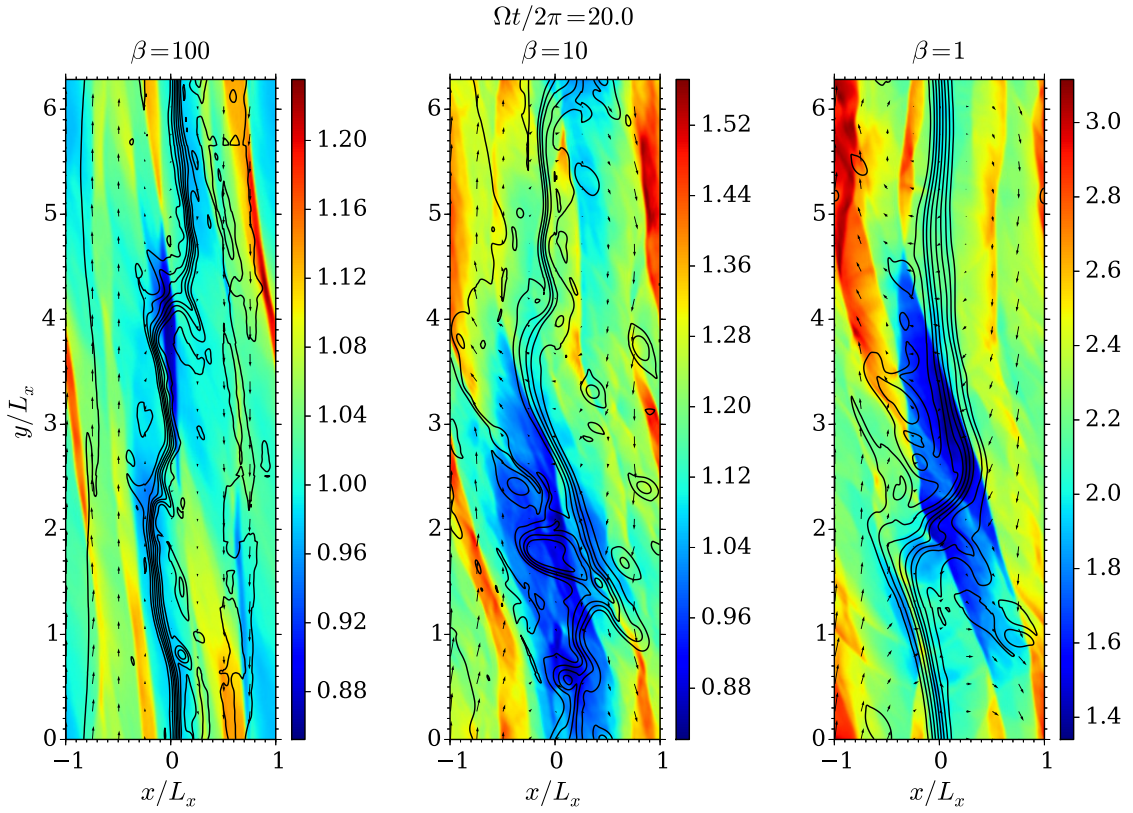

Figure 2.7: Snapshots of the MHD simulations at twenty times the orbital period. The color contours, solid lines, and arrows represent the gas pressure, the lines of magnetic force, and the in-plane velocity, respectively.

Fig. 2.8 summarizes the box-averaged stress as a function of time. The xy-components of the Reynolds stress and the Maxwell stress normalized by the initial gas pressure, or the so-called α-parameters, are plotted in each panel. The instantaneous Reynolds stress generally fluctuates significantly with time, but the temporal average over the interval $15 \leq \Omega t/2\pi \leq 20$ takes a positive value of the order of 10^{-3}. The Maxwell stress, on the other hand, remains positive during the nonlinear evolution, which is still smaller by one or two orders of magnitude compared with the local three-dimensional simulations of

MRIs (Hawley et al., 1995, 1996, etc.). Note that the case of $\beta = 100$ shows a remarkably small value in spite of a more broken structure, due to the weakness of the initial field.

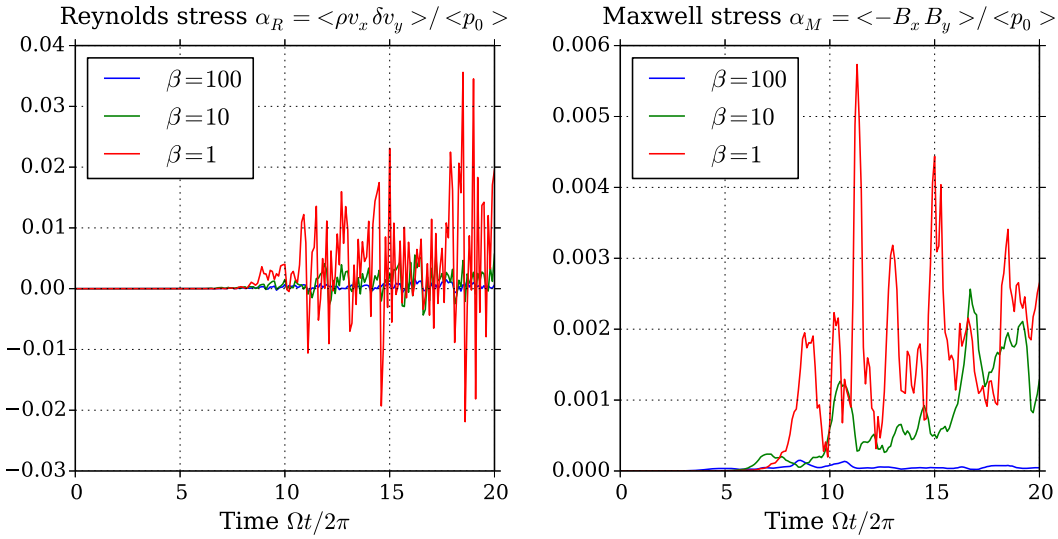

Figure 2.8: Time histories of the box-averaged stress. The left and right panels show the xy-components of the Reynolds stress and the Maxwell stress normalized by the averaged initial gas pressure, that is, the α parameters.

To put it another way, however, once the magnetic field lines are stretched to the point of crossing the radial boundary, much stronger azimuthal fields could be expected. The point is a stretching term in the governing equation for the azimuthal magnetic energy,

$$\frac{d}{dt}\left(\frac{B_y^2}{2}\right) = B_x B_y \frac{\partial v_y}{\partial x} - B_y^2 \frac{\partial v_y}{\partial y}, \tag{2.14}$$

where the first and the second terms in the right-hand side represent the energy change by stretching and compressive motions, respectively. Especially, the energy increase through the background velocity shear, $B_x B_y v'_{y0}$, is called the Ω-dynamo. In a radially periodic system like the shearing box, if a fluid element can move largely across the radial boundaries, the total velocity shear which the element feels becomes much larger than the shear just within one simulation domain, $q\Omega L_x$. The larger radial fluctuation, therefore, leads to the stronger azimuthal magnetic energy. The next subsection is devoted to suggesting such a possible path leading to a more amplified magnetic field and a resultant large Maxwell stress.

2.3.3 Multiple localized magnetic fields

As a phenomenon expected to occur in accretion disks, let us consider the situation where a toroidal magnetic field has multiple structures rather than a single localized field. The motivation of this idealized setup comes from, for example, the existence of a parasitic instability occurring on a current sheet, which induces periodic variation of plasma parameters along an equatorial plane (Goodman & Xu, 1994; Pessah & Goodman, 2009; Rembiasz et al., 2016). The physical mechanism driving the instability in the linear stage does not change even in this case, but a more turbulent state could be expected in the nonlinear stage as a result of coupling between neighboring fields. This section shows a possible path through which the MGDIs may contribute to stronger turbulence generation and anomalous angular momentum transport.

The simulation setup is the same as described in the previous subsection except for the initial profile of the magnetic field. Here we assume the functional form of the toroidal magnetic field as follows:

$$B_{y0}(x) = B_c \cos^4\left(\frac{3\pi x}{L_x}\right), \tag{2.15}$$

which reproduces both the locality within $0.05L_x$ and the periodicity of the localized structure. The pressure and density profiles are also modified to keep dynamical and thermal equilibrium. The plasma beta is defined using the peak value of the magnetic field, B_c, and the gas pressure at the same site.

Figs. 2.9, 2.10, and 2.11 show snapshots at characteristic stages in the cases with β=100, 10, and 1, respectively. The three panels in each figure are taken at times $\Omega t/2\pi$ = 5, 10, and 20 from left to right, and the format of each panel is the same as in Fig. 2.7. In the leftmost panel in Fig. 2.9, we can see that the discrete magnetic field lines are distorted individually in the early stage by the nonlinear growth of MGDIs, just as demonstrated in the simulations with a single localized field. The bending of the field lines grows as time goes on, and before 10 orbits they drastically overlap and merge with the neighboring magnetic fields. The mixing of the magnetic field completes by 20 orbits, and the simulation domain is filled with a lot of magnetic islands as a result of the repetitive reconnection process. Recall that, in a single channel case, the reconnected field simply gets torn off the background field and shows no further turbulent development. At this stage, the energy contained in the magnetic field increases to about 10% of the kinetic energy of the background differential rotation. Even if the difference of the initial magnetic energy is taken

into account, this ratio is rather large compared with the case of a single localized field, where the magnetic energy at the saturated stage is smaller by three orders of magnitude.

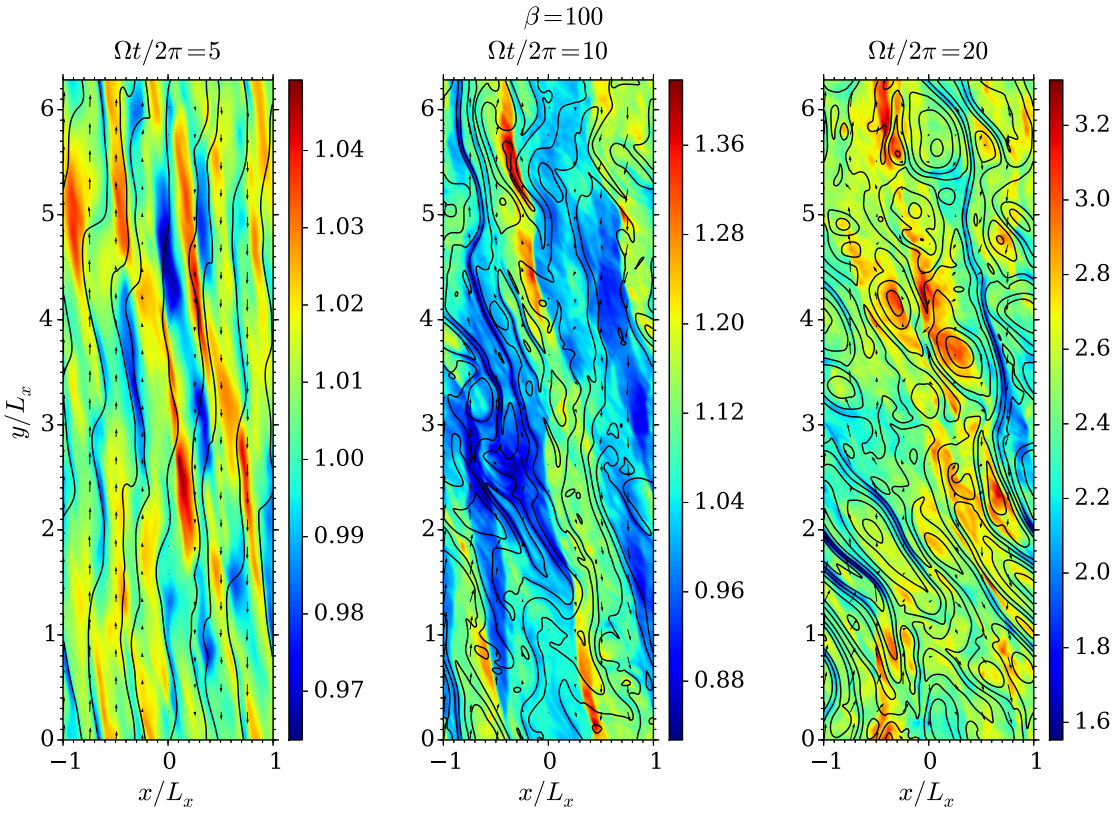

Figure 2.9: Snapshots of the simulation started from a wavy toroidal field with $\beta = 100$, taken at 50, 100, and 200 orbits. The format of each panel is the same as in Fig. 2.7.

The detailed time history of the box-averaged energy is summarized in Fig. 2.12(a), which shows that the dynamo process works efficiently on both B_x and B_y at an early stage before 20 orbits, and roughly speaking, an equi-partition is eventually attained between the kinetic energy in the x-direction and the magnetic energy in the x- and y-directions. The production of the strong azimuthal field is understood as a natural consequence from equation (2.14), which tells the effect of Ω-dynamo. A similar relation holds with regard to the radial field energy as

$$\frac{d}{dt}\left(\frac{B_x^2}{2}\right) = B_x B_y \frac{\partial v_x}{\partial y} - B_x^2 \frac{\partial v_y}{\partial y}, \tag{2.16}$$

which shows that shear motion in the radial velocity newly generates the radial magnetic field. It is clear that in the MGDI this radial velocity is driven by the magnetic pressure

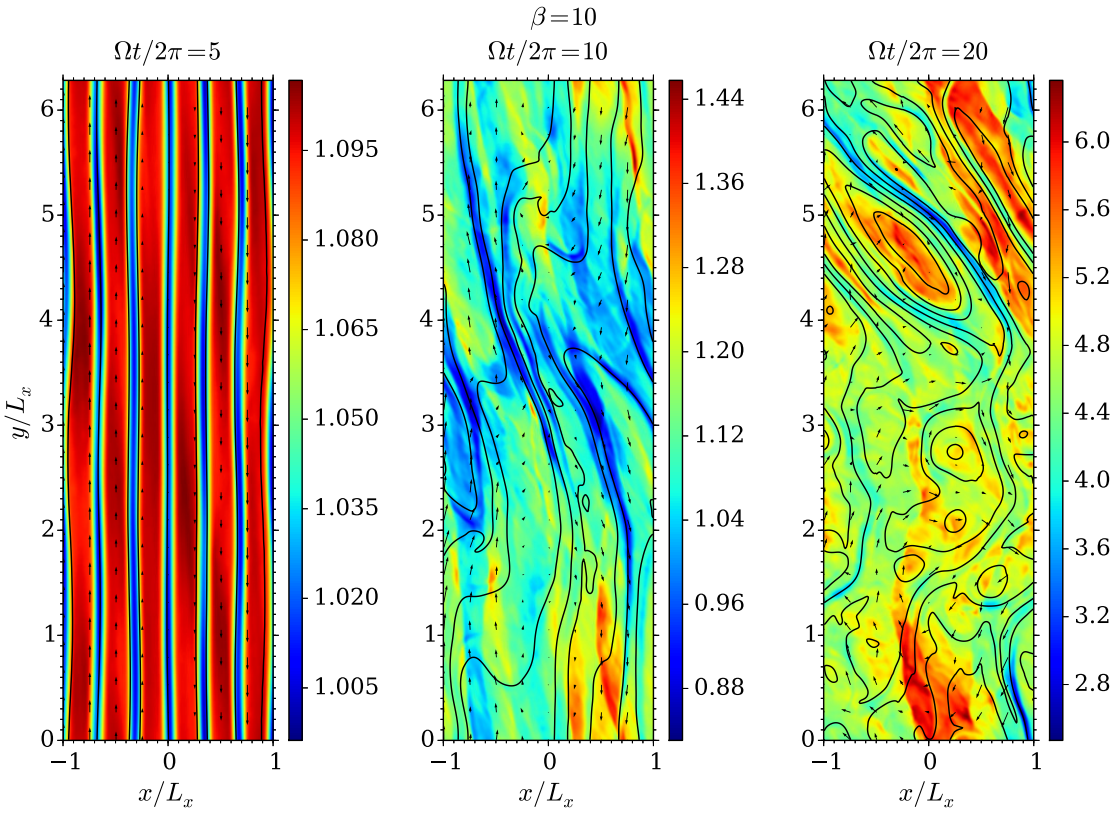

Figure 2.10: Snapshots of the case of $\beta = 10$, with the same format as in Fig. 2.9.

gradient force, while the gravity-related terms play the same role in the case of MRI. In this sense, the dynamo process working here looks quite similar to that in the MRI not only in the azimuthal field, but also in the radial field. At the saturated stage, the gas pressure gradually increases through magnetic reconnection, creating many magnetic islands.

Even when the initial magnetic energy is ten times as large, that is, $\beta = 10$, the same instability grows as shown in Fig. 2.10. Compared with the case of $\beta = 100$, it can be seen that the typical scale of the growing mode becomes larger, as does the size of the magnetic islands in the final stage. The gas pressure at 20 orbits increases about twofold, which implies that the total amount of energy input into the system across the boundaries is enhanced and continuously converted to the internal energy of the plasma through magnetic reconnection. In other words, the total stress integrated along the radial boundary gets larger, since the time variation of the total energy, e, can be described as follows:

$$\frac{\partial}{\partial t}\int e\,dV = 2\,|v_{0y}(L_x)|\int_{x=L_x} W_{xy}dy - \int 2\rho\Omega x v'_{0y}v_x dV, \tag{2.17}$$

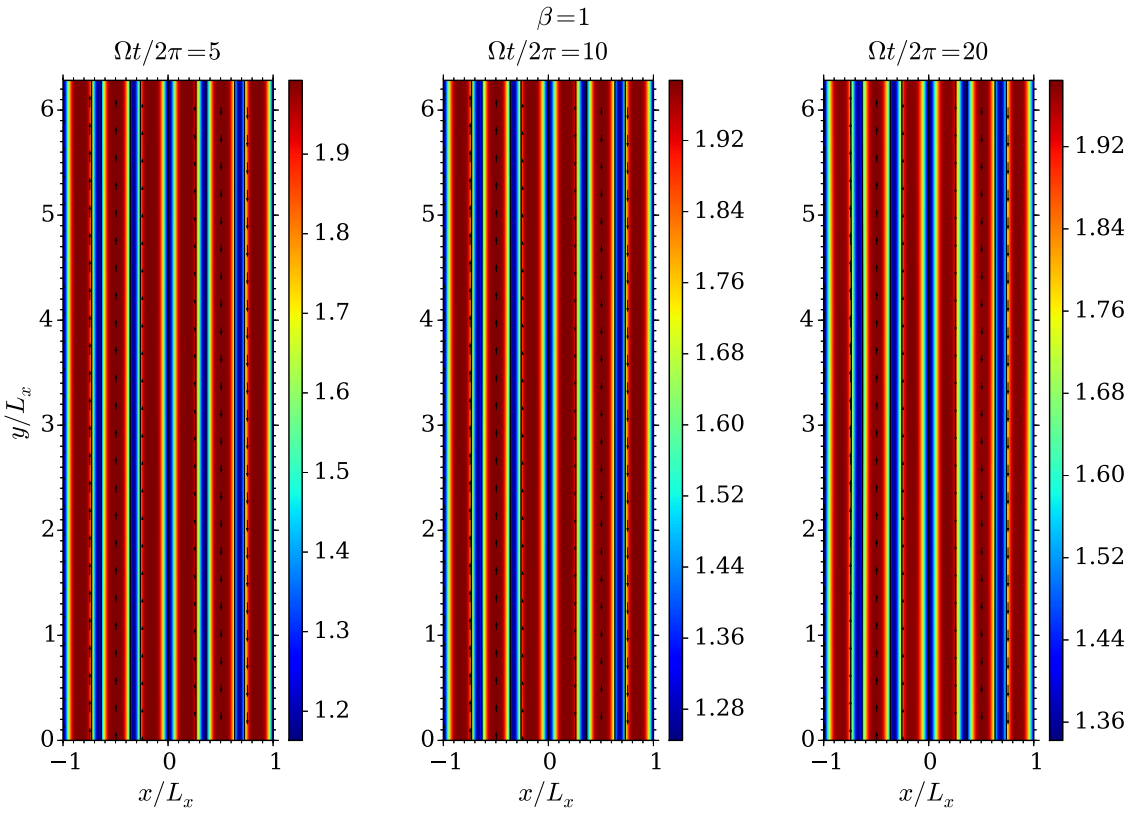

Figure 2.11: Snapshots of the case of $\beta = 1$, with the same format as in Fig. 2.9.

where $W_{xy} = \rho v_x \delta v_y - B_x B_y$ is the total stress. The second term on the right-hand side of equation (2.17), which represents the change in the total gravitational potential in the simulation domain, becomes nearly zero on average. The detailed time history of each energy component is plotted in Fig. 2.12(b). As in the case of $\beta = 100$ shown in panel (a), the growing mode is saturated before 20 orbits, after which the kinetic energy related to v_x and the magnetic energy reach a level comparable to the background differential rotation, but slightly larger than those in the case with a weaker initial field.

However, this situation changes significantly for the strong magnetic field with $\beta = 1$ shown in Fig. 2.11. The initial equilibrium state remains and no growing mode can be observed. It is interesting to note that the nonlinear evolution is accomplished in the single field case discussed in the previous subsection. The energy history in Fig. 2.12(c) also shows a quite calm variation. The suppression of the growing mode is indeed the result of the nonlinear magnetic tension force, since we confirmed the presence of unstable modes in linear analyses under the initial magnetic profile described here.

We summarize the time histories of the Reynolds and Maxwell stresses in Figs. 2.13(a) and 2.13(b), respectively. The result of $\beta = 1$, denoted by the red line, shows no stress

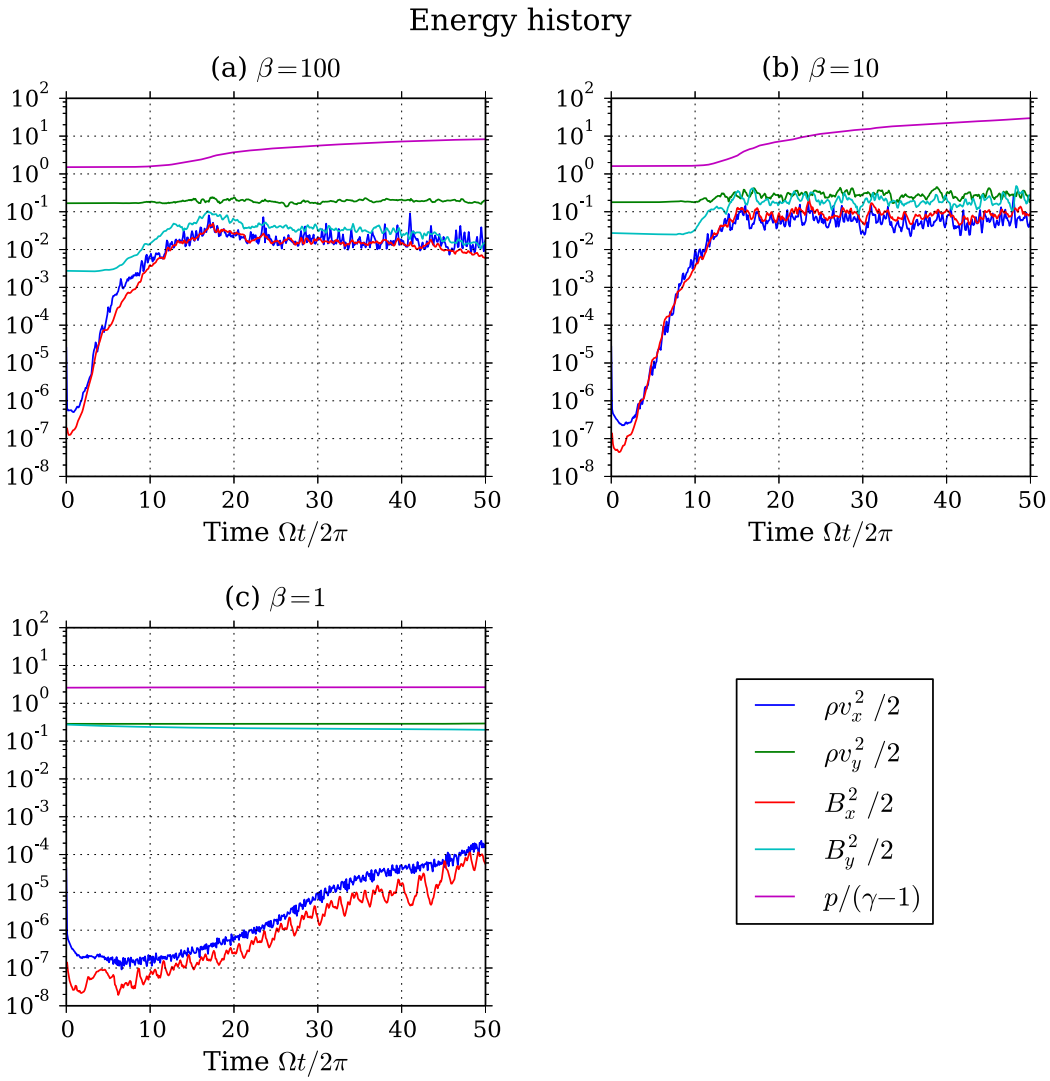

Figure 2.12: Temporal development of the box-averaged energy divided into the contribution from the x and y directions, all of which are normalized by the gas pressure measured in a magnetized region. Each panel shows the results for (a) $\beta = 100$, (b) $\beta = 10$, and (c) $\beta = 1$, respectively.

for either the Reynolds or Maxwell components, because the initial equilibrium state is almost preserved. In the cases with $\beta = 10$ and 100, denoted by the green and blue lines, the Reynolds and Maxwell stresses averaged after 20 orbits are -0.00109 and 0.0235 for $\beta = 100$, and -0.0164 and 0.126 for $\beta = 10$, respectively. The Maxwell stress, therefore, is larger by about two orders of magnitude than the results in the single field case, which means a qualitative change in the nonlinear behavior, rather than the simple quantitative superposition due to an increase in the initial total magnetic flux. In addition, the result for a stronger shear motion with $q = 1.5$, which corresponds to the Kepler rotation, is also

plotted as a cyan line. The basic mechanism driving the instability is same as in the case with $q = 1.0$, but thanks to the more powerful Ω-dynamo effect, the MGDI can grow more quickly nonlinearly and a larger Maxwell stress can be attained at the saturated stage.

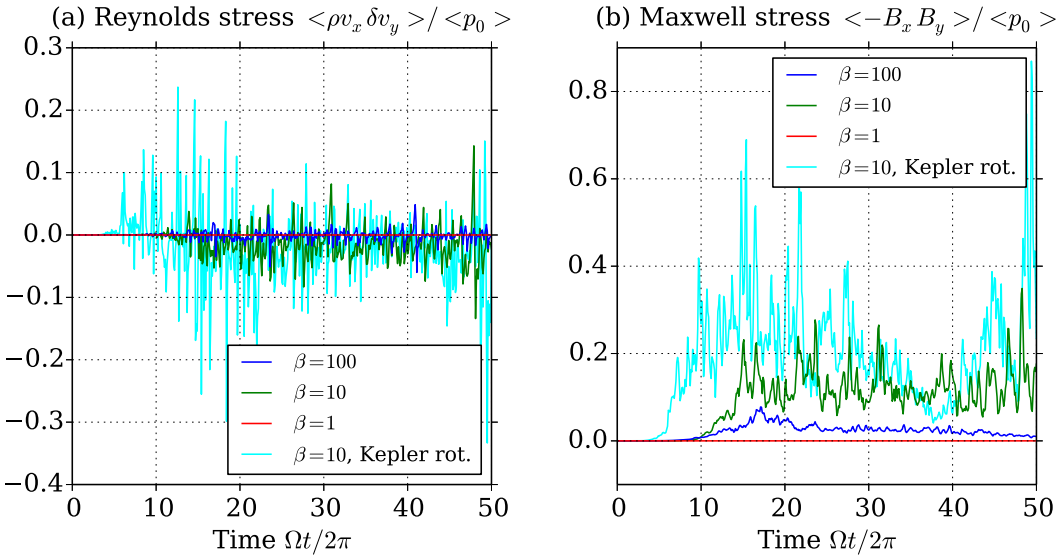

Figure 2.13: The xy-components of the (a) Reynolds and (b) Maxwell stress tensors as functions of time.

The β-dependence of the Maxwell stress averaged during the saturated stage between $30 \leq \Omega t/2\pi \leq 50$ is summarized in Fig. 2.14. It can be clearly seen that the results are well fitted by a power law of $\beta^{-1/2}$ as long as $\beta > 2$, which indicates the proportionality to the initial magnetic flux rather than magnetic energy density, while the cases starting with $\beta < 2$ result in almost no stress.

The suppression of instabilities for a small β is highly relevant to the large characteristic spatial scale under the strong magnetic tension force, which works less efficiently for longer waves. Although this mode has a broad unstable range in wavelength with respect to the linear theory around a single channel, the nonlinear growth is actually quenched in the multiple channel case. Once the simulation box is extended double in the azimuthal direction, however, the drastic growth in the Maxwell stress via channel merging process is activated even for $\beta = 1$. This certainly happens because the extended box allows the growth of the fluctuations with the scale larger than the original domain size. Fig. 2.15 shows the time histories of the Reynolds and Maxwell stress for β=1, 10, and 100, respectively, normalized by the volume averages of the instantaneous thermal pressure, $\langle p\,(t)\rangle$. From the right panel, we can clearly observe the enhancement of the Maxwell stress by the nonlinear growth after 50 orbits for $\beta = 1$. Except for the shifted time when this drastic

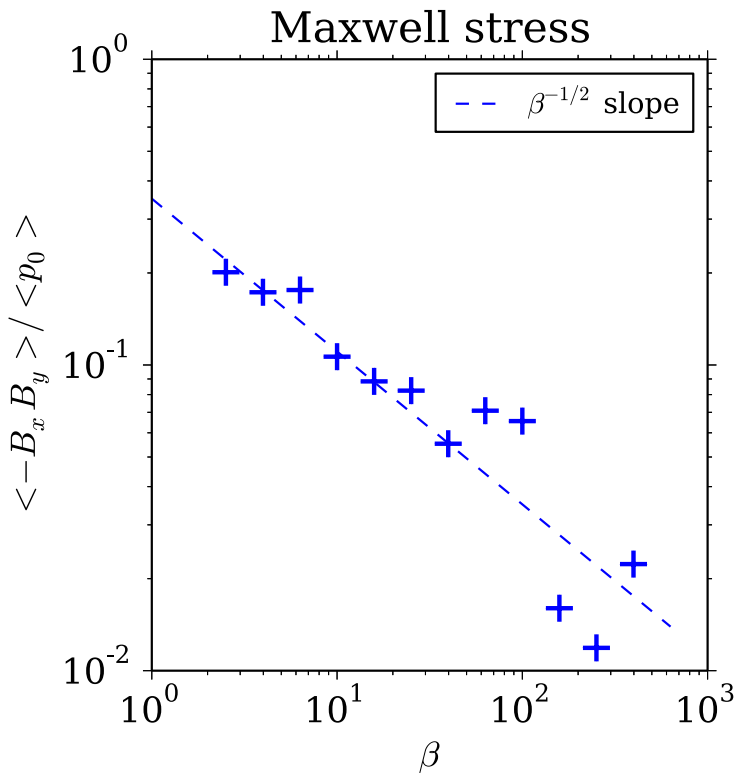

Figure 2.14: The Maxwell stress averaged during the saturated stage as a function of the initial β.

merging is switched on, the statistical behavior is quite similar in all cases, which implies that the MGDI works as the common underlying mechanism to drive the turbulence.

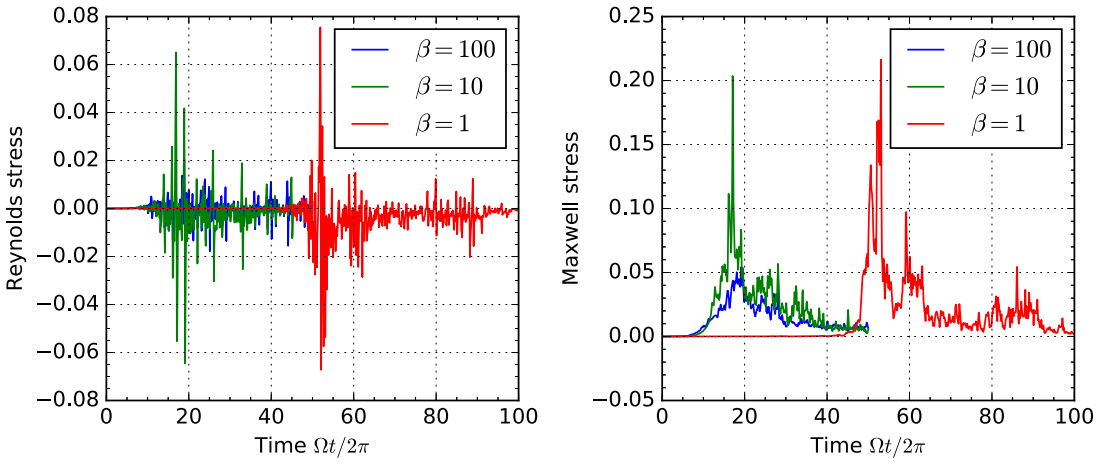

Figure 2.15: Time histories of the Reynolds and Maxwell stress normalized box averages of the instantaneous gas pressure in the elongated simulation box, $(x, y) \in (2L_x, 4\pi L_x)$, for different initial β.

2.4 Discussion and summary

In the present chapter, we have proposed a new plasma instability, MGDI, which can generate a highly turbulent state in an accretion disk and contribute to the enhanced transport of angular momentum. Driven by the spatial non-uniformity of a toroidal magnetic field, an unstable mode completely confined within the equatorial plane can be realized, in contrast to the previous studies on the toroidal MRI, in which a vertical wavenumber always dominates over a finite azimuthal component.

The growth rates and eigenfunctions of this instability are calculated by linear eigenvalue analysis, and the corresponding nonlinear evolution is then demonstrated using two-dimensional MHD simulations. While the simulations beginning with a single localized toroidal field reveal the nonlinear growth of the MGDIs, it is shown that the angular momentum transport does not work so efficiently in the saturated stage. If the instabilities occur in the neighboring field lines under the multiple localized magnetic fields rather than in an isolated situation, however, they drastically overlap with each other and a well-developed turbulent state can be realized. In such a case dynamo action by differential rotation begins to work efficiently on magnetic field lines crossing the radial boundaries, which contributes to a large Maxwell stress. Furthermore, we have shown that a toroidal field with a larger magnetic flux is favorable for the Maxwell stress to reach a large value, but this drastic transition does not occur for a magnetic field that is too strong with $\beta < 2$, as long as we employ the box size, $2L_x \times 2\pi L_x$. Once the simulation domain is elongated, the transition is reactivated, but it takes much longer time to switch on the drastic merging. It is worth noting that the situation with $1 \leq \beta \leq 10$, which is favorable to the growth of the MGDI, often appears during a nonlinear phase in a local simulation of the MRI for a relatively small initial beta, $\beta \sim \mathcal{O}\left(10^2\right)$. In the cases with larger initial β values, like $\beta \sim \mathcal{O}\left(10^{3-6}\right)$, the final states still seem to be in the unstable regime (e.g., Hawley et al., 1995; Sharma et al., 2006; Minoshima et al., 2015).

Although the profile of the toroidal magnetic field discussed here is one of the most idealized situations, the physical essence to drive the instability does not change even under a different structure, as long as an enough radial gradient of the magnetic field is available. There is, therefore, possibility that the present unstable mode will arise around various kinds of fluctuation in the toroidal field, like via parasitic modes including the Kelvin-Helmholtz instability and the tearing instability.

It should be emphasized again that the efficiency of the angular momentum transport obtained here is comparable to that obtained in evaluation in three-dimensional simulations of MRIs assuming an initial toroidal field, in spite of the low dimensionality, and therefore, the MGDIs are capable of driving strong turbulence alone. One might expect not just the sole contribution, but also coupling with magnetic reconnection occurring parallel to the equatorial plane during the nonlinear phase of MRIs, and with the toroidal MRIs as considered in previous studies if vertical variation is also taken into account. It is still not obvious that how large contribution the instabilities have in a fully three-dimensional shearing box. Nevertheless, since they provide new paths toward turbulence without any finite k_z in contrast to the conventional toroidal MRIs, the complementary growth between azimuthally and vertically propagating waves, rather than competitive growth, should be expected. The present instability could possess the ability to play a wide variety of crucial roles in the mechanism of turbulence generation in differentially rotating systems.

Chapter 3

New Fluid Model for Collisionless Magnetohydrodynamic Simulations with Anisotropic Pressure

3.1 Introduction

Space and astrophysical phenomena often occur in collisionless plasmas, where the gas is so hot and dilute that the mean free path of charged particles becomes longer than the system's scale size. To investigate such complicated collisionless systems, numerical simulations can be powerful tools. In fact, particle-in-cell (PIC) and Vlasov simulations are typical numerical methods to solve the Vlasov-Maxwell system, which represents a set of fundamental equations describing the time evolution of the velocity distribution function and the electromagnetic fields. Although these models can capture all important kinetic physics self-consistently, because of limited computational resources it is still hard to apply these methods to phenomena occurring on scales that significantly exceed the kinetic scales, such as those associated with Larmor radii and/or inertial lengths (but which are still smaller than the relevant mean free paths). The Earth's magnetosphere (e.g., Heinemann, 1999; Dumin, 2002; Karimabadi et al., 2014; Burch et al., 2015) and the solar wind (e.g., Hollweg, 1976; Zouganelis et al., 2004; Chandran et al., 2011) are typical examples of such large-scale collisionless plasmas in the solar system. Using an

astrophysical example, radiatively inefficient accretion flow models applied to accretion disks are also thought to represent collisionless plasmas (e.g., Ichimaru, 1977; Narayan & Yi, 1994; Quataert, 2003).

One classical way of dealing with both dynamical and kinetic scales is the so-called kinetic magnetohydrodynamics (MHD) approach, which can take into account some kinetic effects. This philosophy has given rise to the well-known double adiabatic approximation, also known as the Chew-Goldberger-Low (CGL) model (Chew et al., 1956), which pays special attention to the effects of anisotropy in a distribution function. Given that the orbit of a charged particle in a magnetized plasma essentially consists of a combination of its gyromotion around a magnetic field line and its parallel motion along the field line, the distributions of the kinetic energies contained in these independent motions may differ from each other. This situation requires us to extend the standard MHD model with a scalar pressure so as to handle the anisotropic pressure tensor. The double adiabatic approximation is a natural extension of the one-temperature MHD approach, where only the parallel and perpendicular components of the pressure tensor are solved. This is one of the simplest equations of state as a closure model of the moment hierarchy, assuming that the pressure is completely gyrotropic and the third- and higher-order moments are neglected. The properties of this formulation have been studied for decades and it has achieved a certain degree of success (e.g., Holzer et al., 1971; Hau & Sonnerup, 1993; Hau & Wang, 2007; Kowal et al., 2011).

There have been several approaches to construct models beyond the double adiabatic approximation. One noteworthy effort retains the contribution of the higher-order moments by employing a sophisticated heat-flux model, such as Landau closure (e.g., Hammett & Perkins, 1990; Snyder et al., 1997). A different approach was taken by Hada et al. (1999). It relaxes the assumption of the presence of a gyrotropic pressure tensor and introduces a new timescale to describe gyrotropization. This allows finite non-gyrotropy to remain. Wang et al. (2015) attempted to combine these two approaches together. In addition, asymptotic-preserving (AP) schemes (Jin, 1999) may also shed new light on the treatment of anisotropic pressure in some extreme cases.

The gyrotropic formulation in the CGL approximation, however, involves numerical and theoretical difficulties in handling magnetic null points. This comes from the fact that the direction of the magnetic field must be defined for the decomposition of a pressure tensor into its parallel and perpendicular components. From a numerical point of view,

determination of the unit vector parallel to the magnetic field, $\hat{\mathbf{b}} = \mathbf{B}/|B|$, will cause division by zero in a magnetic null point, which severely hampers numerical simulations. If one employs the form of a conservation law, the conservative variable pertaining to the first adiabatic invariant includes the magnetic field in the denominator as well. This drawback may become critical when, for example, considering a current sheet without a guide field, which contains a magnetically neutral line in its own right. The role of pressure anisotropy as pertaining to collisionless magnetic reconnection cannot be studied, therefore, in the framework of the CGL equations.

This breakdown apparently comes from the strong assumption that a pressure tensor can be well described by the gyrotropic form. In other words, the gyro-motion is well-defined on a much shorter timescale than the relevant dynamical timescale. If the magnetic field is so weak that the gyro period becomes comparable to the dynamical timescale, the parallel and perpendicular motions cannot be distinguished from each other and the gyrotropic approximation is no longer valid. As long as we are stuck with the gyrotropic limit, therefore, the problem of division by zero at magnetic null points will not be eliminated completely, regardless of the form of the equations of states employed.

With this in mind, we relax the assumption of gyrotropic pressure and extend the equations of state so as to allow finite deviations from the gyrotropic formulation. This chapter focuses on such a natural extension of the MHD approach following the context of a governing equation that describes a more general form of the pressure tensor. Desirable characteristics of the newly defined theoretical and numerical framework are (1) avoidance of numerical difficulties owing to division by zero in magnetically neutral regions; (2) removal of any temporal and spatial scales related to kinetic physics; (3) convergence to the gyrotropic and isotropic formulations, respectively, under appropriate limits; and (4) a simple modification of an existing MHD code. In this chapter, we successfully derive a new framework that satisfies these requirements by evolving a 2nd-rank pressure tensor directly, and we develop a corresponding, extended MHD code.

The present chapter is organized as follows. First, we derive our analytical formulation in section 3.2. Next, section 3.3 describes the actual implementation of our simulation code based on the finite-difference approach. The numerical behavior is tested in section 3.4. Finally, section 3.5 contains a summary as well as our concluding remarks.

3.2 Formulation

3.2.1 Generalized energy conservation law

In this subsection, we will briefly derive our fluid model, starting from the Vlasov equation,

$$\frac{\partial f_s}{\partial t} + \mathbf{v}_s \cdot \nabla f_s + \frac{q_s}{m_s}\left(\mathbf{E} + \frac{\mathbf{v_s}}{c} \times \mathbf{B}\right) \cdot \nabla_{\mathbf{v}} f_s = 0, \tag{3.1}$$

where the subscript s indicates the species of charged particles — in this thesis, ions, i, and electrons, e. The other notations are standard. Taking the second moment of the particle velocity $\mathbf{v}_s$ in Eq. (3.1), we obtain a kinetic stress tensor equation:

$$\begin{aligned}\frac{\partial}{\partial t}\left(m_s n_s \mathbf{V}_s \mathbf{V}_s + \mathbf{P}_s\right) + \nabla \cdot \left[m_s n_s \mathbf{V}_s \mathbf{V}_s \mathbf{V}_s + \left(\mathbf{V}_s \mathbf{P}_s\right)^S + \mathbf{Q}_s\right] \\ = q_s n_s \left[\mathbf{V}_s \left(\mathbf{E} + \frac{\mathbf{V}_s}{c} \times \mathbf{B}\right)\right]^S + \frac{q_s}{m_s c}\left(\mathbf{P}_s \times \mathbf{B}\right)^S,\end{aligned} \tag{3.2}$$

where the superscript S denotes symmetrization. More specifically, $(\mathbf{VP})^S_{ijk} = V_i P_{jk} + V_j P_{ik} + V_k P_{ij}$ and $(\mathbf{VE})^S_{ij} = V_i E_j + V_j E_i$, respectively. The cross product between a 2nd-rank tensor and a vector is calculated as $(\mathbf{P}_s \times \mathbf{B})_{ij} = \varepsilon_{ikl} P_{s,jk} B_l$, where ε_{ikl} is the Levi-Civita symbol. The moment variables are defined as

$$n_s = \int f_s d\mathbf{v}_s, \tag{3.3}$$

$$n_s \mathbf{V}_s = \int \mathbf{v}_s f_s d\mathbf{v}_s, \tag{3.4}$$

$$\mathbf{P}_s = m_s \int \left(\mathbf{v}_s - \mathbf{V}_s\right)\left(\mathbf{v}_s - \mathbf{V}_s\right) f_s d\mathbf{v}_s, \tag{3.5}$$

$$\mathbf{Q}_s = m_s \int \left(\mathbf{v}_s - \mathbf{V}_s\right)\left(\mathbf{v}_s - \mathbf{V}_s\right)\left(\mathbf{v}_s - \mathbf{V}_s\right) f_s d\mathbf{v}_s. \tag{3.6}$$

Note that the last term in Eq. (3.2) becomes zero if $\mathbf{P}_s$ is exactly gyrotropic. As for the derivation of the standard MHD model, let us define the one-fluid moments as

$$\rho = \sum_s m_s n_s, \tag{3.7}$$

$$\rho \mathbf{V} = \sum_s m_s n_s \mathbf{V}_s, \tag{3.8}$$

$$\rho \mathbf{V}\mathbf{V} + \mathbf{P} = \sum_s \left(m_s n_s \mathbf{V}_s \mathbf{V}_s + \mathbf{P}_s\right), \tag{3.9}$$

$$\rho \mathbf{V}\mathbf{V}\mathbf{V} + \left(\mathbf{VP}\right)^S + \mathbf{Q} = \sum_s \left[m_s n_s \mathbf{V}_s \mathbf{V}_s \mathbf{V}_s + \left(\mathbf{V}_s \mathbf{P}_s\right)^S + \mathbf{Q}_s\right]. \tag{3.10}$$

Then, it is straightforward to show that taking the sum of Eq. (3.2) for a given species s leads to

$$\frac{\partial}{\partial t}\left(\rho\mathbf{V}\mathbf{V}+\mathbf{P}\right)+\nabla\cdot\left[\rho\mathbf{V}\mathbf{V}\mathbf{V}+(\mathbf{V}\mathbf{P})^S+\mathbf{Q}\right] = \left[\mathbf{V}\left(\frac{\mathbf{J}}{c}\times\mathbf{B}\right)+\mathbf{J}\left(\mathbf{E}+\frac{\mathbf{V}}{c}\times\mathbf{B}-\frac{\mathbf{J}}{enc}\times\mathbf{B}\right)+\sum_s\Omega_{cs}\mathbf{P}_s\times\hat{\mathbf{b}}\right]^S, \tag{3.11}$$

where $\mathbf{J}=\sum_s q_s n_s \mathbf{V}_s$ is the total current density, $\Omega_{cs}=q_sB/m_sc$ is the cyclotron frequency of species s, and $\hat{\mathbf{b}}=\mathbf{B}/B$ is the unit vector parallel to the magnetic field. In this derivation, we assume quasi-neutrality, $n\simeq n_i\simeq n_e$, and neglect the electron inertial effect; i.e., we assume $m_e/m_i\ll 1$. Note that the right-hand side of Eq. (3.11) becomes much simpler by employing Ohm's law under ideal MHD or Hall-MHD ordering. The electric field related to convection, $\mathbf{E}^{\rm conv}=-(\mathbf{V}/c)\times\mathbf{B}$, and that related to the Hall effect, $\mathbf{E}^{\rm Hall}=(\mathbf{J}/enc)\times\mathbf{B}$, vanish exactly, while the effect of the electron pressure remains if Hall-MHD ordering is assumed. Another characteristic of this approach is that the trace of the right-hand side reduces to just $\mathbf{J}\cdot\mathbf{E}$, which is consistent with the conservation of kinetic and thermal energy in scalar form.

In addition to the kinetic components, we will derive the semi-conservative form using Faraday's law, which is a counterpart of the conservation law of the total energy in the standard MHD. Throughout this chapter, the factor $1/\sqrt{4\pi}$ will be absorbed into the definition of the magnetic field. After some algebra, we obtain the following equation for the ij-component,

$$\begin{aligned}&\partial_t\left(\rho V_iV_j+P_{ij}+B_iB_j\right)\\ &\quad+\partial_k\left(\rho V_iV_jV_k+P_{ij}V_k+P_{ik}V_j+P_{jk}V_i+Q_{ijk}+\mathcal{S}_{kij}+\mathcal{S}_{kji}\right)\\ &=J_i\left(E_j-E_j^{\rm conv}-E_j^{\rm Hall}\right)+J_j\left(E_i-E_i^{\rm conv}-E_i^{\rm Hall}\right)-E_l\left(\mathcal{J}_{lij}+\mathcal{J}_{lji}\right)\\ &\quad+\left(V_i\varepsilon_{jkl}J_kB_l+V_j\varepsilon_{ikl}J_kB_l\right)/c+\sum_s\Omega_{cs}\left(\varepsilon_{ikl}P_{s,jk}\hat{b}_l+\varepsilon_{jkl}P_{s,ik}\hat{b}_l\right),\end{aligned} \tag{3.12}$$

where Einstein's summation convention is applied to repeated indices. The newly introduced notations, $\mathcal{S}_{kij}$ and $\mathcal{J}_{kij}$, are defined as

$$\mathcal{S}_{kij} = c\varepsilon_{kli}E_lB_j, \tag{3.13}$$

$$\mathcal{J}_{kij} = c\varepsilon_{kli}\partial_lB_j, \tag{3.14}$$

which reduce to the Poynting flux and the current density, respectively, if one takes their trace with respect to i and j.

Eq. (3.12) is a general result, which is valid for a large mass ratio or, in other words, when the scale size of the system is much larger than the electron skin depth. In the particular case where ideal MHD ordering can be reasonably applied, that is, where all temporal and spatial scales are much larger than the cyclotron period and the inertial length of the ions, respectively, we can employ the simplest form of Ohm's law,

$$\mathbf{E} + \frac{\mathbf{V}}{c} \times \mathbf{B} = 0. \tag{3.15}$$

The right-hand side of Eq. (3.12), except for the last two terms related to the cyclotron frequencies, is then simplified to

$$V_k \partial_k \left(B_i B_j \right) - V_i \partial_j \left(\frac{B^2}{2} \right) - V_j \partial_i \left(\frac{B^2}{2} \right). \tag{3.16}$$

Again, Eq. (3.16) reduces to zero by taking the trace. Inclusion of other physics such as finite resistivity and the Hall effect is straightforward by direct application of Eq. (3.12) and appropriate modification of Ohm's law.

In this chapter, for simplicity we will neglect the generalized heat-flux tensor, $\mathbf{Q}$. Generally speaking, it is very common for a collisionless plasma to not reach local thermodynamic equilibrium, and its deviation from the Maxwellian distribution plays a crucial role in dynamical phenomena in collisionless systems. Nevertheless, since the purpose of this chapter is to develop a method to treat anisotropic pressure, we do not take into account the heat-flux tensor. If one wants to include the effects of the heat flux, $\mathbf{Q}$ should be determined by incorporating an appropriate closure model (e.g., Hesse et al., 2004; Wang et al., 2015).

3.2.2 Gyrotropization model

The last two terms in Eq. (3.12) contain the cyclotron frequencies, Ω_{cs}, which cannot be resolved under MHD ordering. Therefore, these terms may be replaced by an effective collision model. Hada et al. (1999) describe a gyrotropization model for an anisotropic pressure tensor, which assumes that the pressure tensor approaches the gyrotropic tensor, $\mathbf{P}_g = P_\perp \mathbf{I} + \left(P_{||} - P_\perp \right) \hat{\mathbf{b}}\hat{\mathbf{b}}$, within a certain relaxation timescale. The functional form of

the collision operator used here is

$$\left[\frac{\partial \mathbf{P}}{\partial t}\right]_{\text{collision}} = -\nu_g \left(\mathbf{P} - \mathbf{P}_g\right). \tag{3.17}$$

The effective collision frequency, $\nu_g = \nu_g(B)$, is a function of the local magnetic-field strength and must be much higher than the system's highest frequency. While Hada et al. (1999) adopted a constant ν_g in both space and time, we assume that ν_g is proportional to the local magnetic-field strength, because the original timescale is determined by the cyclotron period. This dependence on the magnetic field is consistent with the physical insight that finite non-gyrotropy will remain in unmagnetized regions because of the absence of any cyclotron motion.

Employment of the effective collision model successfully eliminates any scales related to the cyclotron motion, and we can thus solve the set of basic equations in the framework of only fluid-based variables. Moreover, it is remarkable that, by introducing the non-gyrotropic pressure tensor and the gyrotropization model described here, any numerical difficulty in dealing with magnetically neutral regions, or singularities at magnetic null points, is completely removed. In other words, the system is regularized by our model. Although we still need to determine the direction of the local magnetic field to calculate an asymptote in the collision model, the gyrotropic pressure will never be used at magnetic null points because ν_g vanishes there owing to the assumption that $\nu_g \propto B$.

To clarify the asymptotic behavior of our regularization model, let us consider a few extreme cases. When a plasma is threaded by a sufficiently strong magnetic field, the effective gyrotropization frequencies are much higher than any dynamical frequencies, which leads the system to display double adiabatic behavior in an asymptotic manner. Given that in this case our regularization procedure does nothing other than make the relaxation timescale sufficiently short, the result does not change from the case when instantaneous gyrotropization, or the double adiabatic approximation, is assumed.

Next, let us consider the opposite case, that is, when the magnetic field is nearly neutral. A model without implementation of our regularization, such as the classical CGL model, assumes instantaneous gyrotropization even if the gyro-period may become comparable to or even longer than the dynamical time. This leads to a singularity related to the division by zero, which results in difficulties in constructing a robust numerical model. Indeed, such a model does not have any physical basis. The gyrotropization model

proposed here, on the other hand, retrieves the regularity at magnetic null points by allowing each component of the gas pressure to evolve individually, without imposing any relaxation processes. Since the gas obeys the 2nd-order moment equation derived from the Vlasov equation, the moment variables will evolve appropriately within the applicability of closure models of the moment hierarchy.

Note that the regularization procedure described here may be closely related to an AP scheme, which was first proposed by Jin (1999). This allows us to apply the same scheme to solve the equations in regions characterized by a wide range of perturbation parameters. For instance, Degond et al. (2009) provided a method to handle the fluid equations for a plasma containing a strong magnetic field in an AP manner, where the perturbation parameter ε representing the non-dimensional gyro-period can attain both a finite value and an arbitrary infinitesimal. Our framework presented here, on the other hand, could be interpreted as applicable to the opposite limit, where the gyro-period can have both finite and infinite values. For details about AP schemes for plasmas, see Degond (2013) for example.

To conclude this section, all governing equations employed in the present model are summarized here. We solve the set of (generalized) conservation laws for the mass, momentum, and total energy, as well as the induction equation under ordering of an ideal MHD,

$$\frac{\partial \rho}{\partial t} + \nabla \cdot (\rho \mathbf{V}) = 0, \tag{3.18}$$

$$\frac{\partial (\rho \mathbf{V})}{\partial t} + \nabla \cdot \left(\rho \mathbf{V}\mathbf{V} + \mathbf{P} + \frac{B^2}{2}\mathbf{I} - \mathbf{B}\mathbf{B} \right) = 0, \tag{3.19}$$

$$\frac{\partial \mathbf{B}}{\partial t} = \nabla \times (\mathbf{V} \times \mathbf{B}), \tag{3.20}$$

$$\begin{aligned} &\frac{\partial}{\partial t}\left(\rho V_i V_j + P_{ij} + B_i B_j\right) + \partial_k \left[\rho V_i V_j V_k + P_{ij} V_k + P_{ik} V_j + P_{jk} V_i + \mathcal{S}_{kij} + \mathcal{S}_{kji}\right] \\ &= B_i V_k \partial_k B_j + B_j V_k \partial_k B_i - B_k V_i \partial_j B_k - B_k V_j \partial_i B_k - \nu_g \left(P_{ij} - P_{g,ij}\right). \end{aligned} \tag{3.21}$$

As the pressure tensor is symmetric by definition, we have a total of 13 independent variables: i.e, $\rho, V_x, V_y, V_z, B_x, B_y, B_z, P_{xx}, P_{yy}, P_{zz}, P_{xy}, P_{yz}$, and P_{zx}.

3.3 Numerical implementation

This section describes our model implementation. Existing MHD codes written in conservative forms can be readily extended to the present model by introducing slight modifications, because we can derive the basic equations in the form of semi-conservation laws accompanied by several directional energy-exchange terms and a collision term. Here we describe the spatial and temporal 2nd-order finite-difference algorithms and highlight the differences with respect to standard MHD codes. Unless otherwise stated, test problems described in the next section employ this 2nd-order implementation. Of course, other methods, such as finite-volume approaches, can be used as well.

In the following, for simplicity let us consider a one-dimensional case and formulate the combination of equations (3.18) – (3.21) as

$$\frac{\partial \mathbf{U}}{\partial t} + \frac{\partial \mathbf{F}}{\partial x} + \mathbf{A}\frac{\partial \mathbf{U}}{\partial x} = -\nu_g \left(\mathbf{U} - \mathbf{U}_g\right), \tag{3.22}$$

where $\mathbf{U} = \{\rho,\ \rho\mathbf{V},\ \mathbf{B},\ \rho\mathbf{V}\mathbf{V} + \mathbf{P} + \mathbf{B}\mathbf{B}\} \in \mathbb{R}^{13}$ contains conservative variables, and $\mathbf{A} \in \mathbb{R}^{13} \times \mathbb{R}^{13}$ describes the energy-exchange terms. Note that $\mathbf{A}$ has non-zero elements only in relation to equation (3.21) and all elements are composed of the products of the velocity and the magnetic field, $V_\alpha B_\beta$.

Extension to a multi-dimensional problem is straightforward, while the numerical divergence error of the magnetic field must be resolved similarly as for standard MHD. In our code, the constrained transport (CT) treatment (Evans & Hawley, 1988; Tóth, 2000) is adopted to avoid this problem. In particular, we used the Harten-Lax-van Leer (HLL) upwind-CT method (Londrillo & del Zanna, 2004; Amano, 2015), where the electric fields are interpolated to the edge centers using the same interpolation scheme as used for other fluid variables and the HLL approximate Riemann solver (Harten et al., 1983). One may employ any other divergence cleaning techniques, as the present model does not alter the properties of the induction equation.

3.3.1 Conservative part

We solve equation (3.22) by splitting the operator into three parts: i.e., a conservative term $\partial\mathbf{F}/\partial x$, a non-conservative term $\mathbf{A}\partial\mathbf{U}/\partial x$, and an effective collision term $-\nu_g\left(\mathbf{U} - \mathbf{U}_g\right)$. In this subsection, we first review the integration method for the conservative part.

Let us consider an equally spaced one-dimensional computational domain, where the

range of the j-th cell is denoted as $x \in [x_j - \Delta x/2, x_j + \Delta x/2]$ with mesh size Δx. All primitive variables $\mathbf{W} = \{\rho,\ \mathbf{V},\ \mathbf{B},\ \mathbf{P}\}$ are defined at each cell center, x_j, as point values. Then, $\mathbf{W}_j$ is interpolated linearly to the face center, $x_{j\pm1/2}$, using the minmod limiter to suppress numerical oscillations around discontinuities. Once the left and right states across the cell faces $\{\mathbf{W}_{L,R}\}$ have been interpolated, we can immediately obtain the corresponding conservative variables and fluxes, $\{\mathbf{U}_{L,R}\}$ and $\{\mathbf{F}_{L,R}\}$, respectively.

Next, we consider a self-similarly expanding Riemann fan at the cell face. The outermost signal speeds in the present system can be evaluated by considering the largest and smallest eigenvalues of the matrix $(\partial\mathbf{F}/\partial\mathbf{U}) + \mathbf{A}$, where $\partial\mathbf{F}/\partial\mathbf{U}$ is a Jacobian matrix, as follows:

$$\begin{aligned} \lambda^{\pm}(\mathbf{U}) &= V_x \pm \sqrt{b + \sqrt{b^2 - c}}, \\ b &= \frac{1}{2\rho}\left(4P_{xx} + B^2\right), \\ c &= \frac{1}{\rho^2}\left[\left(3P_{xx} + B_y^2 + B_z^2\right)\left(P_{xx} + B_x^2\right)\right. \\ &\quad + \left(2P_{xy} - B_xB_y\right)B_xB_y \\ &\quad \left. + \left(2P_{xz} - B_xB_z\right)B_xB_z\right]. \end{aligned} \tag{3.23}$$

These are the counterparts to fast magnetosonic waves in standard MHD. We define the left- and rightward expansion speeds of the Riemann fan in the form of their absolute values,

$$s_L = \left|\min\left\{0, \lambda^-(\mathbf{U}_L), \lambda^-(\mathbf{U}_R)\right\}\right|, \tag{3.24}$$

$$s_R = \left|\max\left\{0, \lambda^+(\mathbf{U}_L), \lambda^+(\mathbf{U}_R)\right\}\right|. \tag{3.25}$$

As in the usual implementation, s_L and s_R are chosen such that they tend to zero in supersonic cases.

Denoting the intermediate state inside the Riemann fan as $\mathbf{U}_*$, the conservative and non-conservative parts in equation (3.22) can be integrated over a control volume, $(x,t) \in [-Ts_L, Ts_R] \times [0,T]$, resulting in

$$\mathbf{U}_*(s_R + s_L) - (\mathbf{U}_R s_R + \mathbf{U}_L s_L) + (\mathbf{F}_R - \mathbf{F}_L) + \int_{\mathbf{U}_L}^{\mathbf{U}_R} \mathbf{A}(\mathbf{U})\, d\mathbf{U} = 0, \tag{3.26}$$

where the last term on the left-hand side requires an integral along a phase-space path from

a left state through a right state. Following the path-conservative HLL scheme proposed by Dumbser & Balsara (2016), we evaluate this integral by assuming two piecewise linear paths from $\mathbf{U}_L$ to $\mathbf{U}_*$, and from $\mathbf{U}_*$ to $\mathbf{U}_R$, respectively. This linear segment assumption immediately leads to an implicit equation for $\mathbf{U}_*$,

$$\begin{aligned}&\mathbf{U}_* (s_R + s_L) - (\mathbf{U}_R s_R + \mathbf{U}_L s_L) + (\mathbf{F}_R - \mathbf{F}_L) \\ &+\tilde{\mathbf{A}} (\mathbf{U}_L, \mathbf{U}_*) (\mathbf{U}_* - \mathbf{U}_L) + \tilde{\mathbf{A}} (\mathbf{U}_*, \mathbf{U}_R) (\mathbf{U}_R - \mathbf{U}_*) = 0,\end{aligned} \tag{3.27}$$

with

$$\tilde{\mathbf{A}} (\mathbf{U}_a, \mathbf{U}_b) = \int_0^1 \mathbf{A} (\mathbf{U}_a + (\mathbf{U}_b - \mathbf{U}_a) s) \, ds. \tag{3.28}$$

In our implementation, the integral over s is calculated by means of a three-point Gaussian quadrature. Equation (3.27) must, in general, be solved iteratively for $\mathbf{U}_*$. In the present system, however, we do not need to iterate in practice, as $\tilde{\mathbf{A}} (\mathbf{U}_a, \mathbf{U}_b) (\mathbf{U}_b - \mathbf{U}_a)$ can be evaluated only for ρ_*, $(\rho \mathbf{V})_*$, and $\mathbf{B}_*$, which are obtained explicitly from equation (3.27). For more details about the path-conservative HLL scheme, see Dumbser & Balsara (2016).

Using the intermediate state obtained above, we can calculate the path-conservative HLL fluctuations—which quantify the modification of the flux from the original point-value flux—as

$$\mathbf{D}_L = \frac{s_L}{s_R + s_L} \left[\mathbf{F}_R - \mathbf{F}_L - s_R (\mathbf{U}_R - \mathbf{U}_L) + \mathbf{D}_A \right], \tag{3.29}$$

$$\mathbf{D}_R = \frac{s_R}{s_R + s_L} \left[\mathbf{F}_R - \mathbf{F}_L + s_L (\mathbf{U}_R - \mathbf{U}_L) + \mathbf{D}_A \right], \tag{3.30}$$

where the contribution from the non-conservative term is

$$\mathbf{D}_A = \tilde{\mathbf{A}} (\mathbf{U}_L, \mathbf{U}_*) (\mathbf{U}_* - \mathbf{U}_L) + \tilde{\mathbf{A}} (\mathbf{U}_*, \mathbf{U}_R) (\mathbf{U}_R - \mathbf{U}_*). \tag{3.31}$$

Finally, the conservative part in equation (3.22) can be discretized as

$$\frac{\partial \mathbf{U}_j}{\partial t} + \frac{1}{\Delta x} \left(\mathbf{F}_{L,j+1/2} - \mathbf{F}_{R,j-1/2} \right) + \frac{1}{\Delta x} \left(\mathbf{D}_{L,j+1/2} + \mathbf{D}_{R,j-1/2} \right) = 0. \tag{3.32}$$

In particular, if the non-conservative terms are not present, or if $\mathbf{D}_A = 0$, this scheme simply reduces to the usual HLL scheme with $\mathbf{F}_{\mathrm{HLL}} = \mathbf{F}_L + \mathbf{D}_L = \mathbf{F}_R - \mathbf{D}_R$.

3.3.2 Energy exchange part

While considering an intermediate state inside an expanding Riemann fan in the previous subsection, the effects of non-conservative terms, $\mathbf{A}\left(\partial\mathbf{U}/\partial x\right)$, were also taken into account to maintain consistency of the hyperbolic system. This only applies, however, to the determination of the conservative flux, and time integration of the non-conservative terms must be carried out separately.

This evaluation requires calculating the magnetic field's derivatives. For the purpose of avoiding spurious oscillations near discontinuities, one may need to carry out this evaluation using an appropriate limiter function. Our implementation simply adopts the minmod limiter, spatially discretized as

$$\frac{\partial\mathbf{U}_j}{\partial t}+\mathbf{A}_j\frac{1}{\Delta x}\text{minmod}\left(\mathbf{U}_{j+1}-\mathbf{U}_j,\mathbf{U}_j-\mathbf{U}_{j-1}\right)=0. \tag{3.33}$$

Then, it is straightforward to temporally integrate both equations (3.32) and (3.33) by means of the 2nd-order total variation diminishing (TVD) Runge-Kutta method (Shu & Osher, 1988),

$$\mathbf{U}^{*} = \mathbf{U}^{n}-\Delta t\mathcal{L}\left(\mathbf{U}^{n}\right), \tag{3.34}$$

$$\mathbf{U}^{n+1} = \frac{1}{2}\mathbf{U}^{n}+\frac{1}{2}\left[\mathbf{U}^{*}-\Delta t\mathcal{L}\left(\mathbf{U}^{*}\right)\right], \tag{3.35}$$

where

$$\mathcal{L}\left(\mathbf{U}\right)=\frac{\partial\mathbf{F}\left(\mathbf{U}\right)}{\partial x}+\mathbf{A}\left(\mathbf{U}\right)\frac{\partial\mathbf{U}}{\partial x}. \tag{3.36}$$

The time interval, Δt, is determined to satisfy the CFL condition for the fastest propagating waves,

$$\Delta t\leq\nu\frac{\Delta x}{\max_j\left\{\left|\lambda^{+}\left(\mathbf{U}_j\right)\right|,\left|\lambda^{-}\left(\mathbf{U}_j\right)\right|\right\}} \tag{3.37}$$

where ν is a safety parameter set to $\nu=0.4$ in this chapter.

3.3.3 Effective collision part

After calculating the pressure tensor based on the updated conservative variables, the effective collision model, equation (3.17), is applied at every time step and at every grid

point. The procedure starts from the determination of the direction of the magnetic field, $\hat{\mathbf{b}} = \mathbf{B}/B$, at each site. Note that, as stated in the previous section, we do not require $\hat{\mathbf{b}}$ in unmagnetized regions, since there the effective collision frequency becomes exactly zero, and therefore no singularity owing to division by zero exists.

Our actual implementation is as follows. The pressure tensor defined in xyz space is rotated to the coordinate system aligned with the local magnetic field, so that the index 1 represents the direction parallel to $\hat{\mathbf{b}}$, and indices 2 and 3 correspond to two different perpendicular directions. Then, the gyrotropic asymptote, $\mathbf{P}_g$, can be defined as

$$\mathbf{P}_g = P_\perp \mathbf{I} + \left(P_{||} - P_\perp\right) \hat{\mathbf{b}}\hat{\mathbf{b}}, \tag{3.38}$$

with

$$P_{||} = P_{11}, \quad P_\perp = \frac{P_{22} + P_{33}}{2}. \tag{3.39}$$

Alternatively, if one does not need any other components except for the parallel and perpendicular ones, the simpler expressions

$$P_{||} = \hat{\mathbf{b}} \cdot \mathbf{P} \cdot \hat{\mathbf{b}} \text{ and } \quad P_\perp = \frac{\mathrm{Tr}\mathbf{P} - P_{||}}{2}, \tag{3.40}$$

can also be used. Note that by enforcing isotropy, $P_{||} = P_\perp = \mathrm{Tr}\mathbf{P}/3$, the model will reduce to the standard MHD limit.

Once the gyrotropic asymptote has been determined, we use the exact solution to equation (3.17) to avoid explicit integration of a stiff equation,

$$\mathbf{P}\left(t + \Delta t\right) = \mathbf{P}_g + \left(\mathbf{P}\left(t\right) - \mathbf{P}_g\right) e^{-\nu_g \Delta t}, \tag{3.41}$$

which is applied for every sub-cycle of the Runge-Kutta time integration.

3.3.4 Summary of the numerical method

We have discussed separately the integration method of each term following the spirit of an operator splitting technique. It is useful to summarize our implementation here. The procedure followed for one Runge-Kutta subcycle proceeds as follows:

1. Convert all conservative variables defined at cell centers $\{\mathbf{U}\}$ to primitive variables

$\{\mathbf{W}\}$.

2. Interpolate $\{\mathbf{W}\}$ into cell faces to evaluate $\{\mathbf{W}_{L,R}\}$.

3. Calculate the corresponding conservative variables $\{\mathbf{U}_{L,R}\}$, fluxes $\{\mathbf{F}_{L,R}\}$, and expansion speeds $\{s_{L,R}\}$.

4. Solve equation (3.27) for the intermediate state $\{\mathbf{U}_*\}$.

5. Obtain HLL fluctuations $\{\mathbf{D}_{L,R}\}$ through equations (3.29) and (3.30).

6. Define the matrix $\{\mathbf{A}_j\}$ required for evaluation of the non-conservative term.

7. Integrate equations (3.32) and (3.33) simultaneously as follows:

$$\begin{aligned}\mathbf{U}^{r+1} = \mathbf{U}^{r} \quad &- \quad \frac{\Delta t}{\Delta x}\left(\mathbf{F}_{L,j+1/2} - \mathbf{F}_{R,j-1/2}\right) \\ &- \quad \frac{\Delta t}{\Delta x}\left(\mathbf{D}_{L,j+1/2} + \mathbf{D}_{R,j-1/2}\right) \\ &- \quad \mathbf{A}_j \frac{\Delta t}{\Delta x}\mathrm{minmod}\left(\mathbf{U}_{j+1} - \mathbf{U}_j, \mathbf{U}_j - \mathbf{U}_{j-1}\right) \end{aligned} \tag{3.42}$$

   where r represents the substep index of the Runge-Kutta procedure.

8. Define parallel and perpendicular pressures, $P_{||,\perp}$ using equation (3.39) or (3.40).

9. Gyrotropize the pressure tensor with the solution (3.41) depending on the local magnetic-field strength.

10. Isotropize the pressure tensor if necessary.

11. Set boundary conditions.

This subcycle is repeated twice in each 2nd-order Runge-Kutta cycle for computing $\mathbf{U}^n - \Delta t\mathcal{L}\left(\mathbf{U}^n\right)$ and $\mathbf{U}^* - \Delta t\mathcal{L}\left(\mathbf{U}^*\right)$ in equations (3.34) and (3.35), respectively. The procedure described here can easily be extended to multi-dimensional problems in a dimension-by-dimension fashion, because our implementation is based on the finite-difference approach.

Note that the fluxes and the fluctuations here are defined as point values. Since the present implementation only has second-order accuracy in space, the point-value and numerical fluxes are identical. If one desires to use a higher than second-order accuracy scheme, however, an appropriate conversion formula from the point-value to the numerical flux must be applied (Shu & Osher, 1988). In Appendix A, we describe an example of

a higher-order implementation using the 5th-order weighted essentially non-oscillatory (WENO) scheme (Jiang & Shu, 1996) and a 3rd-order TVD Runge-Kutta scheme (Shu & Osher, 1988).

3.4 Test problems

This section explores a series of test problems, including one-, two-, and three-dimensional applications. In addition to non-gyrotropic cases, we will place a certain degree of emphasis on gyrotropic and isotropic limits, which can be compared with published results.

3.4.1 Circularly polarized Alfvén waves

First, in this subsection, we demonstrate the numerical convergence of our model in the limit of fast isotropization and fast gyrotropization. In these two asymptotic cases, we can derive an exact solution for finite-amplitude circularly polarized Alfvén waves propagating along ambient magnetic field. In the isotropic MHD limit, the well-known exact solution for Alfvén waves propagating in the x direction is

$$V_y = \delta V \sin(kx - \omega t), \quad V_z = \delta V \cos(kx - \omega t), \tag{3.43}$$

$$B_y = \delta B \sin(kx - \omega t), \quad B_z = \delta B \cos(kx - \omega t), \tag{3.44}$$

for constant density, pressure, normal velocity, and a normal magnetic field. The amplitudes of the velocity and the magnetic field are related through the Walen relation,

$$\frac{\delta V}{V_A} = \frac{\delta B}{B_x}. \tag{3.45}$$

In the gyrotropic MHD limit, on the other hand, the pressure anisotropy modulates the effective strength of the magnetic tension force by a factor of $\varepsilon = 1 - \left(P_{||} - P_{\perp}\right)/B^2$ with respect to standard MHD. This modulation leads to a modified Alfvén velocity, $V_A^* = \sqrt{\varepsilon} V_A$, and the original Alfvén velocity V_A in the Walen relation (3.45) should also be replaced by V_A^*.

In this test we employ the following initial parameters for an ambient plasma: $\rho = 1$, $P = 1$, $V_x = 0$ and $B_x = 1$. For waves, we assume $\delta B = 0.1$ and $k = (2\pi)^{-1}$. In each gyrotropic run, a specific value of ε is adopted, and the initial $P_{||}$ and $P_{\perp}$ are calculated so that the average pressure $\overline{P} = \left(P_{||} + 2P_{\perp}\right)/3$ is identical to P for the relevant ε. Note

that while $P_{||}$ and $P_{\perp}$ are spatially constant, each component of the gyrotropic pressure tensor, $\mathbf{P} = P_{\perp}\mathbf{I} + \left(P_{||} - P_{\perp}\right)\mathbf{BB}/B^2$, varies spatially, because it is a function of the local magnetic field, including the wave components. The domain size is unity, $L_x = 1$, which corresponds to one wavelength. We stop the simulation after five periods, $t = 5L_x/V_A^*$, and compute the errors by comparing the final state with the initial conditions.

The results are summarized in Table 3.1. We list the errors and the orders for four cases: i.e., the isotropic MHD limit and the gyrotropic MHD limit for three different initial values of ε. In the isotropic run we observe nearly 2nd-order convergence, particularly for the L_1 norm. The reduction of the order by 0.1-0.2 may be attributed to the effects of operator splitting in the collision model. The gyrotropic runs show somewhat worse convergence. We regard this deviation as a result of selective heating of the perpendicular pressure through numerical dissipation. The wave variations in this test are driven by the y and z components of the velocity and the magnetic field, dissipation of which heats the perpendicular temperature more efficiently, because the normal magnetic field is relatively large compared with the wave field. The background value of ε, which increases with time, causes the propagation speed of the Alfvén wave to become slightly faster, which leads to a small gap between the five modulated periods and the exact end time of our simulation. This discrepancy, then, may be remedied by employing a less dissipative limiter, like a superbee limiter function, or by employing a higher-order interpolation scheme.

3.4.2 Shock tube problem

3.4.2.1 Fast isotropization

Analysis results of the shock tube problem described by Brio & Wu (1988) are discussed in this subsection. The shock tube problem is one of the most widely used test problems for MHD system, in particular, for checking the accuracy and resolution of propagating waves, including discontinuities such as shock waves and contact discontinuities.

A one-dimensional simulation domain with $x \in [-1, 1]$ is discretized by defining 1000 equally spaced grid points. The initial state is given as

$$(\rho, V_x, V_y, V_z, B_y, B_z, P) = \begin{cases} (1.0, 0.0, 0.0, 0.0, 1.0, 0.0, 1.0) & (x \leq 0), \\ (0.125, 0.0, 0.0, 0.0, -1.0, 0.0, 0.1) & (x > 0). \end{cases} \tag{3.46}$$

The normal component of the magnetic field, B_x, is constant in time and space, $B_x = 0.75$,

Table 3.1: Circularly polarized Alfvén waves for five periods

		L_1		L_∞	
Run	N_x	Error	Order	Error	Order
Isotropic	16	5.94×10^{-2}	—	9.16×10^{-2}	—
	32	3.15×10^{-2}	0.92	5.50×10^{-2}	0.74
	64	9.57×10^{-3}	1.72	2.30×10^{-2}	1.26
	128	4.21×10^{-3}	1.18	9.55×10^{-3}	1.27
	256	1.12×10^{-3}	1.91	3.78×10^{-3}	1.34
	512	3.17×10^{-4}	1.82	1.36×10^{-3}	1.48
Gyrotropic ($\varepsilon = 1.00$)	16	5.95×10^{-2}	—	9.16×10^{-2}	—
	32	3.29×10^{-2}	0.85	5.51×10^{-2}	0.73
	64	1.12×10^{-2}	1.55	2.23×10^{-2}	1.30
	128	4.13×10^{-3}	1.44	8.22×10^{-3}	1.44
	256	1.43×10^{-3}	1.53	3.02×10^{-3}	1.44
	512	4.76×10^{-4}	1.59	9.27×10^{-4}	1.70
Gyrotropic ($\varepsilon = 0.81$)	16	6.12×10^{-2}	—	9.41×10^{-2}	—
	32	3.71×10^{-2}	0.72	6.07×10^{-2}	0.63
	64	1.34×10^{-2}	1.46	2.49×10^{-2}	1.28
	128	4.70×10^{-3}	1.52	9.45×10^{-3}	1.40
	256	1.73×10^{-3}	1.44	1.44×10^{-3}	1.63
	512	6.04×10^{-4}	1.52	9.97×10^{-4}	1.61
Gyrotropic ($\varepsilon = 1.21$)	16	5.72×10^{-2}	—	8.84×10^{-2}	—
	32	2.88×10^{-2}	0.99	4.96×10^{-2}	0.83
	64	9.33×10^{-3}	1.63	2.00×10^{-2}	1.31
	128	3.61×10^{-3}	1.37	7.77×10^{-3}	1.37
	256	1.15×10^{-3}	1.65	2.95×10^{-3}	1.40
	512	3.60×10^{-4}	1.68	9.75×10^{-4}	1.60

because of the constraint $\nabla \cdot \mathbf{B} = 0$. As we now have to provide the gas pressure in tensor form, let us assume that the initial plasma has an isotropic distribution in velocity space, that is, $\mathbf{P} = P\mathbf{I}$ at $t = 0$. Next, we integrate the governing equations (3.18)–(3.21) until $t = 0.2$.

Fig. 3.1 shows the results under an isotropic limit. In addition to gyrotropization, fast isotropization is also assumed by enforcing $P_{||} = P_\perp$ in equation (3.39), as described in

section 3.3.3. The solid line overplotted in each panel represents the reference solution, which was calculated using the Athena code with 20000 grid points (Stone et al., 2008). The solution under the isotropic limit converges properly to the standard MHD result. A pair of fast rarefaction waves propagate in both directions at first, each followed by a slow shock and a slow-mode compound wave. Between these slow-mode related waves, a contact discontinuity is formed, where only the density profile exhibits a discontinuous jump. Note that the effective adiabatic index is $\gamma = 5/3$ rather than $\gamma = 2$ as pertaining to the original problem setting. Nevertheless, the basic structure is still rather similar for both problem settings, except for a slight modification of the wave propagation speeds.

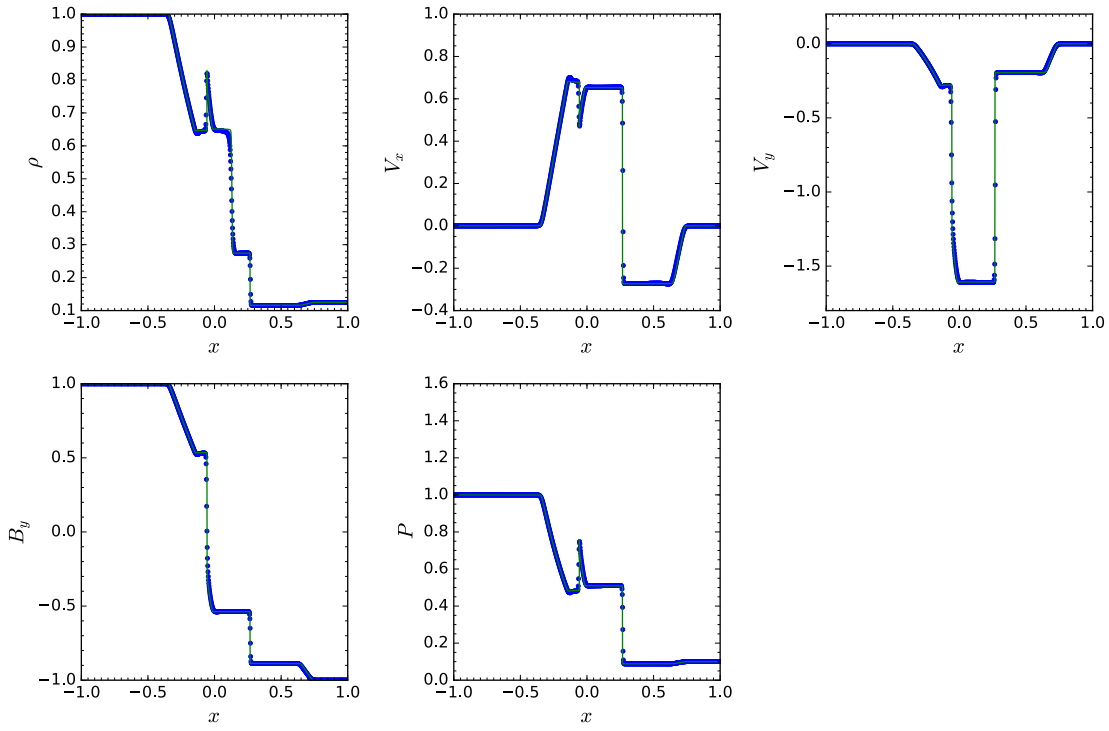

Figure 3.1: Brio-Wu shock tube problem under an isotropic MHD limit. The data have been taken at $t = 0.2$. The solid line overplotted in each panel is the reference solution, calculated using the Athena code with 20000 grid points. In the reference run, a Roe approximate Riemann solver, piecewise constant interpolation, and a corner-transport upwind integrator are employed.

3.4.2.2 Fast gyrotropization

Next, we consider the case under the gyrotropic limit. Although the present formulation preserves the total energy exactly, the amount of heating caused by numerical viscosity and resistivity distributed to each pressure component cannot be determined self-consistently.

This results in the absence of exact Rankine-Hugoniot jump conditions and a dependency of the solutions on the numerical schemes employed in a specific code. One possible approach to avoid this undesired dependency is by incorporating viscosity and/or resistivity models that describe the heating rate in any direction. The simplest assumption regarding resistivity is, for example, the isotropic heating: i.e., one-third of the Joule heating is deposited equally in each P_{xx}, P_{yy}, and P_{zz}, based on the physical consideration that resistive heating is mainly carried by electrons, which may isotropize much faster than the dynamical timescale. Nevertheless, we particularly focus on the ideal Ohm's law to demonstrate the capability of our model to track dynamical developments.

The results under the gyrotropic constraints are plotted in Fig. 3.2, using the same format as in Fig. 3.1. Note that since the simulation domain includes a finite magnetic field throughout and because we assume a very high gyrotropization rate, the governing equations reduce asymptotically to the double adiabatic approximation or CGL limit. There is, unfortunately, no reference solution to which we can reasonably compare our nearly double adiabatic results, so here we only address the most notable differences from the isotropic case.

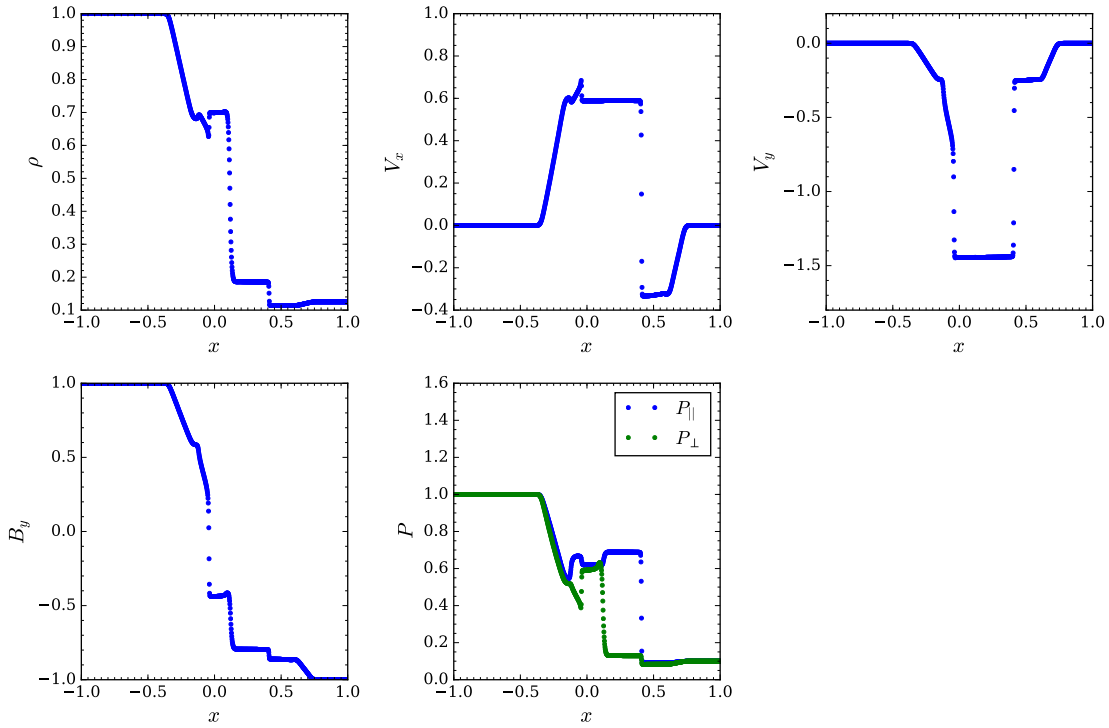

Figure 3.2: Brio-Wu shock tube problem under the gyrotropic MHD limit. The data have been taken at $t = 0.2$.

One noteworthy difference is that the contact discontinuity around $x \sim 0.2$ involves variations not only in ρ but also in B_y, $P_{||}$, and $P_\perp$. This modified jump condition can be understood from the momentum conservation law applied across a boundary without mass flux,

$$\left[P_\perp + \frac{B^2}{2} - \left(1 - \frac{P_{||} - P_\perp}{B^2}\right) B_x^2\right]_1^2 = 0, \tag{3.47}$$

$$\left[-\left(1 - \frac{P_{||} - P_\perp}{B^2}\right) B_x B_y\right]_1^2 = 0, \tag{3.48}$$

where $[X]_1^2 = X_2 - X_1$ indicates a difference between two spatially separated regions. These relations imply that the total pressure, $P_\perp + B^2/2$, and the tangential magnetic field, B_y, may change across the boundary if the pressure anisotropy also changes while satisfying the conservation laws. As regards linear waves, a newly introduced degree of freedom related to the pressure anisotropy produces a different kind of entropy waves, whose eigenfunction can have perturbations associated with the pressure and the magnetic field.

Another notable feature is the selective enhancement of the parallel pressure across the slow shock. This *firehose*-type anisotropy is consistent with being a direct consequence of the conservation of the first and second adiabatic invariants. The combination of the first and second adiabatic invariants, $P_\perp/(\rho B) = \text{const.}$ and $B^2 P_{||}/\rho^3 = \text{const.}$, tells us that, in the context of the motion of a fluid element, increasing density and decreasing magnetic-field strength lead to a significant enhancement of the parallel pressure. The first adiabatic invariant, on the other hand, implies that the perpendicular pressure is proportional to the product of the density and the magnetic-field strength, which results in a smaller increase in the perpendicular pressure across the slow shock.

Once again, we emphasize that the present test should not show any significant differences between cases with and without implementation of our regularization procedure, because the simulation domain does not contain any magnetic null points due to the prevailing constant and uniform normal field.

3.4.2.3 Without gyrotropization

Our implementation works well, even when gyrotropization is completely turned off, i.e. $\nu_g = 0$. Note that in the conventional framework for dealing with anisotropic pressure without our regularization, there is no counterpart to compare with the solution presented

here. This problem is intended purely for testing the implementation's numerical robustness and capabilities. Although we only provide the results for the ideal Ohm's law here for theoretical simplicity, a more general electric field can be employed in a straightforward manner by implementing equation (3.12) instead of (3.21).

Roughly speaking, the qualitative behavior discussed above does not change significantly even without gyrotropization. The profiles of the variables in this case are shown in Fig. 3.3. Again, the wave structure consists of a pair of fast rarefaction waves, slow-mode shock and compound waves, and a contact discontinuity accompanied by variations in the tangential magnetic field and the pressure anisotropy. Note that in one-dimensional problems, P_{yy} and P_{zz} only act as passive variables described by

$$\frac{\partial P_{ii}}{\partial t} + \frac{\partial}{\partial x}\left(V_x P_{ii}\right) + 2P_{ix}\frac{\partial V_i}{\partial x} = 0, \tag{3.49}$$

where $i = y, z$, so the relatively large jump of P_{yy} across the contact discontinuity, for instance, cannot have a back reaction to the plasma flow. In particular, the coplanarity in the present setup (i.e., $V_z = 0$ and $B_z = 0$) reduces the energy equation about the zz component to a simple continuity equation for P_{zz}, which makes the behavior of P_{zz} quantitatively the same as that of ρ.

3.4.3 One-dimensional reconnection layer

This subsection provides another set of solutions to the one-dimensional Riemann problem described by Hirabayashi & Hoshino (2013) (hereafter HH13), who discussed the wave structure in a self-similarly developing reconnection layer by focusing on the properties of slow-mode and Alfvén waves under the double adiabatic approximation (i.e., the gyrotropic limit). In contrast to the coplanar case discussed in the previous subsection, we focus particularly on the non-coplanar problem, where the degeneracy of a shear Alfvén wave and other modes may be removed.

The initial condition is an isotropic and isothermal Harris-type current sheet with a uniform guide field,

$$B_y\left(x\right) = B_0\ \cos\phi\ \tanh\left(x/L\right), \tag{3.50}$$

$$B_z\left(x\right) = B_0\ \sin\phi, \tag{3.51}$$

where B_0 is the magnetic field strength in the lobe region, ϕ is the angle between the

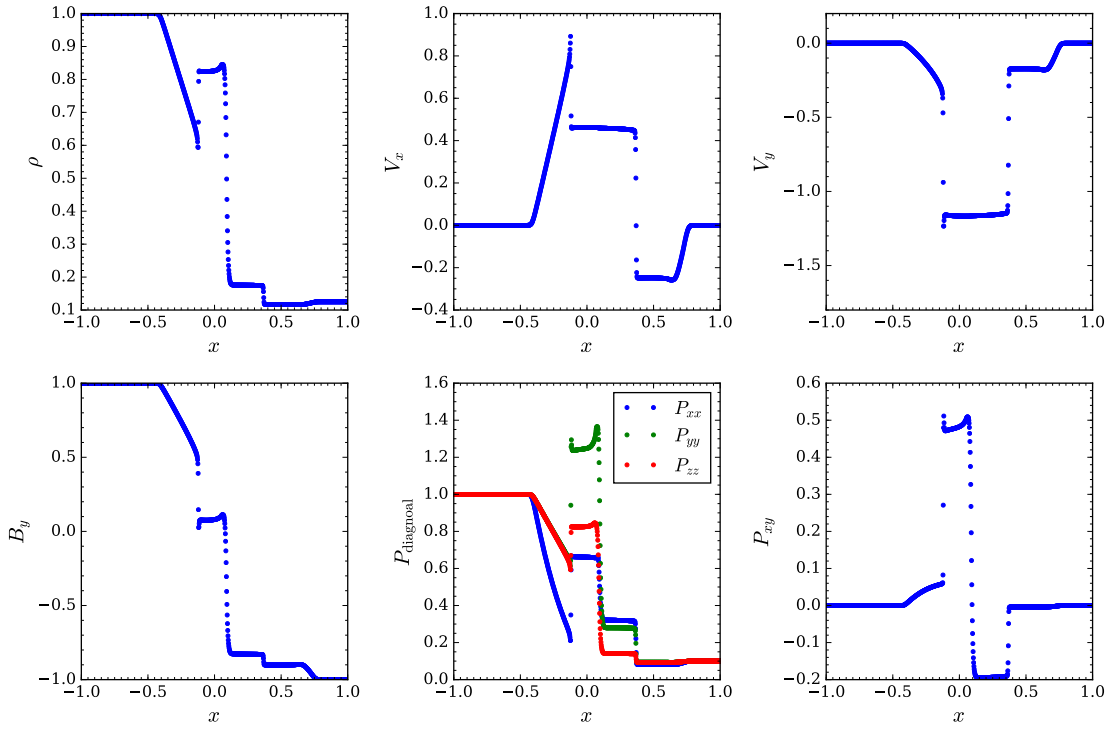

Figure 3.3: Brio-Wu shock tube problem with no gyrotropization. The data have been taken at $t = 0.2$.

lobe magnetic field and the x-axis, and L is the half width of the current sheet. The initially isotropic pressure balance is determined so as to set the plasma beta, $\beta = 2P/B^2$, measured in the lobe region, to 0.25. Once the normal magnetic field, B_x, is superimposed, fast rarefaction waves, rotational discontinuities, and slow shocks propagate away from the current sheet toward both lobes. The magnitude of B_x is adopted as 5% of B_0. The simulation domain, $-200L \leq x \leq 200L$, is discretized by 2000 grid points, and the free boundary conditions are assumed to be located at $|x| = 200L$. For normalization, we set L, B_0, and the lobe density, ρ_0, to unity, which implies that the velocity and pressure are normalized by $V_A = B_0/\sqrt{\rho_0}$ and B_0^2, respectively.

3.4.3.1 Fast isotropization

First, Fig. 3.4 shows snapshots for fast isotropization at $t = 3500$, prior to which a pair of fast rarefaction waves propagated away from the simulation domain. The angle ϕ is set at 30°. Note that this figure is comparable to the left-hand panels of Fig. 1 in HH13. From the panel showing the profiles of the magnetic field, we can see that a pair of rotational discontinuities around $|x| \sim 110$ rotate the entire magnetic field in the z direction. Then,

slow shocks at $|x| \sim 75$, which we can observe in all panels, dissipate the field energy contained in B_z. This behavior is common to the standard MHD approach, independent of the initial angle ϕ, and our model properly and qualitatively retains the same structure as in the isotropic MHD case, even with the inclusion of the propagation of shearing Alfvén waves.

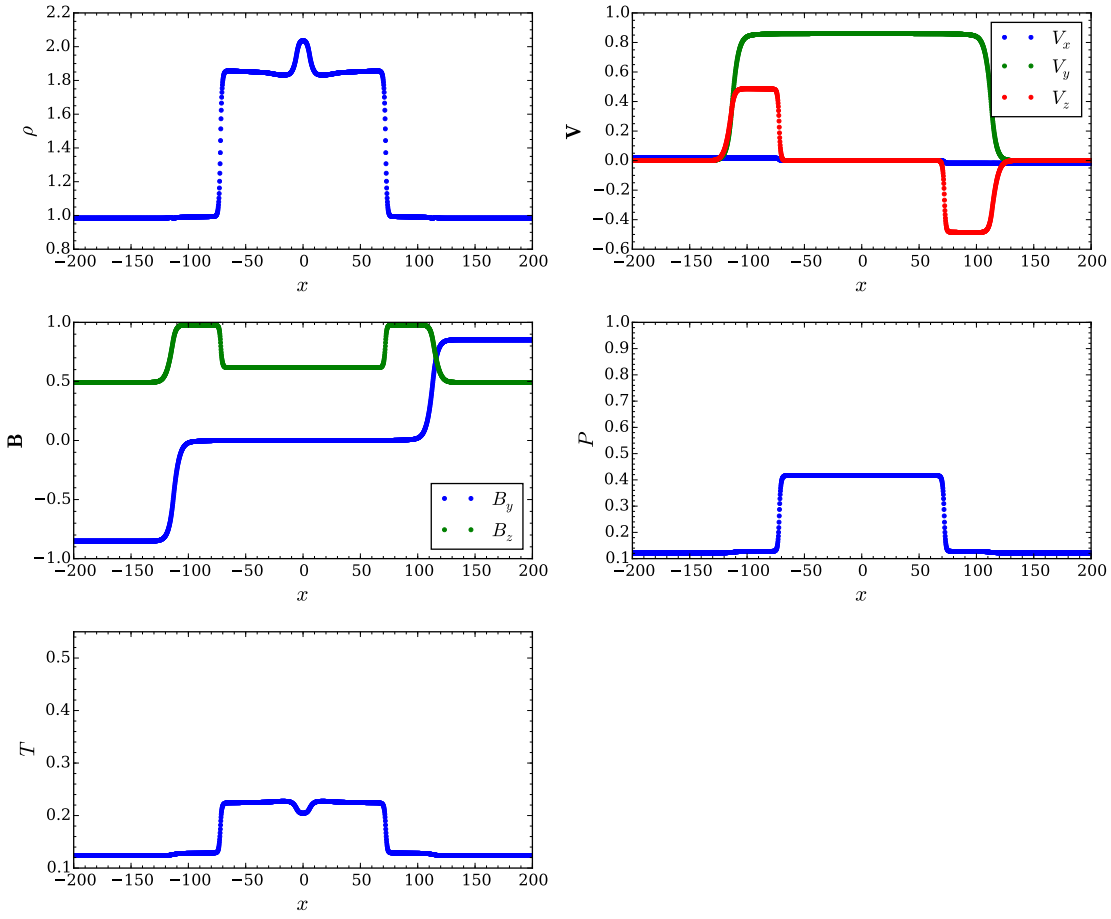

Figure 3.4: Results of a one-dimensional Riemann problem set up to imitate a self-similar reconnection layer, assuming fast isotropization. The data have been taken at $t = 3500$

3.4.3.2 Fast gyrotropization

Fig. 3.5, on the other hand, shows the same plots, except that only gyrotropization is assumed. Since a uniform and constant normal magnetic field is imposed in this one-dimensional problem, each grid point always has a finite magnetic-field strength, which leads to almost the same result as in the double adiabatic limit. Fig. 3.5 is, therefore, now comparable to the right-hand panels of Fig. 1 in HH13, and again all profiles quantitatively agree well with each other. In particular, the reversal of the propagation speeds of slow-

mode waves ($|x| \sim 150$) and Alfvén waves ($|x| \sim 90$), the weakness of the slow shocks in terms of the released magnetic energy, and the parallel pressure enhancements across the slow shocks are captured correctly. As already discussed in the previous subsection, in addition, the contact discontinuity remaining around $x \sim 0$ can sustain variations in the magnetic field and the pressure anisotropy in contrast to the flat profiles in Fig. 3.4.

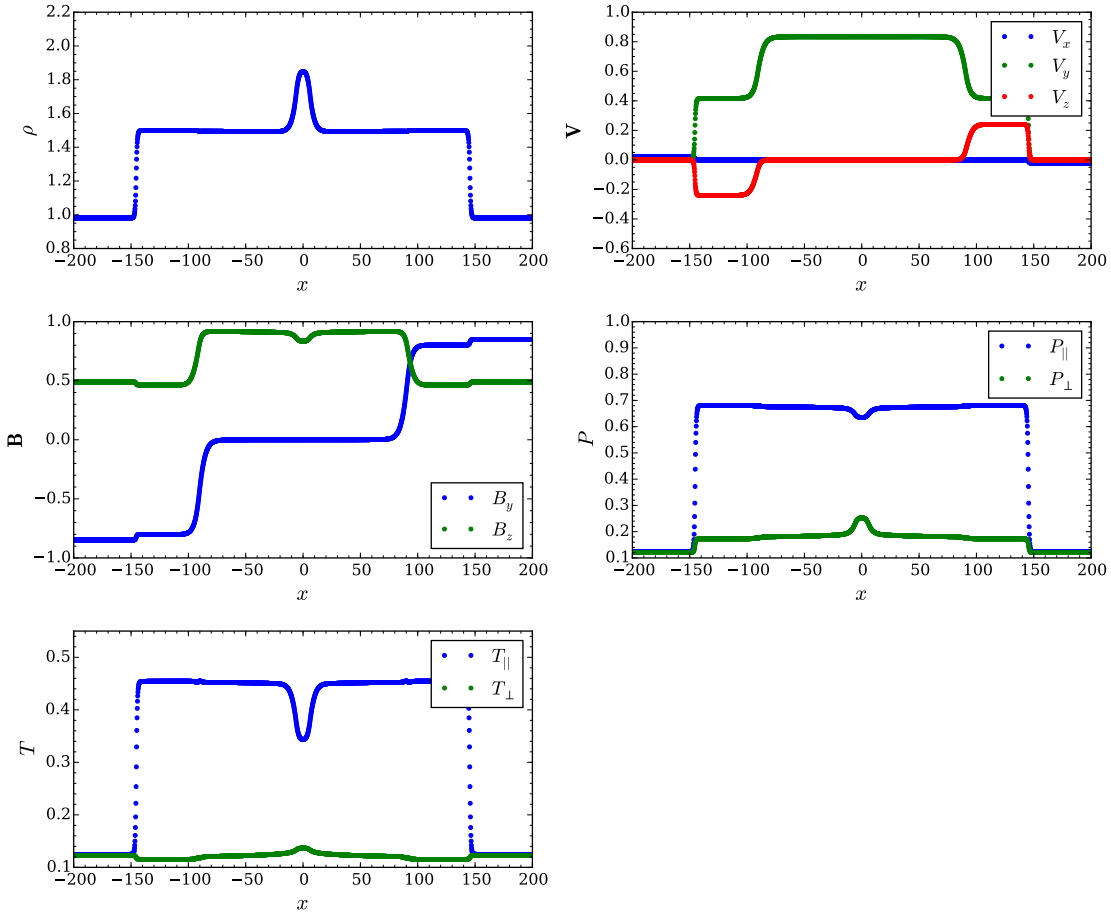

Figure 3.5: Results of a one-dimensional Riemann problem set up to imitate a self-similar reconnection layer, assuming fast gyrotropization. The data have been taken at $t = 3500$.

3.4.3.3 Without gyrotropization

It is remarkable that if any gyrotropization and isotropization effects are neglected, the present model does not show any evidence of magnetic reconnection accompanied by a release of magnetically stored energy, as demonstrated in Fig. 3.6. The final state, in this

case, is simply a dynamical equilibrium sustained by a contact discontinuity satisfying

$$\left[\rho V_x^2 + P_{xx} + \frac{B^2}{2}\right]_2^1 = 0, \tag{3.52}$$

$$[\rho V_x V_y + P_{xy} - B_x B_y]_2^1 = 0, \tag{3.53}$$

$$[\rho V_x V_z + P_{zx} - B_x B_z]_2^1 = 0, \tag{3.54}$$

where the leftmost term in each equation vanishes, because V_x is zero across the contact discontinuity. Focusing on the y direction, for example, the initial state is dynamically imbalanced by the magnetic tension force, $-B_x B_y$, owing to the presence of an additionally imposed B_x component. The present assumption adds five additional degrees of freedom, making this system characterized by a total of six independent entropy modes: i.e.,

$$\begin{aligned}(\delta\rho,\ \delta\mathbf{V},\ \delta B_y,\ \delta B_z,\ \delta P_{xx},\ \delta P_{yy},\ \delta P_{zz},\ \delta P_{xy},\ \delta P_{yz},\ \delta P_{zx}) \\ = \begin{cases} (1,\ \mathbf{0},\ 0,\ 0,\ 0,\ 0,\ 0,\ 0,\ 0,\ 0), \\ (0,\ \mathbf{0},\ 0,\ 0,\ 0,\ 1,\ 0,\ 0,\ 0,\ 0), \\ (0,\ \mathbf{0},\ 0,\ 0,\ 0,\ 0,\ 1,\ 0,\ 0,\ 0), \\ (0,\ \mathbf{0},\ 0,\ 0,\ 0,\ 0,\ 0,\ 0,\ 1,\ 0), \\ (0,\ \mathbf{0},\ 1,\ 0,\ -B_y,\ 0,\ 0,\ B_x,\ 0,\ 0), \\ (0,\ \mathbf{0},\ 0,\ 1,\ -B_z,\ 0,\ 0,\ 0,\ 0,\ B_x), \end{cases}\end{aligned} \tag{3.55}$$

which can be obtained easily by picking up non-propagating eigenmodes from the linearized equations in the present system. Then, the P_{xy} profile induced by the preceding waves can soon regain dynamical balance (3.53) by means of the P_{xy}-related entropy wave—the fifth mode in equation (3.55).

Once the redistribution of the thermal pressure is enforced through gyrotropization and/or isotropization, however, an imbalance develops. In the isotropic limit, in particular, the imbalance for $-B_x B_y$ can be resolved only through $V_x V_y$, because $P_{xy} = 0$. The induced V_x drives the reconnection process, as we have seen already. Whether or not the reconnection is actually quenched for certain initial parameters cannot be predicted until the Riemann problem has been solved.

At a much earlier stage, on the other hand, we can recognize the propagation of slow- and Alfvén-related waves, as well as of fast rarefaction waves. Fig. 3.7 shows a snapshot taken at $t = 100$ using the same format as in Fig. 3.6. The vertical dashed lines indicate the positions of different waves predicted from the parameters pertaining to the right-hand

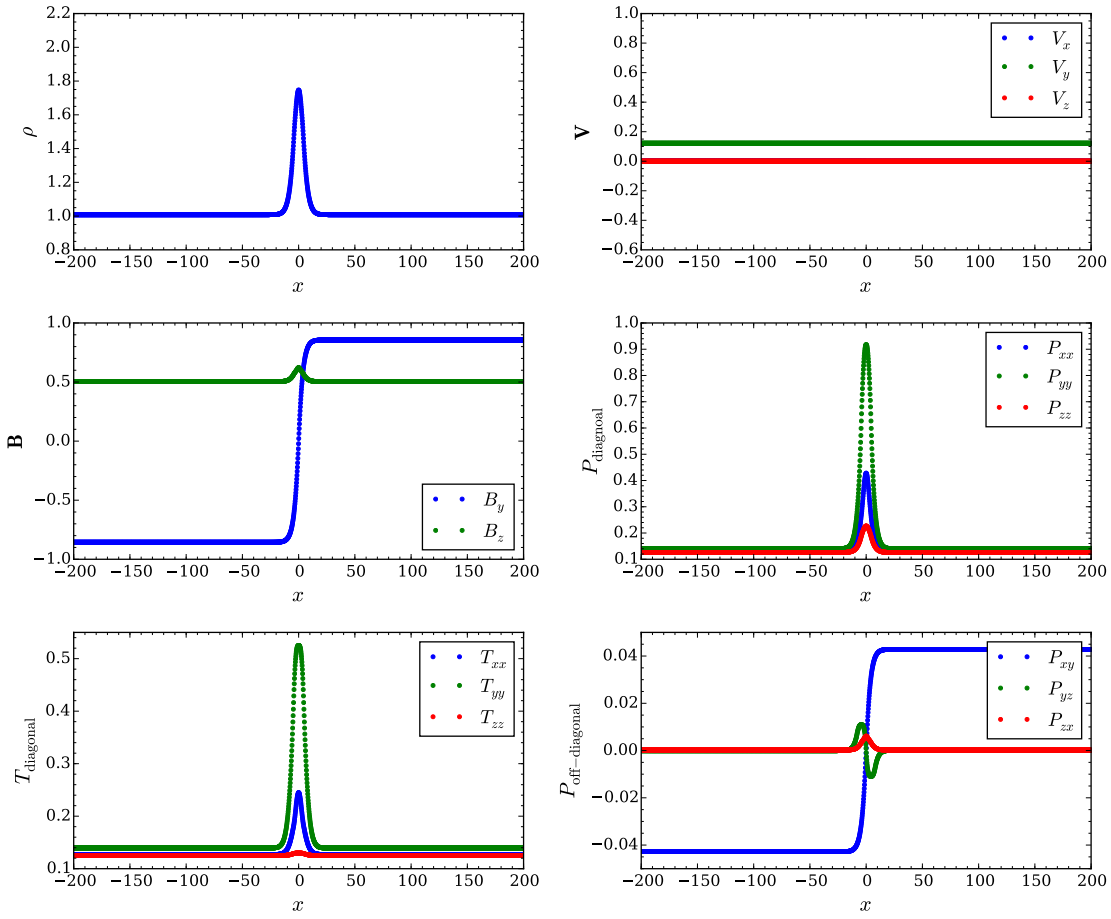

Figure 3.6: Results for a one-dimensional Riemann problem at $t = 3500$, without inclusion of gyrotropization or isotropization effects.

upstream regions. Note that the speeds of the slow and Alfvén waves are much faster than those in the gyrotropic cases. In the absence of gyration, the counterpart of the Alfvén wave is no longer completely decoupled from the thermal pressure in the propagation direction. In this case, the phase velocity of Alfvén-like waves becomes

$$V_A = \sqrt{\frac{P_{xx} + B_x^2}{\rho}}, \tag{3.56}$$

which can be obtained as an intermediate eigenvalue of the Jacobian matrix, $(\partial \mathbf{F}/\partial \mathbf{U}) + \mathbf{A}$, as discussed in section 3.3.1. This velocity is much larger than the usual Alfvén speed measured in the present configuration. The slow mode also becomes faster than its gyrotropic counterpart because of the reduction of the number of degrees of freedom related to the internal energy through the absence of directional coupling of the pressure tensor. This leads to an increase in the effective adiabatic index and also in the sound

speed. The phase speeds of both waves tend to become very close, and the resulting profiles exhibit a compound structure. Nevertheless, our result shows that these waves induce only small variations, and the downstream quantities remain in almost the same state as the initial current sheet, supported by the additional entropy waves.

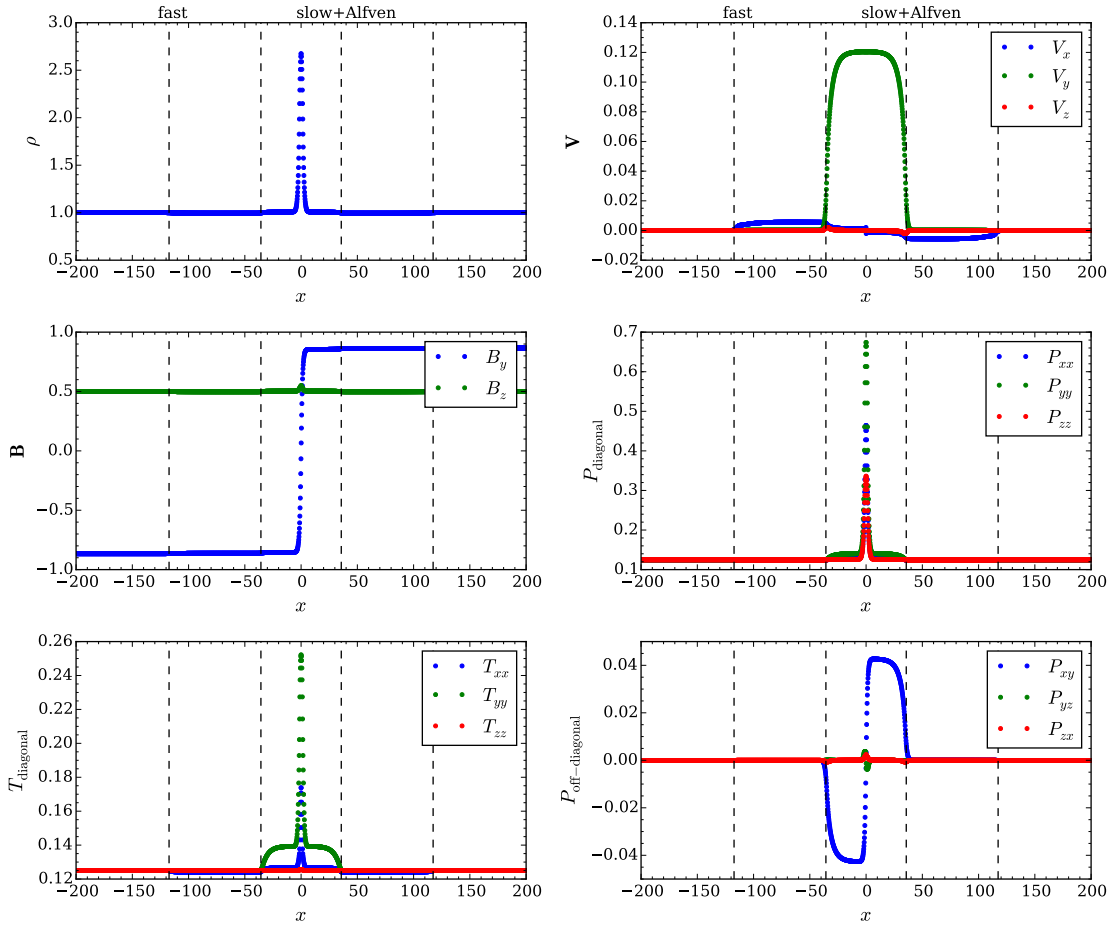

Figure 3.7: Results of the one-dimensional Riemann problem at $t = 100$, without inclusion of gyrotropization or isotropization effects.

The present problem is particularly designed for one of the numerical tests to extract the effect solely associated with the anisotropic pressure. For detailed analysis and a comparison with kinetic simulations or observations, one may need to consider including the Hall effect, pitch-angle scattering, and the finite Larmor radius effect, among other options (Galeev & Zelenyĭ, 1976; Del Sarto et al., 2011; Liu et al., 2012).

3.4.4 Field loop advection

The field-loop advection problem was originally designed to test multidimensional MHD codes (Gardiner & Stone, 2005). This problem contains a spacious, magnetically neutral

region, making it suitable for investigating the capability to deal with anisotropic pressure even in unmagnetized regions, which is one of the critical advantages of the present model.

In this problem, a weakly magnetized field loop is advected obliquely across the simulation domain $(x, y) \in [-L, L] \times [-L/2, L/2]$ with a velocity

$$\mathbf{V} = (V_0, 2V_0, 0)\,, \tag{3.57}$$

which indicates that the field loop returns to the initial position after a time interval $t = 2(L/V_0)$. The magnetic field loop is given in the form of a vector potential as

$$A_z\,(x, y) = \begin{cases} B_0\,(R - r) & (r \le R) \\ 0 & (\text{otherwise}) \end{cases}\,, \tag{3.58}$$

where $r = \sqrt{x^2 + y^2}$ is the distance from the origin, $R = 0.3L$ is the radius of the field loop, and B_0 is the magnetic field strength inside the loop. The magnetic field is initialized by taking a finite difference of the vector potential; otherwise a considerable error in $\nabla \cdot B$ will seriously affect the results. The gas pressure is assumed to be isotropic and spatially uniform with $\beta = 2 \times 10^6$ inside the field loop. The density is also distributed uniformly, satisfying $P/\rho = V_0^2$. We adopt the normalization where L, V_0, and B_0 are unity. The computational domain is discretized with 400×200 grid points. The effective collision frequency for gyrotropization is now set to be close to the dynamical timescale by assuming $\nu_g = 10\,|\mathbf{B}|\,/B_0$.

The simulation result at the time when the field loop returns to the initial position is shown in Fig.3.8. The four panels show (a) the magnetic pressure, (b) the magnetic field lines, (c) the deviation of the diagonally-averaged pressure from the uniform initial value, and (d) the in-plane, off-diagonal component of the pressure. All quantities are normalized by the initial magnetic pressure inside the field loop, $B_0^2/2$. Fig.3.8(a) is comparable to the top left-hand panel in Fig.3 in Gardiner & Stone (2005), and both figures agrees well with each other. From the top two panels, (a) and (b), which are related to the magnetic field, any spurious effects cannot be observed either inside the loop, where inadequate treatment of the electric field would result in a certain pattern, and in the vicinity of the edge of the loop, where the magnetic field changes discontinuously. Therefore, we conclude that introduction of the pressure tensor does not induces any numerical difficulties in our extension to multidimensional problems.

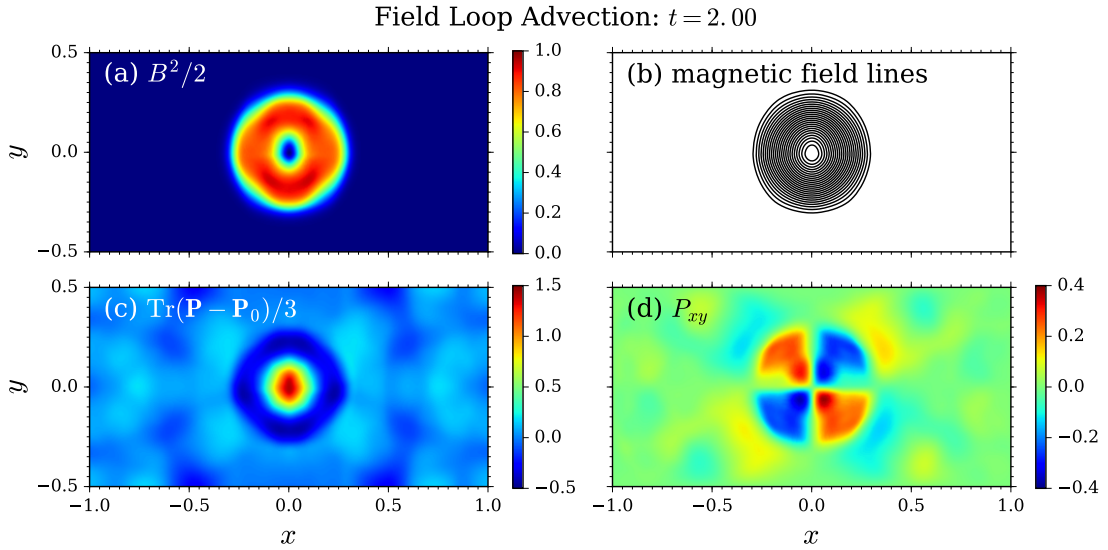

Figure 3.8: Snapshot at $t = 2$ for the field-loop advection problem. All variables are normalized by the initial magnetic pressure inside the field loop, $B_0^2/2$. Relatively slow gyrotropization is assumed with $\nu_g = 10\,|B|\,/B_0$.

The bottom two panels, (c) and (d), are related to the pressure tensor. Although the diagonally-averaged pressure, $\mathrm{Tr}\mathbf{P}/3$, is maintained isotropic, a finite off-diagonal component, P_{xy}, induces a quadrupole pattern because of the difference between $P_{||}$ and $P_{\perp}$ inside the loop. Because the xy component is given by $P_{xy} = (P_{||} - P_{\perp})\hat{b}_x\hat{b}_y$ under the assumption of gyrotropic pressure, this pattern indicates the presence of a *firehose*-type anisotropy with $P_{||} > P_{\perp}$, as deduced by considering the direction of the magnetic field. Qualitatively speaking, this anisotropy can also be understood by considering the behavior associated with the double adiabatic approximation, because the decomposition of the pressure tensor into parallel and perpendicular components is allowed inside the magnetic-field loop. The intuitive form of the double adiabatic equations of state can be formulated as follows,

$$\frac{D}{Dt}\left(\frac{P_{\perp}}{\rho B}\right) = 0, \tag{3.59}$$

$$\frac{D}{Dt}\left(\frac{B^2 P_{||}}{\rho^3}\right) = 0, \tag{3.60}$$

where $D/Dt = \partial/\partial t + \mathbf{V}\cdot\nabla$ indicates a Lagrangian derivative. Equations (3.59) and (3.60) indicate that a decrease in the magnetic-field strength naturally leads to an enhancement of the parallel pressure. In the present case, the magnetic field changes almost discontinuously across the outer edge of the field loop and also across the loop's center, which

results in a decrease of magnetic-field strength through significant numerical dissipation.

Finally, we emphasize that the present model can successfully solve the equations for the vast unmagnetized regions in this problem without any numerical difficulties. The boundaries between the magnetized and unmagnetized regions are also captured seamlessly. Note that, except for the early stages, each cell might contain a non-zero magnetic field below or around the level of the machine precision. Nevertheless, it may no longer be meaningful to define $P_{||}$ and $P_{\perp}$ there, and we strongly recommend the direct use of the non-gyrotropic pressure tensor in essentially neutral regions.

3.4.5 Magnetorotational instability

The previous tests involved only weak anisotropy so that the resultant situations were stable with respect to anisotropy-driven instabilities (i.e., firehose and mirror instabilities). If one of these instabilities were to turn on, a rapidly growing eigenmode would lead to the simulation crashing. This happens, because the growth rate becomes larger without bounds as the wavelength becomes shorter. The maximum growth rate of the kinetic counterpart of the MHD instability, on the other hand, will be limited by the finite Larmor radius effect. A compromise to avoid the disruption was presented by Sharma et al. (2006) (hereafter SHQS06). They limited the maximum degree of the pressure anisotropy by assuming that, once the anisotropy exceeds the threshold of one of the kinetic instabilities, the wave instantaneously reduces the anisotropy to the marginal state through pitch-angle scattering (hard-wall limit). This model is applied to their simulations of magnetorotational instabilities (MRI) in a collisionless accretion disk based on the gyrotropic formulation and the Landau fluid model, and it succeeds in tracking the non-linear evolution of the MRIs. In this subsection, we follow their pitch-angle scattering model and show the result of the MRI simulation as a test problem for highly non-linear evolution of an anisotropic plasma.

While the same thresholds—see Eqs (32)–(34) in SHQS06—are employed in the present test, we slightly modified the numerical procedure of the scattering model compared with the implementation of SHQS06, where the collision terms in the equations of state, $\left[\partial P_{||}/\partial t\right]_c = -\left(2\nu/3\right)\left(P_{||} - P_{\perp}\right)$ and $\left[\partial P_{\perp}/\partial t\right]_c = -\left(\nu/3\right)\left(P_{\perp} - P_{||}\right)$, were solved implicitly. Instead of the implicit treatment, we use an analytic approach. Once the parallel and perpendicular pressures in a marginal state, $P_{||,s}$ and $P_{\perp,s}$, have been determined, the

analytic solution for the isotropized pressure tensor can also be obtained by solving

$$\left[\frac{\partial \mathbf{P}}{\partial t}\right]_c = -\nu_{\rm iso}\left(\mathbf{P} - \mathbf{P}_s\right), \tag{3.61}$$

where $\nu_{\rm iso}$ is the effective collision frequency of the pitch-angle scattering, which should be set to a much larger value than any dynamical frequencies of the system, and $\mathbf{P}_s$ is the marginal pressure tensor. For detailed calculation of the marginal state, see Appendix B.

The other setup of our simulation is the same as that in SHQS06. With the help of the shearing box model (Hawley et al., 1995; Stone & Gardiner, 2010), the radial, azimuthal, and vertical coordinates in a cylindrical system are converted to x, y, and z in a local Cartesian coordinate system, respectively, and the simulation domain is fixed to $(x, y, z) \in [-L/2, L/2] \times [0, 2\pi L] \times [0, L]$. At the edges, the so-called shearing periodic boundary conditions are employed. A differentially rotating plasma is then described by the shear velocity $\mathbf{V}_0 = (0, -q\Omega_0 x, 0)$, where Ω_0 is the angular velocity of a disk at the center of the simulation box, and the dimensionless parameter $q = -\ln\Omega/\ln R$ is set at 1.5. We assume that a plasma characterized by a uniform and isotropic pressure, $\mathbf{P} = P_0\mathbf{I}$, is initially threaded by a weak vertical magnetic field with $\beta = 400$. The initial mass density, ρ_0, is also uniform. To trigger the growth of the MRIs, we add a random velocity perturbation with a magnitude of 0.1% of the isothermal sound speed, $c_s = \sqrt{P_0/\rho_0}$, which is equated to ΩL by assumption of a geometrically thin disk. In this problem, we employ the 5th-order WENO scheme and the 3rd-order TVD Runge-Kutta scheme rather than 2nd-order methods for the purpose of resolving MRI-driven turbulence more accurately. The number of grid points is set at $64 \times 128 \times 64$.

The time evolution of the volume-averaged energy density and the xy component of the stress tensor, normalized by P_0, are shown in the top and bottom panels of Fig. 3.9, respectively. The results under the isotropic MHD limit are plotted in the two left-hand panels for comparison purposes. They show common behavior of the MRIs in unstratified shearing box simulations. During the early stages, all unstable modes start to grow exponentially. After the fastest growing mode captured in the simulation box, which has a wavelength of $\lambda = L/2$, becomes dominant, the non-linear growth of the longest-wavelength mode, $\lambda = L$, soon forms a pair of in- and outward channel flows. The amplitude of this channel-flow structure continues to increase, because it is an exact solution of the shearing box system (Goodman & Xu, 1994). At roughly three orbits, the channel solution drastically

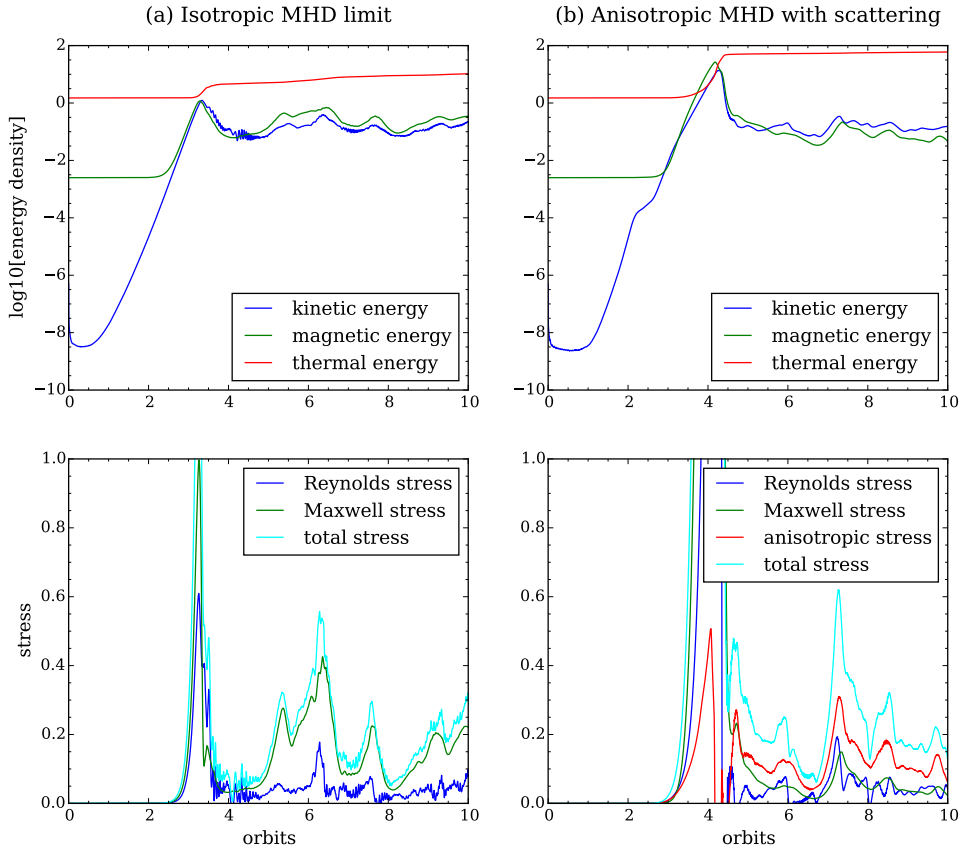

Figure 3.9: Volume-averaged energy density and stress, normalized by the initial thermal pressure, as functions of time. The two left-hand panels (a) show the results for an isotropic MHD limit, while the right-hand panels (b) show the results for anisotropic MHD models with pitch-angle scattering.

breaks down into a turbulent state because of magnetic reconnection across the dense current sheet. During the subsequent saturated stage, the MHD turbulence continues to fill the simulation domain while repeating the formation of local channel flows and their breakdowns through reconnection. The kinetic energy contained in motion deviated from a Keplerian orbit and the magnetic energy are in equi-partition during this phase. The stress, however, is highly dominated by magnetic contributions, also known as Maxwell stress. This large stress caused by MHD turbulence is considered to play an important role for angular-momentum transport in accretion disks. Note that the thermal energy continues to increase gradually, because the energy input into the simulation domain through the boundary condition finally dissipates to thermal energy, and no cooling mechanism is included in the system.

The anisotropic MHD calculation incorporated with the pitch-angle scattering model, on the other hand, leads to the two right-hand plots in Fig. 3.9. There are two noticeable differences from the isotropic case in the energy history. One is a dent of the kinetic energy around two orbits. As described by SHQS06, this happens because the *mirror*-type pressure anisotropy with $P_\perp > P_{||}$ generated by the growth of the MRI suppresses further growth of the MRI itself. If the scattering model is not included, the MRI stops at this level, and subsequently the simulation box will be filled with vertically propagating Alfvén waves.

The other major difference is the excessive peak of magnetic energy around four orbits, just before the channel flow breaks down because of magnetic reconnection. This feature was also pointed out by SHQS06 but not discussed in detail. To understand this issue, it is useful to consider the effect of the pressure anisotropy on the dynamics of the magnetic reconnection, as suggested in Hoshino (2015). The author demonstrated the enhancement of angular-momentum transport in collisionless accretion disks by means of PIC simulations from the perspective just discussed. He states that, although the *mirror*-type anisotropy with $P_\perp > P_{||}$ induced by the MRI is favorable for reconnection, or tearing instabilities, to grow (Chen & Palmadesso, 1984), the opposite *firehose*-type anisotropy with $P_{||} > P_\perp$ occurring in a dense current sheet as a result of reconnection will suppress further reconnection. The spatial distribution of the mass density and pressure anisotropy observed in our calculations during the epoch of the largest channel flow, $\Omega t/2\pi = 4.2$, are shown in Fig. 3.10. The rightmost panel, which displays the occurrence frequency as a function of ρ and $P_\perp/P_{||}$, clearly shows that the inside of the dense current sheet is dominated by relatively isotropic or *firehose*-type anisotropic plasma compared with the dilute lobe regions, which is consistent with the ideas discussed above. It is, however, not an obvious issue as to whether or not the suppression or enhancement of the tearing instability in an anisotropic current sheet are captured in the present fluid model, either qualitatively or quantitatively. Further discussion of this issue is beyond the scope, and will be the subject of future work.

3.5 Discussion and summary

In this chapter, we have proposed a natural extension to the double adiabatic approximation, or simply the CGL limit, to deal with the effects of an anisotropic pressure tensor

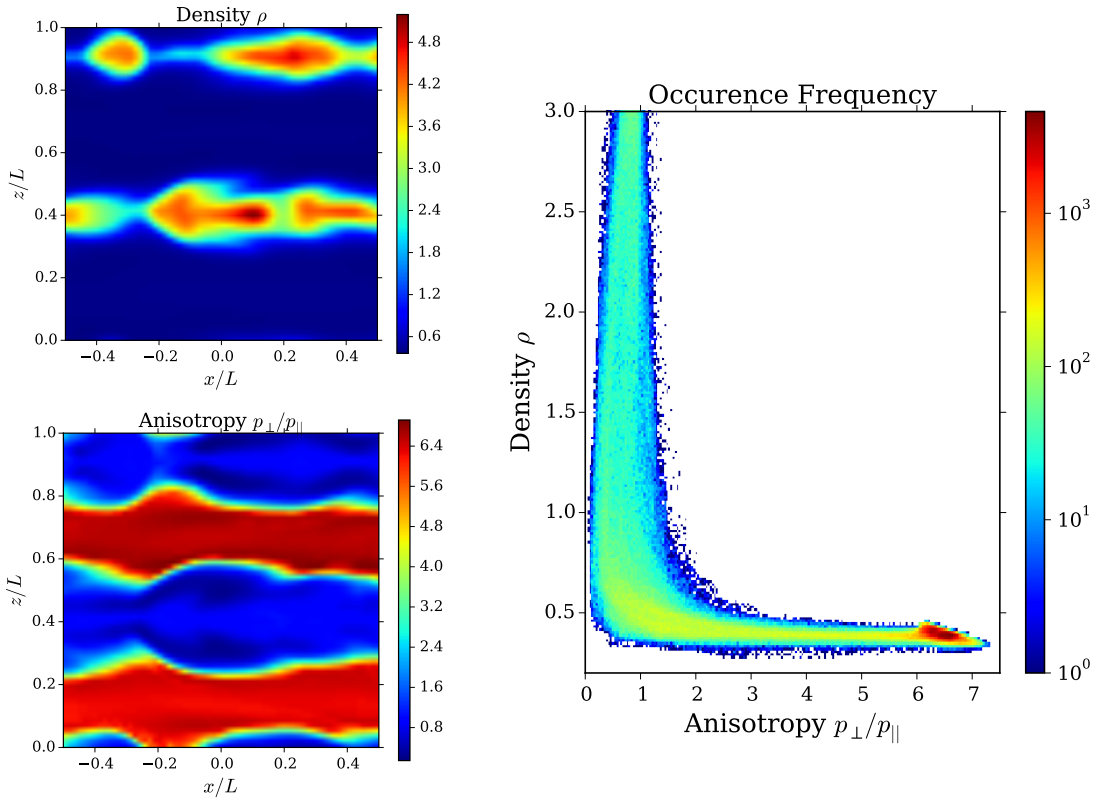

Figure 3.10: Slices of the density and pressure anisotropy distributions along $y = 0$ at time $\Omega t/2\pi = 4.2$, just before the largest channel flow structure breaks down. The rightmost panel shows the occurrence frequency as a function of the density and the anisotropy, which demonstrates that the dense current sheet consists of a relatively isotropic plasma or a slightly anisotropic plasma with $P_{||} > P_\perp$.

in the framework of magnetohydrodynamics. The features of our fluid model can be summarized as follows:

1. All six components of the pressure tensor are evolved according to equation (3.2), which is the 2nd-moment equation of the Vlasov equation without assuming isotropy or gyrotropy.

2. The effect of gyrotropization is introduced through an effective collision term, with the collision rate set proportional to the local magnetic-field strength, which is a natural assumption from the physical insights into the last term of equation (3.2).

3. With the help of features 1. and 2., the present model successfully eliminates the singularity at magnetic null points, where the CGL equations cannot be applied.

4. By employing a large gyrotropization rate or a large isotropization rate, our model

correctly reduces to the CGL limit (when a finite magnetic field is present) or to standard MHD, respectively, in an asymptotic manner.

The present model contains one free parameter, ν_g, which controls the speed of gyrotropization. This timescale is, in general, considered to be much shorter than the dynamical time of a given system. In (almost) unmagnetized regions, however, such an ordering fails because of the lack of any cyclotron motion or owing to a rather large gyro period and, hence, a singularity in the mathematical expression appears inevitably. Our fluid model represents one of the main efforts to recover regularity by adequately adopting a functional form of ν_g that is consistent with the physical consideration of the $\Omega_c \mathbf{P} \times \hat{\mathbf{b}}$ term in the 2nd-moment equation.

We also emphasize that it is a relatively easy task to extend an existing MHD code written in a conservative form to the present model, because we derive the basic equations as clear counterparts to the standard MHD equations. However, one should keep in mind that the effect of the directional energy exchange by the Lorentz force cannot be included into the conservative term. This requires an appropriate treatment for a Riemann solver, as discussed in section 3.3; otherwise the calculation will fail to return a physically and mathematically consistent solution.

The prospective applications of the present formulation include a wide variety of large-scale phenomena in collisionless plasmas, particularly where the effect of anisotropic pressure plays an important role. The magnetospheric plasma environment around Earth is a typical example, where the mean free path of charged particles and the typical spatial scale differ by roughly three orders of magnitude. Large temperature anisotropy has been measured by satellite observations, particularly near current sheets accompanied by magnetic reconnection (e.g., Hoshino et al., 1997; Artemyev et al., 2015; Hietala et al., 2015). These magnetically neutral sites can also be solved seamlessly without any numerical and theoretical difficulties by this model.

Finally, focusing on the method to handle a pressure tensor, we neglect the 3rd- and higher-order moments of the Vlasov equation, such as the heat fluxes. Establishment of a more sophisticated fluid model that can track other kinetic aspects is very challenging in the field of collisionless plasma physics. The model proposed here may shed light on this issue as a basis and as a guiding idea.

Chapter 4

Stratified Simulations of Collisionless Accretion Disks

4.1 Introduction

To explain efficient angular momentum transport required for mass accretion in accretion disks is one of the fundamental issues in astrophysics. As already reviewed in chapter 1, since the astrophysical importance of the magnetorotational instability (MRI) was pointed out (Balbus & Hawley, 1991), the MRI has been investigated elaborately as a driver of strong magnetohydrodynamic (MHD) turbulence to provide substantial turbulent transport of angular momentum. While numerical studies of MRIs developed under the MHD framework, where collisional state is assumed, has achieved success, it is also of great importance to understand dynamics in collisionless regime. For instance, Sagittarius A* (Sgr A*), which is a compact radio source at the center of our galaxy, is believed to be combination of a collisionless accretion disk and a relativistic jet possessing a supermassive black hole at the center (e.g., Narayan et al., 1995; Falcke & Markoff, 2000; Doeleman et al., 2008; Kusunose & Takahara, 2012).

Given this fact, Hoshino (2015) conducted a three-dimensional, local shearing box simulation in collisionless regime using particle-in-cell (PIC) technique. He pointed out that the angular momentum transport carried by anisotropy in velocity distribution function, which is interpreted as an anisotropic pressure tensor in fluid-based models, reached a value comparable to that carried by Maxwell stress, $-B_x B_y/4\pi$. It was also argued that the total transport efficiency measured by instantaneous thermal pressure was enhanced by an order of magnitude compared with standard MHD results. In terms of α-viscosity

proposed in Shakura & Sunyaev (1973), which is defined as the xy-component of the stress tensor normalized by the thermal pressure, $\alpha \sim \mathcal{O}(0.1)$ was achieved.

Sharma et al. (2006), on the other hand, investigated the effect of the anisotropic stress under the fluid framework based on combination of the double adiabatic approximation, or Chew-Goldberger-Low (CGL) model after Chew et al. (1956), and Landau fluid model (Hammett & Perkins, 1990). The CGL model assumes a gyrotropic pressure. It means that a pressure tensor can be described by only two independent components parallel and perpendicular to a local magnetic field, rather than one scalar value. These two variables are evolved with time in association with MHD-type equations, while other kinetic effects are neglected. The CGL results agreed with the more lately published PIC calculation in the sense that the anisotropic and Maxwell stresses had the same contribution to the angular momentum transport. A puzzling difference between these two approaches is, however, the total efficiency of the transport. Although the PIC simulation predicts a quite large value of α, the local simulations using the CGL model lead to values similar to those obtained in standard MHD calculations.

One of the possible keypoints to solve this discrepancy may be a treatment of magnetic reconnection under anisotropic pressure. In both fully-kinetic and fluid-based approaches, the perpendicular pressure, $p_\perp$, tends to dominate the parallel pressure, $p_{||}$, in shearing box simulations. This is qualitatively because the MRI is a process to enhance the magnetic field, which naturally results in anisotropy with $p_\perp > p_{||}$ from conservation of the first and the second adiabatic invariants. In contrast, magnetic reconnection dissipates the magnetic energy and makes opposite anisotropy in neutral sheets where reconnection takes place. According to Hoshino (2015), it is this parallel pressure enhancement via reconnection that suppresses successive reconnection itself (Chen & Palmadesso, 1984). As a result, larger magnetic energy, and hence larger Maxwell stress, are likely to be maintained in the system. It is, however, still ambiguous whether and how much the effect of suppression of reconnection by the pressure anisotropy is retained in the CGL framework. A part of this ambiguity arises from the fact that CGL-based models cannot deal with pressure anisotropy at magnetically neutral regions in its own right, due to the presence of singularity near $B = 0$. To take a step forward beyond previous fluid models with anisotropy, in this chapter, we adopt a newly invented model which has already been explained in detail in chapter 3. Our new model enables us to define and resolve an anisotropic pressure tensor both in magnetized and unmagnetized regions seamlessly

without any peculiar treatment. Thus we can investigate the role of the pressure tensor at the deep inside of neutral sheets.

In spite of limited kinetic effects included in the system, it is of significance to employ a fluid-based model possessing the scale-free property, when large-scale dynamics is considered. Since the fully kinetic approach must resolve particle scales such as Debye lengths and gyro radii, it is quite unrealistic to analyze disk-scale behavior, which in general occurs in a scale much larger than the kinetic scales. In this sense, this work can be placed in one of the attempts to fill the gap between the small-scale, kinetic approach and the scale-free, fluid approach. In particular, we tackle a series of *stratified* shearing box simulations by retaining vertical gravity of a central object. The stratification introduces a concept of the disk's scaleheight, or the disk thickness, into the system, which cannot be reproduced in PIC simulations apparently.

The differences between stratified and unstratified shearing box simulations have been discussed by a number of authors, based on the standard MHD framework in collisional regime (e.g., Brandenburg et al., 1995; Stone et al., 1996; Miller & Stone, 2000; Davis et al., 2010). One of the major changes is generation of buoyantly rising patches of strong toroidal magnetic fields, even when the simulation domain does not contain any external magnetic flux. The previous studies have suggested that these magnetic patches work just like a global or an external field for local MRIs, which can sustain strong MRI-driven turbulence and enhance the angular momentum transport by roughly one order of magnitude in terms of α compared with an unstratified simulation started from the same initial condition. It is still unclear what makes these patches. Nevertheless, investigating this effect in the collisionless regime as well would be of importance to understand global behavior of collisionless accretion disks. In this chapter, we *revisit* this point for the first time in the collisionless framework.

This chapter is organized as follows. In section 4.2, we describe numerical settings. In particular, procedures specific to the present problem are explained in detail. Section 4.3 discusses our simulation results while comparing with cases under isotropic pressure calculated using the same code. Finally, section 4.4 is devoted to summary and concluding remarks.

4.2 Simulation setup

4.2.1 Basic equations

In all calculations presented in this chapter, we employ the local shearing box approximation (Hawley et al., 1995) along with the vertical component of gravity. The pressure anisotropy is handled with the model described in chapter 3, while the shearing source terms and Coriolis force are additionally included. Then the basic equations are as follows:

$$\frac{\partial \rho}{\partial t} + \nabla \cdot (\rho \mathbf{v}) = 0, \tag{4.1}$$

$$\frac{\partial \rho \mathbf{v}}{\partial t} + \nabla \cdot \left[\rho \mathbf{v}\mathbf{v} + \mathbf{p} + \frac{B^2}{2}\mathbf{I} - \mathbf{B}\mathbf{B} \right] = -2\rho \mathbf{\Omega} \times \mathbf{v} - \rho \nabla \Phi, \tag{4.2}$$

$$\frac{\partial \mathbf{B}}{\partial t} - \nabla \times (\mathbf{v} \times \mathbf{B}) = 0, \tag{4.3}$$

$$\begin{aligned} &\partial_t \left(\rho v_i v_j + p_{ij} + B_i B_j \right) + \partial_k \left(\rho v_i v_j v_k + p_{ij} v_k + p_{ik} v_j + p_{jk} v_i + \mathcal{S}_{kij} + \mathcal{S}_{kji} \right) \\ &= B_i v_k \partial_k B_j + B_j v_k \partial_k B_i - B_k v_i \partial_j B_k - B_k v_j \partial_i B_k \\ &-2\rho v_i \varepsilon_{jkl} \Omega_k v_l - 2\rho v_j \varepsilon_{ikl} \Omega_k v_l - \rho v_i \partial_j \Phi - \rho v_j \partial_i \Phi - \nu_g \left(p_{ij} - p_{g,ij} \right), \end{aligned} \tag{4.4}$$

where $\mathbf{\Omega} = \Omega \hat{\mathbf{e}}_z$ is an angular velocity vector, $\mathcal{S}_{kij}$ is a generalized Poynting flux tensor introduced in the previous chapter, ε_{ijk} is the Levi-Civita symbol, Φ is a gravitational potential, and other notations are standard. Note that the ideal Ohm's law, $\mathbf{E}+(\mathbf{v}/c)\times\mathbf{B} = 0$, is assumed throughout this chapter. The gravitational potential Φ in the shearing box with vertical gravity is given by

$$\Phi = -q\Omega^2 x^2 + \frac{1}{2}\Omega^2 z^2, \tag{4.5}$$

where $q = -d\ln\Omega/d\ln R$ is a shear parameter and we assumed $q = 3/2$, which corresponds to Keplerian rotation.

To mimic pitch-angle scattering owing to micro-instabilities driven by the pressure anisotropy, we adopt the hard-wall limit introduced in Sharma et al. (2006). This model sets maximum extent of the anisotropy, beyond which the pressure tensor is isotropized immediately till the marginal value. The detailed implementation of isotropization via the scattering model in our code is described in Appendix B.

In addition to gyrotropization and isotropization, furthermore, we implement the effect of cooling, or *isothermalization*, in a rather artificial manner. This step is required to

maintain vertical structure of the disk; without any cooling, the gas in a simulation box is heated up continuously, which makes the disk thicker and thicker. For the purpose of investigating long-term evolution under a statistically constant disk structure, therefore, the dissipated thermal energy must be removed from the computational domain. To achieve this, we employ a technique similar to the gyrotropization model. Once ρ and p_{ij} are found from equations (4.1) and (4.4), respectively, we can define the *isothermal* pressure tensor,

$$\mathbf{p}_{cool} = \rho c_s^2 \, \frac{3\mathbf{p}}{p_{xx} + p_{yy} + p_{zz}}, \tag{4.6}$$

where c_s is the speed of sound assumed to be uniform and constant. Equation (4.6) renormalizes the pressure tensor so that the diagonal average of $\mathbf{p}$, which is directly proportional to the total thermal energy, becomes identical with the isothermal value ρc_s^2, while the ratios between every two components of the pressure tensor unchange. Then, the pressure is made to approach $\mathbf{p}_{cool}$ nearly instantaneously by

$$\left.\frac{\partial \mathbf{p}}{\partial t}\right|_{cool} = -\nu_{cool} \left(\mathbf{p} - \mathbf{p}_{cool}\right), \tag{4.7}$$

with ν_{cool} assumed to be a large number compared to, for example, the disk rotation frequency Ω.

4.2.2 Initial and boundary conditions

Equations (4.1)–(4.4) in combination with isotropization and cooling models are solved as an initial- and boundary-value problem. Initially, we assume purely azimuthal differential rotation expanded linearly in the local shearing box,

$$\mathbf{v}_K = -q\Omega x \hat{\mathbf{e}}_y. \tag{4.8}$$

Suppose that the gas pressure is isotropic at $t = 0$. The stratified disk is, then, given by a vertical hydrostatic balance. By the use of isothermal relation, we obtain

$$\rho = \rho_0 \exp\left(-z^2/H^2\right), \tag{4.9}$$

$$\mathbf{p} = p_0 \mathbf{I} \exp\left(-z^2/H^2\right), \tag{4.10}$$

where ρ_0 is the mid-plane density, $p_0 = \rho_0 c_s^2$ is the mid-plane pressure, and $H = \sqrt{2}c_s/\Omega$ is a disk thickness. A magnetic field is imposed upon this disk structure. In this chapter, the sinusoidally changing vertical field is considered,

$$\mathbf{B} = B_0 \sin\left(\frac{2\pi x}{L_x}\right)\hat{\mathbf{e}}_z, \tag{4.11}$$

where B_0 is the maximum field strength, and L_x is the radial dimension of the simulation domain. It is known that the intensity of MRI-driven turbulence is highly sensitive to the net vertical magnetic flux, which vanishes in the present configuration. As mentioned in section 1.4.1, this zero-net-flux model is motivated by the fact that there is no obvious observational ground that a black hole accretion flow is threaded by large-scale, external magnetic flux.

The above initial configuration is in magnetohydrodynamical equilibrium. To drive growth of MRIs, we superpose a random, isentropic perturbation on the density and the gas pressure, the amplitude of which is 0.1% of the local background value. For the consistency with Hawley et al. (1995), a velocity perturbation is also added with the amplitude of 0.02% of c_s.

We adopt the shearing periodic boundary condition in x-direction, which is an essentially periodic boundary while the effect of the background shear is taken into account (Hawley et al., 1995; Stone & Gardiner, 2010). Practically, this is achieved by data shift along the azimuthal flow after the periodic boundary condition is applied. In y-direction, a purely periodic boundary is employed.

A particular issue on stratified disk simulations comes into discussion when the vertical boundary is considered. We assume a periodic boundary in z-direction, while it appears to be unrealistic in a present stratified box. The extent to which the employment of the periodic vertical boundary affects the disk dynamics has been discussed by several authors. Stone et al. (1996) compares two runs each of which adopts the periodic boundary condition or the outflow boundary condition with an additional vertical domain including strong viscosity and resistivity. This extended region works as a dumping layer, which is necessary to avoid spurious Lorentz force arising from an artificially snipped magnetic field line at the boundary. They concluded that both vertical structure and volume averaged quantities do not show any significant difference between two runs. Davis et al. (2010), on the other hand, performs simulations with vertical dimensions of $4H$ and $6H$ using a

periodic boundary. They also made conclusion that the nature of MRI turbulence and the angular momentum transport in both cases look quite similar to each other, and hence, the four-scaleheight run associated with the periodic boundary yields robust estimates on properties of disk turbulence. In our implementation, the gravitational potential is modified to connect values at top and bottom boundaries smoothly, as described in Davis et al. (2010), i.e.

$$\frac{1}{2}\Omega^2 z^2 \to \frac{1}{2}\Omega^2 \left(\sqrt{(z_0 - |z|)^2 + \lambda^2} - z_0 \right)^2, \tag{4.12}$$

where z_0 indicates the position of the top or bottom boundary, and λ is a thickness of the smoothing region. We set $\lambda = 0.1H$.

4.2.3 Code

The code we use in this chapter is a higher-order version of that described in the previous chapter, namely, fifth order of accuracy in space and third order in time. The gyrotropization, isotropization, and cooling procedures are combined in an operator splitting manner.

For the purpose of reducing and homogenizing errors which arise from the background shearing velocity, we employ the orbital advection technique introduced in Stone & Gardiner (2010). The orbital advection scheme decomposes basic equations (4.1)–(4.4) into two systems by making use of the fact that the background shear flow velocity $\mathbf{v}_K$ is constant in time. One is the usual MHD system where $\mathbf{v}' = \mathbf{v} - \mathbf{v}_K$ is evolved rather than $\mathbf{v}$ itself, with slight modification on the shearing source terms. The other system describes the linear advection due to the background shear flow, which can be solved analytically. See Stone & Gardiner (2010) for technical details developed in the standard MHD. For completeness sake, implementation in the present model with an anisotropic pressure is summarized in Appendix C.

4.3 Results

Important parameters and spatially and temporally averaged stress in our simulations are summarized in Table 4.1. The three-dimensional simulation domain of radial, azimuthal and vertical coordinates is $(x, y, z) \in [-H/2, H/2] \times [0, 4H] \times [-2H, 2H]$ in all cases. Each run is labeled by A (with anisotropic pressure) or I (with isotropic pressure), and 32 and 64 indicate the number of grid points per scaleheight, shown in the second column. Runs

A32 are further distinguished by lower-case alphabets. The third column is the simulation end time. The plasma beta and the gyrotropization frequency employed in each run are shown in the forth and fifth columns, respectively. Throughout this chapter, double brackets $\langle\langle f \rangle\rangle$ represent spatial averages over the whole simulation domain and temporal averages after 50 orbits unless otherwise specified, while single brackets $\langle f \rangle$ indicate only spatial averages. The averaged Reynolds, Maxwell, and anisotropic stress normalized by the mid-plane pressure are recorded in the remaining columns.

Table 4.1: Simulation summary

Run	Resolution	Orbits	β	ν_{g0}/Ω	$\langle\langle \rho v_x v_y \rangle\rangle / p_0$	$\langle\langle -B_x B_y \rangle\rangle / p_0$	$\langle\langle p_{xy} \rangle\rangle / p_0$
A32a	$32/H$	300	10^2	10^{13}	0.0014	0.0044	0.0020
A32b	$32/H$	100	10^3	10^{13}	0.0013	0.0040	0.0020
A32c	$32/H$	100	10^4	10^{13}	0.0015	0.0050	0.0019
A32d	$32/H$	100	10^2	10^8	0.0016	0.0049	0.0019
A32e	$32/H$	300	10^2	10^3	0.0016	0.0065	0.0020
A64	$64/H$	20	10^2	10^{13}	0.0034	0.0124	0.0040
I32	$32/H$	300	10^2	—	0.0017	0.0062	—
I64	$64/H$	20	10^2	—	0.0018	0.0082	—

Note: Double brackets denote spatial averages over whole simulation domain and temporal averages after 50 orbits expect for A64 where averages are taken after 10 orbits.

Comparison among Runs A32a–A32c shows that the magnitude of the initial magnetic field does not affect statistics in the later stage both in qualitative and quantitative manners. This agreement essentially arises from the fact that, in zero-net flux simulations, the system has no typical scale of a magnetic flux. Once the initial magnetic structure is stirred by nonlinear growth of MRIs, therefore, information on the initial field is forgotten completely and the systems tend to reach the same statistical steady state. Then, we fix the value of the initial β at 100 in other runs.

4.3.1 Fiducial run

We regard Run A32a as a fiducial case, and let us review the result in this section. In Fig. 4.1, color contours of the density (left half) and the azimuthal magnetic field (right half) normalized by ρ_0 and B_0, respectively, during the initial stage from 2 to 3.25 orbits are shown with the time interval of 0.25 orbits. At first, the growth of the MRI becomes prominent at the outer regions with roughly $|z| > H$, while the linear theory in a uniform medium predicts that the maximum growth rate is 0.75Ω ubiquitously. As time goes on,

MRI-driven channel sheets appear inside the disk as well. After 3 orbits, they finally break down into turbulence through magnetic reconnection. This compressible turbulence disturbs the disk structure as seen in the density contours at 3 and 3.25 orbits, but the stratification is maintained statistically throughout the simulation even under the presence of pressure anisotropy, which is discussed in detail later.

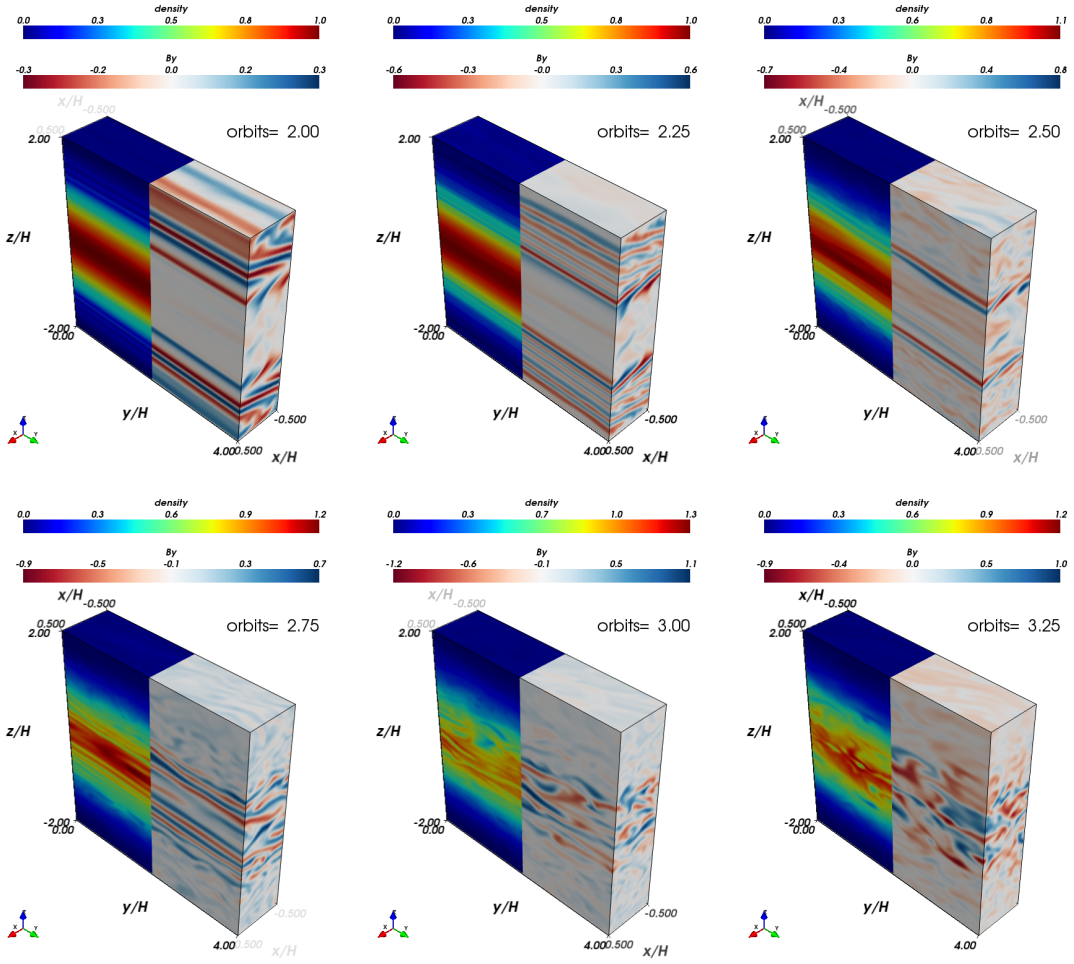

Figure 4.1: Snapshots during the initial phase of the MRI from Run A32a. The left and right halves in each panel show contours of the mass density and the azimuthal magnetic field, normalized by the mid-plane density and the maximum field strength at the initial state, respectively.

4.3.1.1 Statistics

After 3–4 orbits passes, the simulation box is filled with chaotic turbulent motion. Statistics of various quantities are summarized in Table 4.2. For a comparison purpose, we also show statistics for Run I32, where all conditions are the same as in Run A32a except for

the use of isotropic pressure. The second and fourth columns from the left represent averages both in space and in time, while the third and fifth columns show standard deviations of volume averaged values, which indicate magnitude of temporal fluctuation.

From energy distribution in Table 4.2, we can see that the properties of turbulent fluctuation in two runs are quite similar with each other. Magnetic energy, for example, is distributed into each directional component related to B_x, B_y and B_z, respectively, roughly in the ratio of 0.1:0.85:0.05 in common, and kinetic energy is $\sim 40\%$ of the total magnetic energy. The magnitudes both in the kinetic and magnetic energy, however, decrease by $\sim 20\%$ in A32a compared with in I32. The qualitatively same relation holds as well for stress; both Reynolds and Maxwell stresses are reduced by $\sim 20\%$ with the nearly constant ratio between them. In Run A32a, we also have additional angular momentum transport by anisotropic stress, p_{xy}. The value of this anisotropic stress seems merely comparable to contribution from the Reynolds stress. However, the 20 percent reduction of other stress is compensated by p_{xy}, and the total transport efficiency does not change significantly. The bottommost two rows in Table 4.2 compare parallel and perpendicular pressures averaged over the simulation. As qualitatively predicted from the double adiabatic approximation, in an average sense $p_\perp$ dominates $p_{||}$, which causes the positive p_{xy} by combination with the positive Maxwell stress, because the anisotropic stress can be written as $p_{xy} \simeq \left(-B_x B_y/B^2\right)\left(p_\perp - p_{||}\right)$ when the gyrotropic assumption holds well. [1]

4.3.1.2 Volume-averaged stress

Fig. 4.2 exhibits the time histories of volume-averaged Reynolds, Maxwell, anisotropic, and total stress for Runs A32a and I32. Each quantity shows highly chaotic behavior. In particular, the Maxwell stress is strongly intensified intermittently with the interval which sometimes exceeds several dozen orbits. This is the reason why considerably long duration like 300 orbits is required to obtain a temporally averaged, representative value in shearing box simulations of MRI-driven turbulence (Winters et al., 2003).

Fig. 4.3 also shows each stress averaged over the whole simulation domain after 50 orbits, but plotted as functions of the instantaneous magnetic energy. The green scattered points clearly indicate strong correlation between the Maxwell stress and the magnetic energy. The slope of the regression line is 0.27, while the Reynolds stress shows weaker dependence with the slope of 0.054. The anisotropic stress, on the other hand, exhibits

[1] Taking the xy-component of a gyrotropic pressure tensor $\mathbf{p} = p_\perp \mathbf{I} + \left(p_\parallel - p_\perp\right)\mathbf{BB}/B^2$.

Table 4.2: Statistics for Runs A32a and I32

	A32a		I32	
Quantity f	$\langle\langle f\rangle\rangle \times 10^2$	$\sigma_{\langle f\rangle} \times 10^2$	$\langle\langle f\rangle\rangle \times 10^2$	$\sigma_{\langle f\rangle} \times 10^2$
$\rho v_x^2/2p_0$	0.27	0.081	0.35	0.112
$\rho v_y^2/2p_0$	0.15	0.054	0.22	0.095
$\rho v_z^2/2p_0$	0.17	0.044	0.19	0.066
$B_x^2/2p_0$	0.12	0.057	0.19	0.091
$B_y^2/2p_0$	1.18	0.576	1.51	0.823
$B_z^2/2p_0$	0.06	0.029	0.10	0.046
$\rho v_x v_y/p_0$	0.14	0.050	0.17	0.068
$-B_x B_y/p_0$	0.47	0.181	0.60	0.239
p_{xy}/p_0	0.20	0.058	—	—
$\left(p_{\|\|} - \langle p\rangle_{t=0}\right)/p_0$	-0.49	0.165	—	—
$\left(p_\perp - \langle p\rangle_{t=0}\right)/p_0$	0.15	0.083	—	—

Note: Single brackets denote spatial averages over whole simulation domain.
σ_X is a standard deviation for a quantity X.

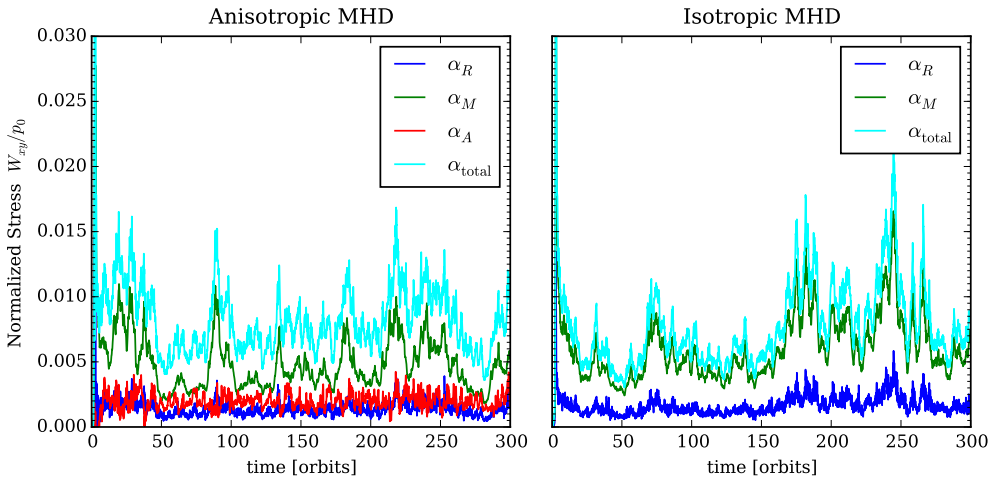

Figure 4.2: Time variation of α-parameters averaged over the whole simulation domain in Runs A32a (left) and I32 (right). Contribution from Reynolds (blue), Maxwell (green), anisotropic (red, only in the anisotropic run), and total (cyan) stress are plotted with different colors.

no clear dependence with a slightly negative slope for the linear regression line. This tendency looks quite different from that observed in an unstratified simulation (see Fig. 3 in Sharma et al. (2006)). For more details, we need to see spatial structure, which will be discussed in the next section.

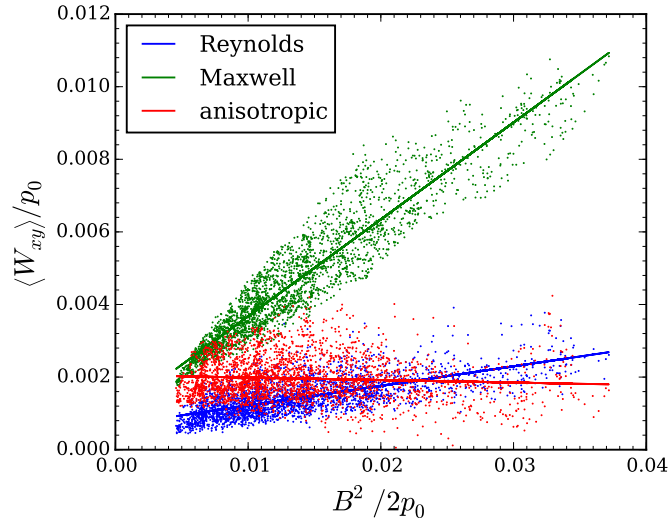

Figure 4.3: Dependence of each stress on instantaneous magnetic energy. The solid lines are results of linear fitting.

4.3.1.3 Vertical structure

Since the present system involves stratification, it becomes possible to study vertical dependence of various quantities, which is a great advantage of the scale-free model. One of the graphical methods helpful to understand the vertical structure is a spacetime diagram. It shows a quantity averaged along a horizontal plane as a two-dimensional function of both a vertical position and time. Figs. 4.4 and 4.5 compare the spacetime diagrams for Runs A32a and I32, respectively. From top to bottom, we plot the color contours of the plasma beta in logarithmic scale, the radial and azimuthal magnetic flux, the Maxwell stress, and the anisotropic stress (only in A32a), each of which is properly non-dimensionalized by the initial mid-plane pressure.

From the top three panels, we can see the evidence that strongly magnetized patches generated near the disk mid-plane buoyantly rise toward the boundary regions. The magnetic flux piled up near the boundaries is apparently the spurious result of the use of periodic boundary condition in the vertical direction. As we already mentioned, however, this structure does not affect the behavior inside the disk with $|z/H| \lesssim 1$, where the MRI is highly active. In particular, the bottom two panels show that both the Maxwell and anisotropic stress do not have any corresponding structure near the boundaries, so the statistics of each stress in the previous section should not be largely altered by the choice of boundary condition. Looking at a sign of the azimuthal field in the rising patches (and also in the piled up field near the boundary), we can observe quasi-periodic reversals. This

characteristic pattern is thought as an indication of an underlying dynamo effect, and has been observed commonly in previous MHD simulations in the collisional regime.

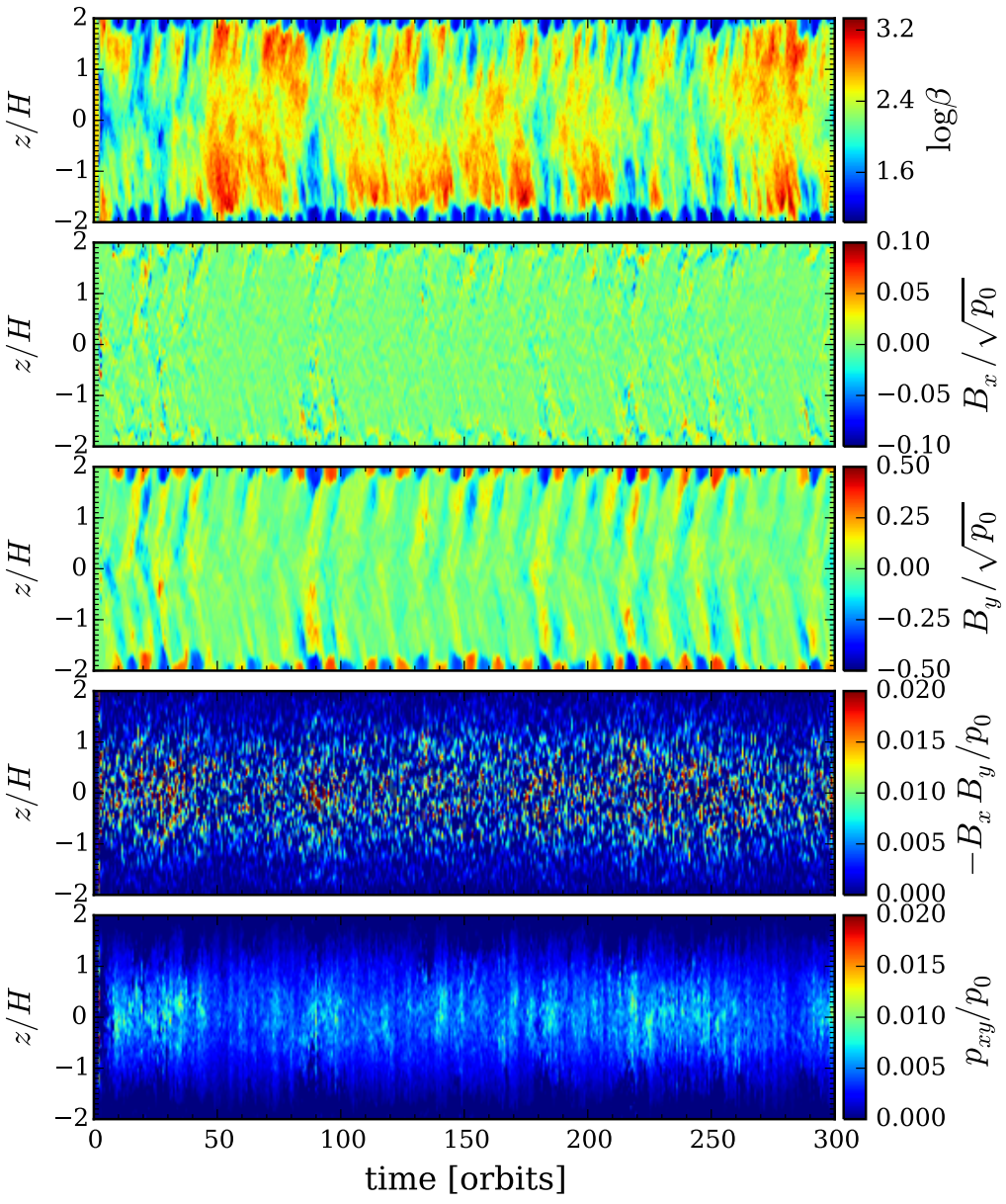

Figure 4.4: Horizontally averaged structure of various quantities in the anisotropic run as functions of vertical position and time in Run A32a. From top to bottom, we plot the plasma beta, the radial magnetic field, the azimuthal magnetic field, the Maxwell stress, and the anisotropic stress.

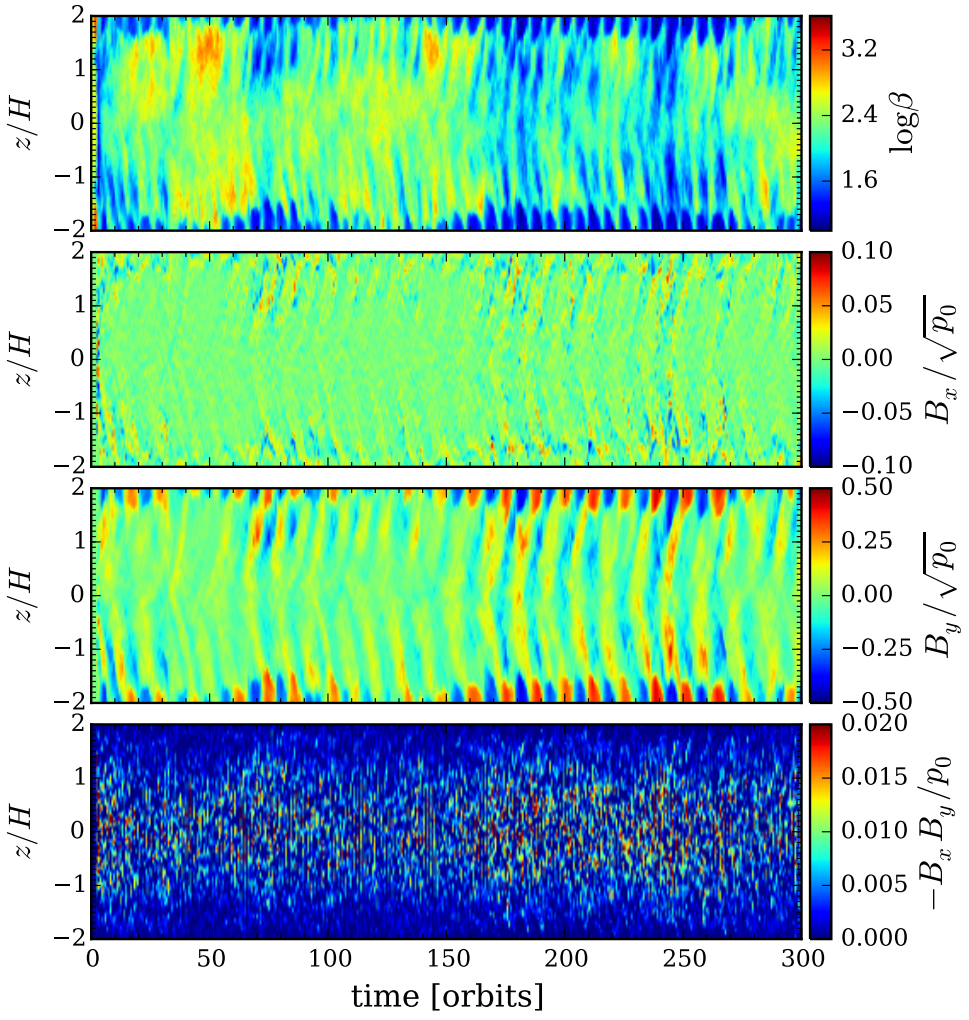

Figure 4.5: Spacetime diagrams in the isotropic Run I32 with the same format as in Fig. 4.4.

By comparison with Run I32 shown in Fig. 4.5, it can be said that the magnetic structure described here is qualitatively same as in the isotropic case. The vertical distribution of the anisotropic stress, however, is rather different from other two components. To make this point clearer, we take a further average about time after 50 orbits. It yields temporally and horizontally averaged, one-dimensional vertical profiles of the stress in Fig. 4.6, where each stress is colored in the same way as in Fig. 4.2. Again, the left and right panels represent the results for Runs A32a and I32, respectively.

It is remarkable that the anisotropic stress localizes around the disk mid-plane, while

the Maxwell and Reynolds components have broader structure over the wide range of height as well as in the isotropic MHD run. As a result, the total efficiency of angular momentum transport also has a localized profile rather than a flat, or two-peak, distribution like obtained in I32 and previous studies (Davis et al., 2010). This localization indicates that, for angular momentum transport in collisionless disks, the effect of the background structure of an accretion disk could be more essential than expected in collisional disks. In particular, although unstratified shearing box simulations have predicted the magnitude of anisotropic stress comparable to the Maxwell stress, our stratified model shows it is true only at the deep inside of the disk, $|z/H| \lesssim 0.5$, and the anisotropic stress decreases gradually, but more sharply than other stress, as z moves away from the disk mid-plane. Note that it is not surprising that the results of unstratified models well agree with the activity around the mid-plane, because the vertical gravity is proportional to z.

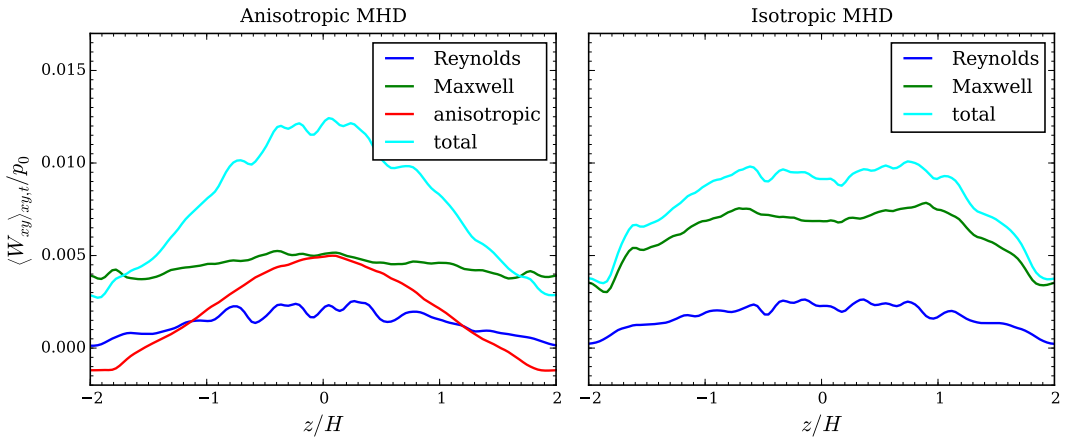

Figure 4.6: Comparison of vertical structure of horizontally and temporally averaged stress between Runs A32a and I32.

The localization of the anisotropic stress seems to be explained as follows. α_A, which is a part of α carried by anisotropic stress, can be written as

$$\alpha_A = \frac{p_{xy}}{p_0} \simeq \left(\frac{p_\perp - p_{||}}{B^2}\right)\left(\frac{-B_x B_y}{p_0}\right) = \left(\frac{\beta_\perp - \beta_{||}}{2}\right)\alpha_M, \tag{4.13}$$

where α_M is the Maxwell stress normalized by p_0. It means that, even if anisotropy is somewhat uniform in the sense of $p_\perp/p_{||}$, α_A can vary largely depending on the magnitude of diagonal components in the pressure tensor itself. This argument is illustrated in Fig. 4.7. From top to bottom, plotted are the horizontally and temporally averaged profiles of the parallel and perpendicular pressure, the ratio and the difference between

them, and the magnetic energy density, respectively, within $|z/H| \leq 1.5$ where the spurious boundary effect is relatively weak. The first and second panels show that the anisotropy $p_\perp/p_{||}$ is rather uniform inside the disk, $|z/H| \simeq 1$, in the sense of their ratio, with the stratification maintained. The anisotropic stress, however, is determined by the difference of $p_\perp$ and $p_{||}$, which is plotted in the third panel, and it shows a convex profile due to the stratification. Since the magnetic energy density has quite flat structure as shown in the bottommost panel, the profile of anisotropic stress becomes nearly proportional to the stratified pressure. Although it might seem an apparent consequence, this is undoubtedly the first quantitative estimate of the anisotropic stress in a collisionless accretion disk including the disk scale.

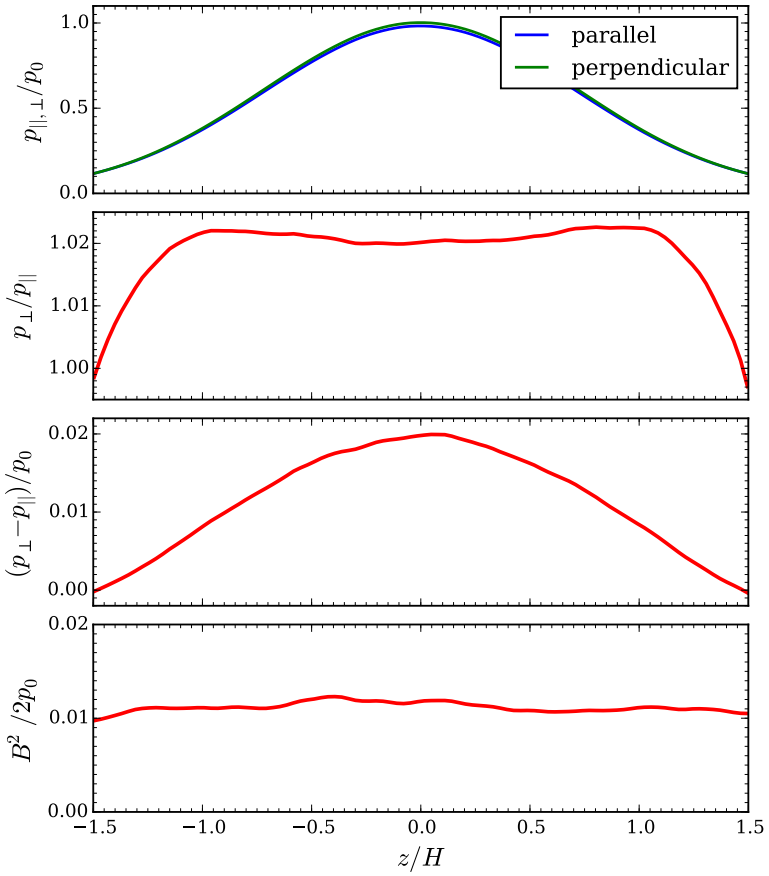

Figure 4.7: Horizontally and temporally averaged profiles of the variables related to anisotropic stress, p_{xy}.

4.3.2 Resolution dependence

Convergence of solutions with respect to the number of grid points is an issue of importance for numerical simulations. The grid convergence of statistics in a shearing box model during a saturated stage of the MRI has also been investigated intensively. Focusing ourselves to calculations with no net magnetic flux, it is known that the turbulent stress in cases without explicit dissipation and vertical gravity becomes smaller and smaller without bound as the higher resolution is employed (Pessah et al., 2007; Fromang & Papaloizou, 2007; Guan et al., 2009). This absence of convergence has been a long-standing mystery of a shearing box model. A resolution study using Athena code reported in Davis et al. (2010), however, argued that they observed convergence of the saturation amplitude of MRI-driven turbulence with the resolution up to 128 grid points per scale height, once the vertical gravity and the resultant stratification is retained. In contrast, Bodo et al. (2014) revisited the same problem with ampler computational resources by PLUTO code, and observed *no* evidence of convergence with resolution up to 200 grid points per scale height. The grid convergence of turbulent stress in a shearing box model is still an open question.

In the case of our model as well, it is significant to assess the dependence of the transport efficiency on the number of grid points. We list in Table 4.1 the results using different resolutions with 32 and 64 grid points per scale height in Runs A32a and A64 (I32 and I64 for isotropic pressure). Note that the Reynolds and Maxwell stress in Run I64 are in remarkably good agreement with those obtained in Run S64R1Z4 reported in Davis et al. (2010), which corresponds to the same calculation with our Run I64. Run A64, on the other hand, shows more sensitive increase in every component of stress, and the total transport efficiency exceeds the isotropic counterpart. The duration of the high resolution run, however, is limited to only 20 orbits due to the restriction of currently available computational resource. This duration is apparently not sufficient at all to obtain a meaningful representative value from highly chaotic turbulence, since the interval of intermittent behavior can reach several dozens of orbits, as we already mentioned. We leave more precise and robust study on convergence by simulations lasting several hundreds of orbits to future work.

4.3.3 Dependence on gyrotropization model

Our model to deal with an anisotropic pressure tensor introduces a new timescale, or a frequency, to control how fast the pressure tensor approaches to its gyrotropic asymptote. It would be necessary to clarify the dependence of our results on this parameter. The gyrotropization frequency enters into the system through the last term in equation (4.4), where

$$\nu_g = \left(\frac{|\mathbf{B}|}{B_0}\right)\nu_{g0}, \tag{4.14}$$

is set to be proportional to the local magnetic field strength normalized by a fiducial value, B_0. In all our calculations, B_0 is fixed at the initial maximum value of the magnetic field for $\beta = 100$, i.e., $B_0 = \sqrt{2p_0/10^2}$, which is also a typical field strength during the saturated stage. Runs A32a, A32d and A32e in Table 4.1 employ different values of ν_{g0}: 10^{13}, 10^8 and 10^3 in unit of the rotation frequency of the disk, Ω. These choice of ν_{g0} roughly yield $\nu_{g0}\Delta t \simeq 10^{10}$, 10^5 and 1, respectively, at a site of the typical magnetic field, using a simulation time step defined to satisfy the CFL condition (3.37). We, therefore, expect the quantitatively similar results for Runs A32a and A32d, where $\nu_g\Delta t \gg 1$, and the statistics shown in Table 4.1 successfully demonstrate it.

Run A32e, on the other hand, shows the Maxwell stress increased by $\sim 40\%$, while the Reynolds and anisotropic contribution remain unchanged. The magnetic energy is also increased by 35%. This enhancement may be traced to reduction of released magnetic energy via magnetic reconnection under the presence of large non-gyrotropy. In section 3.4.3.3, we illustrated that the eigenmodes which are not present in a gyrotropic framework can support a current sheet without raising up an explosive reconnection event and releasing magnetically stored energy. To obtain a supporting evidence for this assertion, we make plots for occurrence frequencies of non-gyrotropy in Fig. 4.8. The vertical axis indicates a measure of non-gyrotropy, which is defined as an L_2-norm of a residue of a pressure tensor from its gyrotropic limit normalized by the mid-plane pressure;

$$\begin{aligned}\Delta\hat{p} &\equiv \frac{1}{p_0}\sqrt{\sum_{i,j}\left|p_{ij} - p_{g,ij}\right|^2}, \\ &= \frac{1}{p_0}\sqrt{(p_{xx} - p_{g,xx})^2 + (p_{xy} - p_{g,xy})^2 + \cdots + (p_{zz} - p_{g,zz})^2}.\end{aligned}$$

The horizontal axis is a magnetic field strength in a logarithmic scale, and the number of

cells counted during 50–100 orbits is shown by the color contour. From left to right, each panel shows the result for Runs A32a, A32d and A32e, respectively.

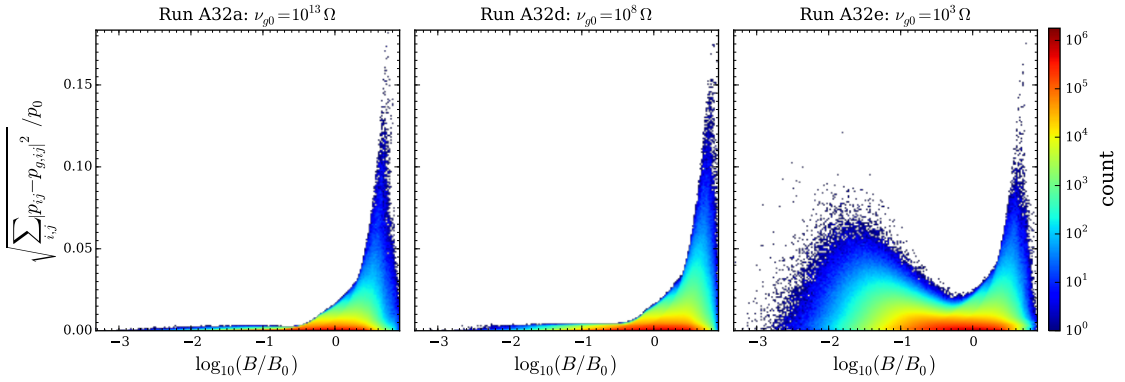

Figure 4.8: Occurrence frequencies of a measure of non-gyrotropy and magnetic field strength, for Runs A32a, A32d and A32e using different gyrotropization frequencies.

Again, the left two panels for Runs A32a and A32d show the quite similar results; a majority of data crowds around a narrow region along $\Delta\hat{p} \simeq 0$. Note that $\nu_g \Delta t \gg 1$ holds over all the range of the field strength in these two runs. In the rightmost panel for the smallest value of ν_{g0}, however, the large non-gyrotropy with at most $\Delta\hat{p} \simeq 0.1$ remains in weakly magnetized regions, which can be thought as sites where magnetic reconnection takes place. The extent to which this highly nonuniform non-gyrotropy alters the dynamics of reconnection is still unclear. Nevertheless, in a qualitative sense at least, our result seems consistent with the suppression of reconnection by the non-gyrotropic entropy modes.

The enhanced stress in Run A32e highlights the important role of deviation from gyrotropic pressure, which updates the previous result of the shearing box simulation with the gyrotropic framework by Sharma et al. (2006). Even though the volume occupancy of weakly magnetized regions with finite non-gyrotropy is not so large, it can have a significant impact on entire large-scale dynamics through the process of magnetic reconnection. This is a good example of multi-scale coupling typical in collisionless plasmas, and we have suggested a new aspect of micro-physics to be taken into account in large-scale collisionless plasmas.

4.3.3.1 Combined model of rotation and gyrotropization

For the purpose of showing one of the possible orientations toward improvement of our gyrotropization model, we have tried numerical experiments including the effect of rotation

of a pressure tensor in addition to gyrotropization; we solve

$$\frac{\partial p_{ij}}{\partial t} = \Omega_c \left(\varepsilon_{ikl} p_{jk} \hat{b}_l + \varepsilon_{jkl} p_{ik} \hat{b}_l \right) - \nu_g \left(p_{ij} - p_{g,ij} \right),$$

instead of only the gyrotropization represented by the last term. This is motivated by the fact that the original form of this operator simply describes rotation of a pressure tensor by cyclotron motion of particles (see equation (3.12)). By solving this term analytically in an operator splitting manner, the effect that a particle incoming into a neutral sheet quickly changes its direction of cyclotron motion, which is one of the essential physics in magnetic reconnection, may be incorporated into a system. Practically, since our model employs a one-fluid framework, we have to determine the direction in which particles rotate. In the present application, suppose the pressure is mainly supported by ions, and a positive value is adopted for Ω_c.

In order to clarify the role of this rotation term particularly on magnetic reconnection, let us reconsider the same one-dimensional Riemann problem as described in section 3.4.3 by setting $\Omega_c = (B/B_0)\,\Omega_{c0}$ and $\nu_{g0} = 0$. The results adopting different values of the rotation frequency, i.e., $\Omega_{c0} L/V_A = 10^0$, 10^{-2} and 10^{-4} are shown in Figs. 4.9 to 4.11, respectively. By comparison of Figs. 3.5 and 4.9, it is remarkable that when Ω_{c0}^{-1} takes the same order as the Alfvén transit time across the initial current sheet, the resultant structure of the reconnection layer is the almost same as that observed under a gyrotropic limit in spite of the absence of any explicit gyrotropization term. The resemblance with the gyrotropic case would be traced to redistribution of non-gyrotropic components generated at a certain gyrophase into a wide range of gyrophases. The fast rotation, therefore, tends to randomize non-gyrotropy, which effectively works like gyrotropization, although it is not guaranteed that the non-gyrotropy vanishes eventually. The only major difference from the gyrotropic limit is behavior of the rotational discontinuities around $|x/L| \sim 90$, where the response of various quantities are anti-symmetric between leftward and rightward propagating waves. This symmetry breaking apparently arises from the assumption that the pressure is supported only by positive charges, i.e., $\Omega_c > 0$, and thus reflects the direction of the local magnetic field.

When the rotation is slower than the dynamical timescale like shown in Fig. 4.10 with $\Omega_{c0} = 10^{-2} V_A/L$, the reconnection layer becomes quite complicated and highly asymmetric. It is no longer straightforward to understand the structure based on propagation of

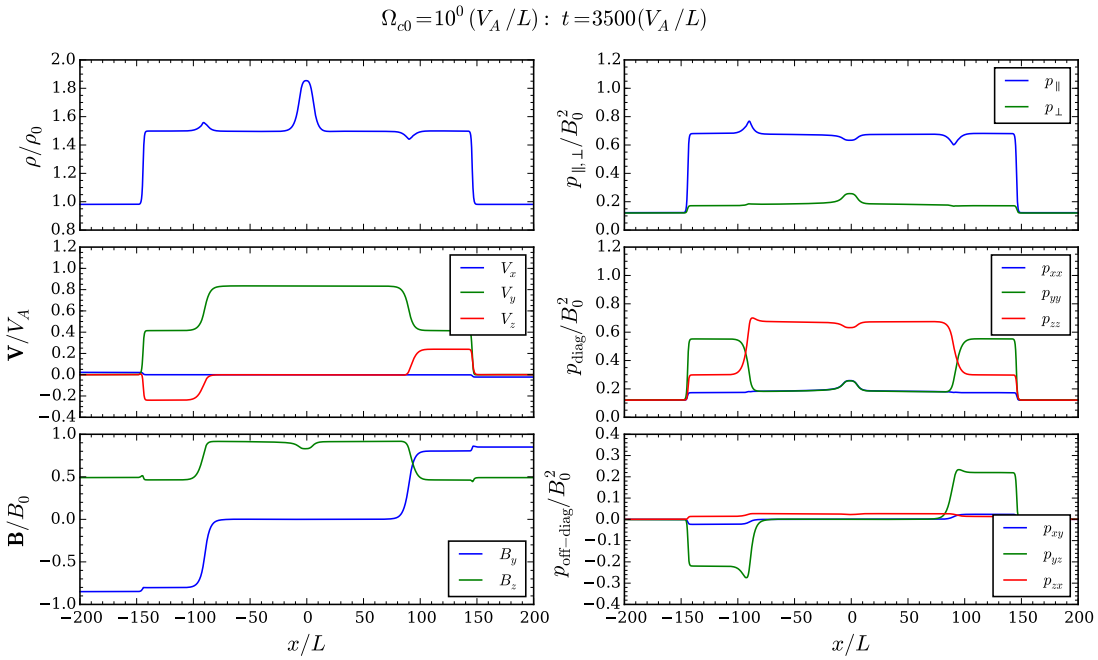

Figure 4.9: Results of the one-dimensional Riemann problem at $t = 3500$ including only the rotation term with $\Omega_{c0} = 10^0$.

isolated waves. Once the rotation frequency is further decreased by two orders of magnitude, however, the system shows no explosive reconnection as shown in Fig. 4.11. This naturally occurs by the same mechanism described in section 3.4.3.3 and Fig. 3.6 there, while the assumption of positive Ω_c causes a slight leftward migration of the contact discontinuity.

As we have seen in this section, the rotation term works in a qualitatively similar way to the gyrotropization model used in this thesis, which reinforces the validity of our parameterization to some extent. In spite of the similarity, inclusion of this original rotation term still has an advantage. We observed that, when applied to stratified disk simulations, it becomes possible to employ smaller ν_{g0} than listed in Table 4.1 for the first time by the use of the combined model; otherwise the simulation with, for example, $\nu_{g0} = 10\Omega$ breaks down due to appearance of negative density. To the contrary, a merit of incorporating with the gyrotropization model is to guarantee the consistency with a gyrotropic limit in an asymptotic manner by reducing non-gyrotropy explicitly.

4.3.3.2 Application to stratified disk simulations

In this section, let us apply the combined model described above to our stratified disk model. For simplicity we assume $\Omega_{c0} = \nu_{g0}$ here. Simulation parameters and the resultant

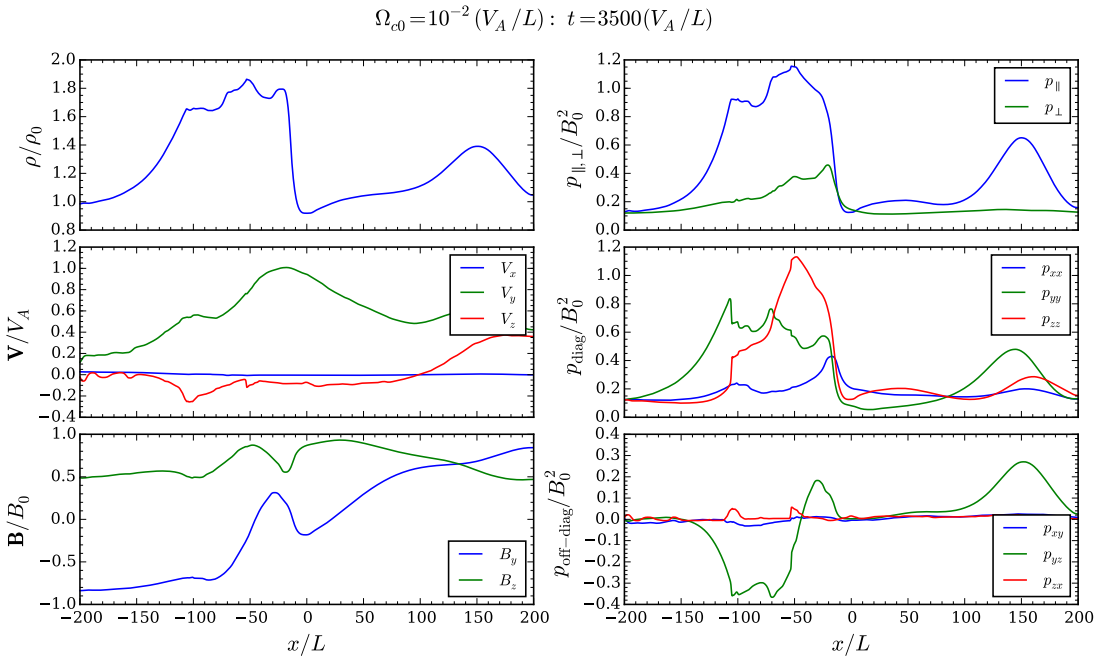

Figure 4.10: Results of the one-dimensional Riemann problem at $t = 3500$ including only the rotation term with $\Omega_{c0} = 10^{-2}$.

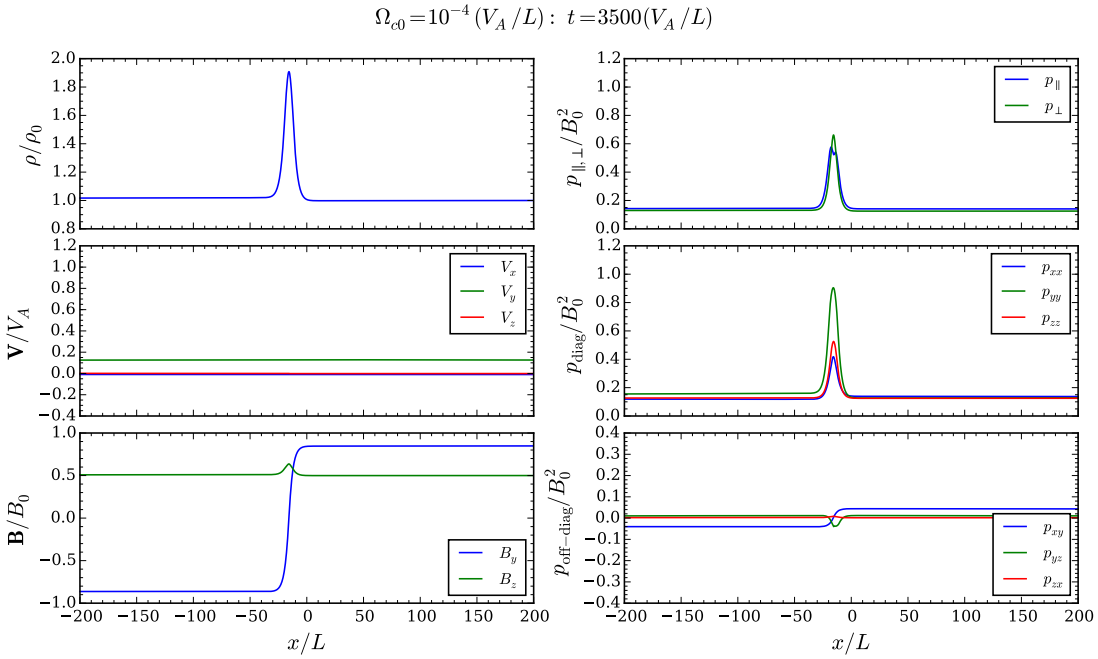

Figure 4.11: Results of the one-dimensional Riemann problem at $t = 3500$ including only the rotation term with $\Omega_{c0} = 10^{-4}$.

stress averaged both in space and in time are summarized in Table 4.3 with the same format as in Table 4.1. Each run is labeled with R (with rotation). From Run R32a to Run R32d, the frequency common to gyrotropization and rotation procedures is changed.

Table 4.3: Simulation summary for rotation + gyrotropization model

Run	Resolution	Orbits	β	ν_{g0}/Ω	$\langle\langle \rho v_x v_y \rangle\rangle / p_0$	$\langle\langle -B_x B_y \rangle\rangle / p_0$	$\langle\langle p_{xy} \rangle\rangle / p_0$
R32a	$32/H$	300	10^2	10^{13}	0.0014	0.0045	0.0019
R32b	$32/H$	300	10^2	10^8	0.0015	0.0048	0.0020
R32c	$32/H$	300	10^2	10^3	0.0016	0.0057	0.0021
R32d	$32/H$	300	10^2	10^1	0.0019	0.0121	0.0090

The dependence of the stress on ν_{g0} are illustrated in Fig. 4.12 along with the averaged plasma beta. The A32 and R32 serieses are represented by circles and squares, respectively. We can clearly see that two serieses are in both qualitative and quantitative agreement for $\nu_{g0} \gtrsim 10^3\Omega$, which ensures that the current model is an appropriate extension of the original model when a pressure tensor is well gyrotropized. The intensive enhancement in the Maxwell and anisotropic stress is, however, observed when ν_{g0} is further decreased to 10Ω in Run R32d, and the magnetic energy also increases roughly by three times compared with the case of $\nu_{g0} = 10^3\Omega$. Although these facts seem to imply a more efficient *dynamical* suppression of magnetic reconnection by a non-gyrotropic pressure, the increase not only in the Maxwell stress but also in the anisotropic stress may be related to a process slightly different from the case in A32e or R32c. For example, it is known in kinetic description that charged particles entering a reconnection layer experience Speiser orbits toward the direction of the electric field along an X-line. The situation particularly in a shearing box is illustrated in Fig. 4.13. Since the magnetic field is continuously stretched to x-direction by the MRI and to y-direction by the background differential rotation, the reconnection is expected to occur in a plane inclined both from (x, z)- and (y, z)-planes, like the shaded region in Fig. 4.13. Thus the population in Speiser orbits tends to have the correlation of $\langle v_x v_y \rangle > 0$, which contributes to positive p_{xy} in a quite non-gyrotropic manner. Getting back to our fluid model, although each particle's orbit is not resolved, it could be possible to generate this non-gyrotropic p_{xy} by distorting and rotating the pressure of incoming flux with large $p_\perp$. This effect cannot be captured when only gyrotropization is assumed, where the anisotropy around the magnetic field remains in the constant direction. To demonstrate this hypothesis, however, requires more detailed study on magnetic reconnection itself in an isolated system. Anyway, the result here emphasizes the striking dependence of an angular momentum transport efficiency on the ratio between the cyclotron frequency and the disk's rotation frequency. Note that, since the previous PIC simulations by Hoshino (2015) assumed a small ratio $\Omega_c/\Omega =$

10 for saving computational resources, there might be a possibility to overestimate the suppression effect due to the non-gyrotropic distribution function. It is to be hoped that future research will clarify this point.

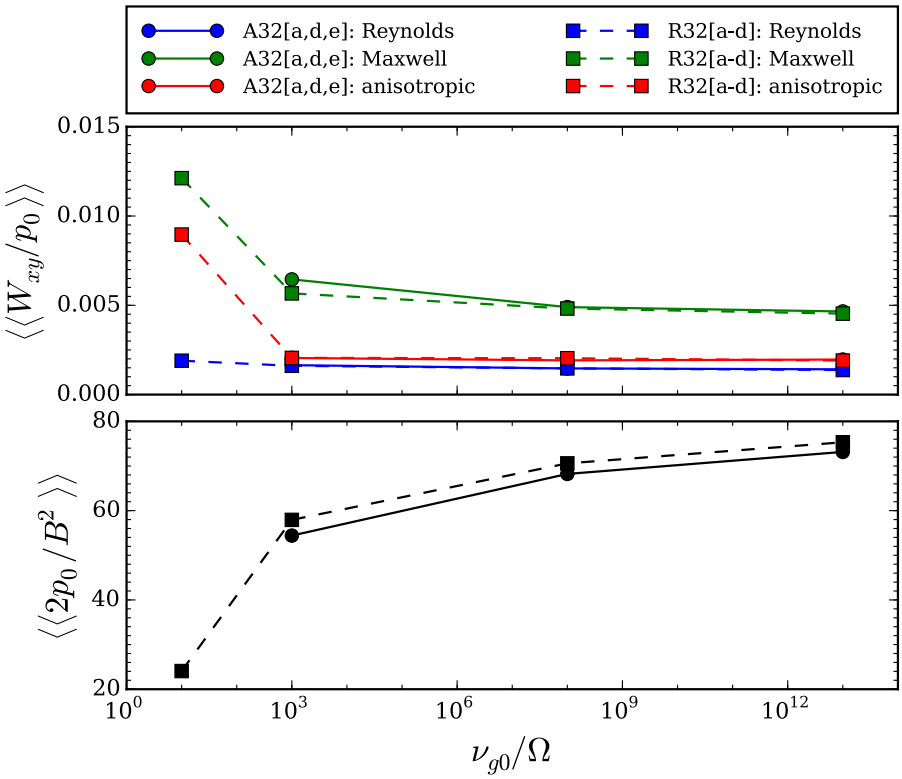

Figure 4.12: Dependence of stress and plasma beta on a gyrotropization and cyclotron frequency. The circles connected with solid lines are the cases with only gyrotropization, and the squares connected with dashed lines indicate the result of the gyrotropization and rotation model.

4.4 Discussion and summary

In this chapter, we have conducted a series of stratified shearing box simulations in collisionless regime using our newly developed kinetic MHD model. This is the first approach to large-scale dynamics of collisionless accretion disks. In particular, it is designed to fill the gap between the double adiabatic simulations assuming gyrotropic pressure and fully kinetic simulations, which cannot handle disk scales.

The main results of importance are summarized as follows:

1. The volume- and time-averaged total efficiency of angular momentum transport remains at the same level as in isotropic MHD simulations.

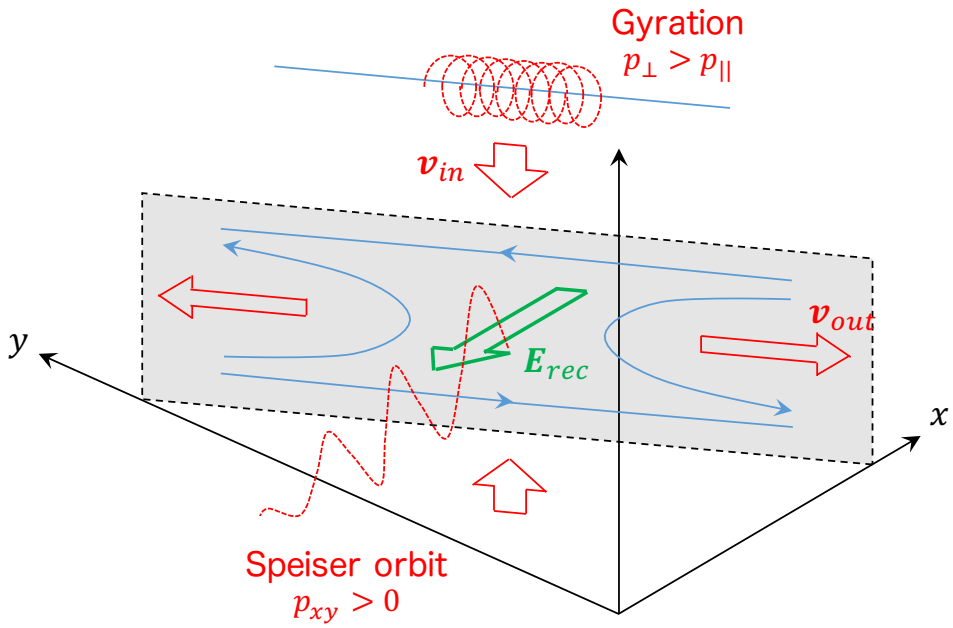

Figure 4.13: A schematic picture of a reconnection layer expected in a shearing box simulation.

2. The distribution ratio of the Reynolds, Maxwell, and anisotropic stress agrees with unstratified simulations only near the disk mid-plane, and anisotropic stress decreases outwardly.

3. The results are not affected by the choice of an artificial parameter to determine the gyrotropization rate, as long as it is sufficiently large.

4. Once the gyrotropization rate approaches a dynamical time scale of a disk, finite non-gyrotropy around neutral sheets tends to enhance the Maxwell stress.

Although the result 1 looks the same argument claimed in the previous study of unstratified simulations using the double adiabatic model (Sharma et al., 2006), the contribution from the anisotropic stress is only comparable to the Reynolds stress, rather than to the Maxwell stress as predicted in the unstratified case. The properties of the unstratified shearing box model is well reproduced only around the disk mid-plane, where the effect of vertical gravity is weak and stratification can be ignored in good approximation. The stratified pressure, however, yields strong dependence of the anisotropic stress on the vertical position. Specifically, as stated in result 2, the anisotropic stress decreases outwardly away from the mid-plane reflecting stratification of the diagonal pressure, while the Maxwell and the Reynolds stress have broader distribution. This fact apparently suggests

that the large-scale structure be more essential for angular momentum transport in a collisionless accretion disk than expected in a collisional disk where thermal pressure cannot carry angular momentum. Our results must be an important foothold to understand more global behavior of collisionless disks in the future.

A self-similar solution for Sgr A* based on the ADAF model (Narayan & Yi, 1994) predicts that the ratio of the cyclotron frequency to the rotation frequency of the disk largely depends on an orbital radius, but it is in general expected to be much greater than unity. Result 3 relieves us of a distress about the practical choice of a gyrotropization frequency. When it is artificially set to a value comparable to a dynamical frequency, on the other hand, the energy release through magnetic reconnection could be suppressed by finite non-gyrotropy, and efficient transport is likely to be sustained by the increased Maxwell stress. This result 4 is qualitatively consistent to PIC simulations in Hoshino (2015), though we have to take care that the physics to suppress the reconnection process would be quite different. It is a highly challenging matter of interest to improve our current model to capture this suppression effect, which is believed to reflect *micro*-physics in part, while a large gyrotropization rate is maintained outside the current sheets, where *macro*-physics plays a role. Note that the role of non-gyrotropy in the context of MRIs was not discussed either in fully kinetic PIC simulations by Hoshino (2015), where suppression of magnetic reconnection and the resultant enhancement of angular momentum transport were accounted for only in terms of the gyrotropic anisotropy with $p_{||} > p_{\perp}$. While there have been theoretical and numerical studies on non-gyrotropic electron pressure, which strongly affects the physics of resistivity, and hence the magnetic reconnection, through the generalized Ohm's law (e.g., Hesse & Winske, 1993, 1994; Yin & Winske, 2003), the dynamical role has not been discussed with interest. The simple test problem provided in section 3.4.3.3 and its indirect application to a larger system demonstrated here emphasize the necessity to see the importance of non-gyrotropic components of a pressure tensor in a new light.

It should be noted that our model currently does not include the effect of resistivity, which is another large issue to determine saturation amplitudes of the MRI-driven turbulence. The lack of resistivity is because the distribution of thermal energy generated by Joule heating into each component of a pressure tensor cannot be determined within the fluid framework. This means that magnetic reconnection occurs only through numerical dissipation in the current model, and the heating rate of each component of a pressure

tensor is not under control. We, however, could employ a model of the heating rates, for example, based on the idea that the Joule heating is mainly carried by electrons which isotropize instantaneously. Conversely, it is possible to construct a model of anisotropic heating of ions. To investigate the dependence of the present results on resistivity models is also left for future work to be discussed.

Chapter 5

General Discussion

5.1 Summary of this thesis

Throughout this thesis, we have investigated the anomalous angular momentum transport by magnetohydrodynamic (MHD) turbulence in accretion disks, particularly in the context of α-viscosity. More specifically, in chapter 2, the magneto-gradient driven instability (MGDI) is proposed as a new process to drive MHD turbulence from a toroidal magnetic flux in a *collisional* disk. The MGDI has the property that it occurs along a horizontal plane of the disk, in contrast to the case of the conventional magnetorotational instability (MRI), where vertically propagating waves play essential roles. Thus, these two unstable modes are more likely to grow complementarily rather than competitively. As we have seen, the Maxwell stress induced by the MGDI is proportional to the externally imposed toroidal magnetic flux, and $\alpha \sim \mathcal{O}(0.1)$ seems to be attained for a relatively strong magnetic field with $\beta \lesssim 10$. It is widely confirmed that the strong toroidal field commonly arises in three-dimensional simulations even without any external flux. This *internally* induced toroidal field would work just like an *external* flux for local perturbations, which can seed the MGDI. We, however, have to keep in mind that the nature of turbulence can be different between two- and three-dimensional problems. More precise quantitative estimates on contribution of the MGDI requires fully three-dimensional analyses; nevertheless we believe that the physical essence of the instability is quite general and does not change even in more complicated three-dimensional cases.

In contrast, chapters 3 and 4 have discussed dynamics of more dilute gas which should be treated as a *collisionless* plasma. While chapter 3 was designed to make preparations for collisionless disk simulations provided in chapter 4, the methodology newly developed in

chapter 3 itself has an importance from the viewpoint of plasma physics. The new kinetic MHD model is a successful attempt at including the effect of an anisotropic distribution function into the framework of one-fluid MHD as much as possible by allowing a pressure tensor in a more general form than gyrotropic formulation, which enables us to resolve magnetically neutral regions without any numerical difficulty. While there still remains several courses of improvement to be considered particularly related to the relaxation procedure, the fluid model introduced in this thesis is a first step of great significance to make a closer link between the MHD theory to govern macro-scale phenomena and the kinetic theory to describe micro-scale physics. The future applications include much variety of large-scale collisionless phenomena studied in the discipline of space and astrophysics.

Chapter 4, in particular, applied the developed kinetic MHD model to a series of shearing box simulations of accretion disks incorporated with vertical gravity, and investigated the impact of an anisotropic pressure on angular momentum transport in a collisionless disk. The results provided in this thesis shows that the total efficiency of the angular momentum transport is not so much different from the level predicted in collisional regime, while the additional transport due to anisotropic pressure is revealed to localize near the disk mid-plane. This localization apparently the consequence of the stratification, which cannot be studied by a fully kinetic approach. It implies that the transport process expected in a collisionless disk, particularly due to the pressure anisotropy, depends on the background disk structure more largely than in a collisional disk, where only the Maxwell and Reynolds stress can contribute to the angular momentum transport, and strongly invokes the necessity of collisionless global simulations, for which the present model will be expected to play an effective role.

Another significant result is a moderate enhancement of the Maxwell stress by bringing a newly introduced time scale of gyrotropization and a dynamical time scale close to each other. We obtained the indirect evidence that finite non-gyrotropy remaining particularly in the vicinity of neutral sheets may reduce the amount of magnetic energy released via magnetic reconnection, which eventually increases the Maxwell stress as well. The reduction of released energy is qualitatively consistent with anticipation from the simple one-dimensional problem to mimic magnetic reconnection without any gyrotropization in chapter 3. This result revises the argument in Hoshino (2015) that the parallel pressure enhancement in reconnection exhaust suppresses the successive reconnection itself, where only gyrotropic pressure is taken into account, although a difference in the parameter

range resolved in kinetic and fluid approaches need to be kept in mind. We must, furthermore, remind you that other existing MHD codes incorporated with anisotropic pressure based on the double adiabatic formulation cannot explore the role of non-gyrotropy as demonstrated in this thesis. Research on the effect of non-gyrotropy in the framework of completely scale-free, one-fluid magnetohydrodynamics is just getting started.

Finally, let us summarize our current understanding of MRI-driven turbulence with and without vertical gravity obtained by different approaches in Table 5.1. Note that the basic properties of the MRI are adequately captured in all frameworks: standard MHD, CGL-based gyrotropic MHD, the present kinetic MHD with non-gyrotropy, and fully kinetic PIC/Vlasov model. The capability to describe kinetic effects increases from left to right. The standard MHD, which does not involve any kinetic effect due to the assumption of high collisionality and/or isotropization, is applicable both to a totally local shearing box model without any typical spatial scale of a disk and to a vertically stratified shearing box model in association with the disk's scale height. Although the estimated efficiencies of angular momentum transport are smaller than the observational requirement roughly by an order of magnitude, the effects of excessive numerical viscosity and resistivity on saturation amplitude of MRI-driven turbulence are still an open question. Our attempt at extension of a one-fluid framework to include kinetic physics more is located between the previous CGL-based kinetic MHD model and fully kinetic PIC or Vlasov model, in the sense that handling of the pressure anisotropy in the vicinity of neutral sheets is taken into account, while the scale-free property is retained. Although the obtained enhancement of angular momentum transport by inclusion of non-gyrotropy was moderate and did not reach the stage to account for efficient transport on observational ground, it should be recognized as a great step to put forward our understanding on the role of collisionless effects in black-hole accretion flows.

5.2 Future prospects

As a closing section of this thesis, we would like to mention future work and applications. As we already pointed out, angular momentum transport by anisotropic pressure in a collisionless accretion disk seems to be largely subject to the structure of the disk. In this thesis, the effect of vertical stratification has been considered. A real accretion disk, however, stratifies also in radial direction. Such an effect can no longer be captured by

Table 5.1: Summary of simulation studies of MRIs.

	Collisional	**Collisionless**		
Model	**MHD**	**MHD+CGL**	**This thesis**	**PIC/Vlasov**
Kinetic effect	×	Anisotropy	Anisotropy Nongyrotropy	○
Micro instability	—	PAS model	PAS model	○
MRI	○	○	○	○
Disk scale	○	○	○	×
Neutral sheets	—	×	△	○
α **(local)**	10^{-4}–10^{-2}	∼MHD	∼MHD	~ 0.1
α **(stratified)**	$\lesssim 10^{-2}$		10^{-3}–10^{-2}	×

Note: PAS = pitch-angle scattering

a shearing box model, and a genuinely global model is necessary. A global disk simulation is one of the apposite future applications of this work, and it would bring about more quantitative understanding of advection-dominated accretion flows, which might be comparable with observational understandings. In particular, once the relativistic version of our model is developed, the jet formation at a collisionless, black-hole accretion flow will become accessible, although it has been investigated by collisional MHD models conventionally.

It is also a fundamental issue to be worked out in more detail how the anisotropy and the non-gyrotropy of a pressure tensor regulate the reconnection process in the present model. To organize this point necessarily involves elucidating which physical process *is* or *is not* included in the system, compared with the original Vlasov-Maxwell system. Note that there have been investigation of the effect of electron pressure anisotropy, the divergence of which enters the system electromagnetically through the generalized Ohm's law. It is known that the inertia resistivity and/or the anisotropy of the electron pressure work as a source of anomalous resistivity to enhance the magnetic reconnection in a collisionless system. Our one-fluid kinetic MHD model, on the other hand, involves the dynamical role of a pressure tensor in the equations of motion and energy, but the simplest ideal Ohm's law is still employed in the induction equation so far and the reconnection takes place via numerical resistivity. To integrate the spontaneous mechanism of anomalous resistivity into the present model is a highly challenging matter, since what we really need is a one-

fluid model by which we can enjoy the scale-free property; nevertheless, the methodology itself to resolve all components of a pressure tensor should work even when the system is extended to a multi-fluid model. The role of anisotropic pressure in magnetic reconnection is still an open question, and we believe that there will be a lot of aspects which our model can contribute to in the future.

Appendix A

Higher Order Implementation

In the text, our 2nd-order implementation is described in detail to clarify the differences from the standard MHD code. Here, we provide an example of a more accurate implementation by employing a 5th-order spatial scheme and a 3rd-order temporal scheme.

In terms of the procedure in Section 3.3.4, step 2 is first replaced by the 5th-order WENO interpolation (Jiang & Shu, 1996),

$$\mathbf{W}_{L,j+1/2} = w_1\mathbf{W}^{(1)} + w_2\mathbf{W}^{(2)} + w_3\mathbf{W}^{(3)}, \tag{A.1}$$

where $\mathbf{W}^{(i)}$ represents the 3rd-order linear interpolation using different stencils,

$$\mathbf{W}^{(1)} = \frac{3}{8}\mathbf{W}_{j-2} - \frac{5}{4}\mathbf{W}_{j-1} + \frac{15}{8}\mathbf{W}_j, \tag{A.2}$$

$$\mathbf{W}^{(2)} = -\frac{1}{8}\mathbf{W}_{j-1} + \frac{3}{4}\mathbf{W}_j + \frac{3}{8}\mathbf{W}_{j+1}, \tag{A.3}$$

$$\mathbf{W}^{(3)} = \frac{3}{8}\mathbf{W}_j + \frac{3}{4}\mathbf{W}_{j+1} - \frac{1}{8}\mathbf{W}_{j+2}. \tag{A.4}$$

The normalized nonlinear weights, $w_i = \hat{w}_i/(\hat{w}_1 + \hat{w}_2 + \hat{w}_3)$, are chosen to reduce to small numbers around discontinuities as

$$\hat{w}_i = \frac{\gamma_i}{(\beta_i + 10^{-6})^2}, \tag{A.5}$$

with optimum weights

$$\gamma_1 = \frac{1}{16}, \quad \gamma_2 = \frac{5}{8}, \quad \gamma_3 = \frac{5}{16}, \tag{A.6}$$

which ensures convergence to the 5th-order linear interpolation in smooth regions. β_i, the

global smoothness indicator (Levy et al., 2000), is the weighted average of the smoothness indicator for each variable,

$$\beta_i = \frac{1}{N_d} \sum_{d=1}^{N_d} \frac{\beta_i^d}{||W^d||^2}, \tag{A.7}$$

where $N_d = 13$ indicates the number of independent variables, and β_i^d is the smoothness indicator for the d-th variable, defined as

$$\beta_1^d = \frac{13}{12}\left(W_{j-2}^d - 2W_{j-1}^d + W_j^d\right)^2 + \left(\frac{W_{j-2}^d - 4W_{j-1}^d + 3W_j^d}{2}\right)^2, \tag{A.8}$$

$$\beta_2^d = \frac{13}{12}\left(W_{j-1}^d - 2W_j^d + W_{j+1}^d\right)^2 + \left(\frac{W_{j-1}^d - W_{j+1}^d}{2}\right)^2, \tag{A.9}$$

$$\beta_3^d = \frac{13}{12}\left(W_j^d - 2W_{j+1}^d + W_{j+2}^d\right)^2 + \left(\frac{3W_j^d - 4W_{j+1}^d + W_{j+2}^d}{2}\right)^2. \tag{A.10}$$

By employing reverse stencils, $\mathbf{W}_{R,j-1/2}$ can also be obtained in the same way. Note that the coefficients described here are not for reconstruction, but for interpolation. Employing the interpolation scheme as a point value enables us to use various kinds of Riemann solvers in the context of a finite-difference approach as well, and to couple the scheme with the CT method.

Next, the conversion from a point-value to a numerical flux must be carried out for $\mathbf{F}_{L,R}$ and $\mathbf{D}_{L,R}$ before taking two-point differences in step 7. This can be achieved by comparing the coefficients in the Taylor expansion (Shu & Osher, 1988). The 6th-order formula, for example, is obtained from

$$\hat{\mathbf{f}}_{j\pm1/2} = \mathbf{f}_{j\pm1/2} - \frac{\Delta x^2}{24}\left.\frac{\partial^2 \mathbf{f}}{\partial x^2}\right|_{j\pm1/2} + \frac{7\Delta x^4}{5760}\left.\frac{\partial^4 \mathbf{f}}{\partial x^4}\right|_{j\pm1/2}. \tag{A.11}$$

The 2nd- and 4th-order derivatives are evaluated by means of the simple central differences with 4th- and 2nd-order accuracy, respectively, which guarantees the 6th-order overall accuracy.

The derivatives for non-conservative terms using the minmod limiter in step 7 must also be replaced by a higher-order scheme. In our implementation, the face-centered values, $\mathbf{U}_{L,j+1/2}$ and $\mathbf{U}_{R,j-1/2}$, are calculated from the cell-centered values, $\mathbf{U}_j$, as numerical fluxes in the WENO scheme as well as in step 2. In this case, however, the coefficients are adjusted for reconstruction, as we do not need the interpolated value elsewhere. Now

Eqs. (A.2)–(A.4) are modified to

$$\mathbf{U}^{(1)} = \frac{1}{3}\mathbf{U}_{j-2} - \frac{7}{6}\mathbf{U}_{j-1} + \frac{11}{6}\mathbf{U}_j, \tag{A.12}$$

$$\mathbf{U}^{(2)} = -\frac{1}{6}\mathbf{U}_{j-1} + \frac{5}{6}\mathbf{U}_j + \frac{1}{3}\mathbf{U}_{j+1}, \tag{A.13}$$

$$\mathbf{U}^{(3)} = \frac{1}{3}\mathbf{U}_j + \frac{5}{6}\mathbf{U}_{j+1} - \frac{1}{6}\mathbf{U}_{j+2}. \tag{A.14}$$

The optimum weights also change to

$$\gamma_1 = \frac{1}{10}, \quad \gamma_2 = \frac{3}{5}, \quad \gamma_3 = \frac{3}{10}. \tag{A.15}$$

Use of these coefficients ensures that the two-point difference,

$$\left.\frac{\partial \mathbf{U}}{\partial x}\right|_j \simeq \frac{1}{\Delta x}\left(\mathbf{U}_{L,j+1/2} - \mathbf{U}_{R,j-1/2}\right), \tag{A.16}$$

has 5th-order of accuracy in smooth regions, while exhibiting non-osclillatory behavior around discontinuities.

Finally, the 2nd-order time integration (3.34) and (3.35) is replaced by the 3rd-order TVD Runge-Kutta method (Shu & Osher, 1988):

$$\mathbf{U}^{(1)} = \mathbf{U}^n - \Delta t \mathcal{L}\left(\mathbf{U}^n\right), \tag{A.17}$$

$$\mathbf{U}^{(2)} = \frac{3}{4}\mathbf{U}^n + \frac{1}{4}\left[\mathbf{U}^{(1)} - \Delta t \mathcal{L}\left(\mathbf{U}^{(1)}\right)\right], \tag{A.18}$$

$$\mathbf{U}^{n+1} = \frac{1}{4}\mathbf{U}^n + \frac{2}{3}\left[\mathbf{U}^{(2)} - \Delta t \mathcal{L}\left(\mathbf{U}^{(2)}\right)\right]. \tag{A.19}$$

Appendix B

Isotropization Model

In this thesis, the hard-wall limit employed by Sharma et al. (2006) is modified to use the analytic solution of Eq. (3.61), or explicitly,

$$\mathbf{P}^{n+1} = \mathbf{P}_s + (\mathbf{P}^n - \mathbf{P}_s)\, e^{-\nu_{\rm iso}\Delta t}, \tag{B.1}$$

where $\mathbf{P}_s$ is a marginal state of a certain kinetic instability. For the firehose, mirror, and ion-cyclotron instabilities, the following relations are satisfied, respectively:

$$\frac{P_{\perp,s}}{P_{||,s}} - 1 + \frac{B^2}{P_{||,s}} = -\frac{1}{2}, \tag{B.2}$$

$$\frac{P_{\perp,s}}{P_{||,s}} - 1 = \frac{\xi B^2}{P_{\perp,s}}, \tag{B.3}$$

$$\frac{P_{\perp,s}}{P_{||,s}} - 1 = S\left(\frac{B^2}{P_{||,s}}\right)^{1/2}, \tag{B.4}$$

where $\xi = 3.5$ and $S = 0.3$ are used here. Each equation can be solved for $P_{||,s}$ and $P_{\perp,s}$ if we impose the condition that the total thermal energy, which is proportional to a trace of the pressure tensor, is unchanged through scattering: i.e., the relation $P^n_{||} + 2P^n_{\perp} = P_{||,s} + 2P_{\perp,s}$ holds. Note that this condition guarantees energy conservation exactly, ${\rm Tr}\mathbf{P}^{n+1} = {\rm Tr}\mathbf{P}^n$. If the firehose instability turns on, for example, solving Eq. (B.2) leads to

$$P_{||,s} = {\rm Tr}\mathbf{P}^n + 2B^2, \tag{B.5}$$

$$P_{\perp,s} = \frac{{\rm Tr}\mathbf{P}^n}{2} - B^2. \tag{B.6}$$

The marginal states for the mirror and ion-cyclotron instabilities can also be calculated in the same way.

To avoid duplicated gyrotropization, it may be better to construct the marginal pressure tensor in a non-gyrotropic form. We adopt, therefore, the following prescription,

$$\mathbf{P}_s = \mathbf{R} \begin{pmatrix} \hat{P}_{11,s} & 0 & 0 \\ 0 & \alpha \hat{P}^n_{22} & \alpha \hat{P}^n_{23} \\ 0 & \alpha \hat{P}^n_{32} & \alpha \hat{P}^n_{33} \end{pmatrix} \mathbf{R}^T, \tag{B.7}$$

where $\mathbf{R}$ is a rotational matrix from the coordinate system aligned with a local magnetic field to the xyz coordinate system, $\hat{P}_{ij}$ $(i, j = 1, 2, 3)$ is a pressure component measured in field-aligned coordinates (the parallel direction is assumed for $i = 1$), $\hat{P}_{11,s} = P_{||,s}$, and $\alpha = P_{\perp,s}/P^n_{\perp}$. Convergence to this marginal state allows the pressure to retain finite non-gyrotropy, while the thermal energy contained in the parallel and perpendicular components is correctly redistributed.

Appendix C

Orbital Advection Scheme with Anisotropic Pressure

The orbital advection scheme introduced in Stone & Gardiner (2010) is a numerical technique to integrate MHD equations in a shearing box accurately and efficiently by decomposing the system into two subsystems; one is the simple linear system to describe advection by background differential rotation, and the other is the standard hyperbolic system with modified shearing source terms. Since the detailed numerical implementation is provided in Stone & Gardiner (2010), in this appendix, we only reproduce practical equations employed in our simulation code for the sake of completeness, along with comments on a few modifications required to apply the orbital advection scheme to the kinetic MHD model with an anisotropic pressure tensor.

We will decompose basic equations (4.1)–(4.4). The subsystem for linear advection can be written simply as follows;

$$\frac{\partial \rho}{\partial t} + v_K \frac{\partial \rho}{\partial y} = 0, \tag{C.1}$$

$$\frac{\partial \rho \mathbf{v}'}{\partial t} + v_K \frac{\partial \rho \mathbf{v}'}{\partial y} = 0, \tag{C.2}$$

$$\frac{\partial \mathbf{B}}{\partial t} - \nabla \times (v_K \hat{\mathbf{e}}_y \times \mathbf{B}) = 0, \tag{C.3}$$

$$\frac{\partial \mathbf{E}'}{\partial t} + v_K \frac{\partial \mathbf{E}'}{\partial y} = \mathbf{s}_{E'}, \tag{C.4}$$

where $v_K = -q\Omega x$ represents the background Keplerian velocity, $\mathbf{v}' = \mathbf{v} - v_K \hat{\mathbf{e}}_y$ is a deviation from the Keplerian rotation, $\mathbf{E}' = \rho \mathbf{v}' \mathbf{v}' + \mathbf{p} + \mathbf{B}\mathbf{B}$ is a generalized energy tensor,

and

$$\mathbf{s}_{E'} = -\left(\rho v'_x v'_y + p_{xy} - B_x B_y\right) \frac{dv_K}{dx} \begin{pmatrix} 0 & 1 & 0 \\ 1 & 2 & 1 \\ 0 & 1 & 0 \end{pmatrix}.$$

Since the advection velocity is purely along y-axis and constant in time, these equations can be integrated using their analytic solutions without constraint on the CFL condition. In practice, this procedure is implemented by the similar way as the shearing periodic boundary condition, although we must take special care of the divergence-free condition for a magnetic field. The right-hand side in equation (C.4) cannot be gathered up in a flux form, and is treated as a source term separately.

By subtracting equations (C.1)–(C.4) from equations (4.1)–(4.4), we find that the remaining part yields the following subsystem;

$$\frac{\partial \rho}{\partial t} + \nabla \cdot \left(\rho \mathbf{v}'\right) = 0, \tag{C.5}$$

$$\frac{\partial \rho \mathbf{v}'}{\partial t} + \nabla \cdot \left(\rho \mathbf{v}'\mathbf{v}' + \mathbf{p} + \frac{B^2}{2}\mathbf{I} - \mathbf{B}\mathbf{B}\right) = 2\rho\Omega v'_y \hat{\mathbf{e}}_x + (q-2)\,\rho\Omega v'_x \hat{\mathbf{e}}_y - \rho\Omega^2 z \hat{\mathbf{e}}_z, \tag{C.6}$$

$$\frac{\partial \mathbf{B}}{\partial t} - \nabla \times \left(\mathbf{v}' \times \mathbf{B}\right) = 0, \tag{C.7}$$

$$\begin{aligned} &\partial_t E'_{ij} + \partial_k \left(\rho v'_i v'_j v'_k + p_{ij} v'_k + p_{ik} v'_j + p_{jk} v'_i + \mathcal{S}'_{kij} + \mathcal{S}'_{kji}\right) \\ &= B_i v'_k \partial_k B_j + B_j v'_k \partial_k B_i - B_k v'_i \partial_j B_k - B_k v'_j \partial_i B_k \\ &\quad + v'_i s'_{g,j} + v'_j s'_{g,i} - \nu_g \left(p_{ij} - p_{g,ij}\right), \end{aligned} \tag{C.8}$$

where quantities with prime is evaluated using $\mathbf{v}'$ rather than $\mathbf{v}$ itself, and

$$\mathbf{s}'_g = \begin{pmatrix} 2\rho\Omega v'_x \\ -2\rho\Omega v'_y \\ -\rho\Omega^2 z \end{pmatrix}.$$

The gravitational and Coriolis forces are slightly modified from the original shearing box system. These equations are integrated in a standard manner as described in chapter 3. Note that equations (C.4) and (C.8) are reduced to equations (51) and (55) in Stone & Gardiner (2010), respectively, by taking their trace.

Bibliography

Abramowicz, M. A., Chen, X., Kato, S., Lasota, J.-P., & Regev, O. (1995). Thermal equilibria of accretion disks. *The Astrophysical Journal Letters*, *438*, L37–L39.

Abramowicz, M. A., Czerny, B., Lasota, J. P., & Szuszkiewicz, E. (1988). Slim accretion disks. *The Astrophysical Journal*, *332*, 646–658.

Amano, T. (2015). Divergence-free Approximate Riemann Solver for the Quasi-neutral Two-fluid Plasma Model. *Journal of Computational Physics*, *299*, 863–886.

Artemyev, A. V., Petrukovich, A. A., Nakamura, R., & Zelenyi, L. M. (2015). Statistics of intense dawn-dusk currents in the Earth's magnetotail. *Journal of Geophysical Research (Space Physics)*, *120*, 3804–3820.

Bai, X.-N. (2015). Hall Effect Controlled Gas Dynamics in Protoplanetary Disks. II. Full 3D Simulations toward the Outer Disk. *The Astrophysical Journal*, *798*, 84.

Balbus, S. A., & Hawley, J. F. (1991). A powerful local shear instability in weakly magnetized disks. I - Linear analysis. II - Nonlinear evolution. *The Astrophysical Journal*, *376*, 214–233.

Balbus, S. A., & Hawley, J. F. (1992). A Powerful Local Shear Instability in Weakly Magnetized Disks. IV. Nonaxisymmetric Perturbations. *The Astrophysical Journal*, *400*, 610–621.

Balbus, S. A., & Hawley, J. F. (1998). Instability, turbulence, and enhanced transport in accretion disks. *Reviews of Modern Physics*, *70*, 1–53.

Blandford, R. D., & Payne, D. G. (1982). Hydromagnetic flows from accretion discs and the production of radio jets. *Monthly Notices of the Royal Astronomical Society*, *199*, 883–903.

Blandford, R. D., & Znajek, R. L. (1977). Electromagnetic extraction of energy from Kerr black holes. *Monthly Notices of the Royal Astronomical Society*, *179*, 433–456.

Bodo, G., Cattaneo, F., Mignone, A., & Rossi, P. (2014). On the Convergence of Magnetorotational Turbulence in Stratified Isothermal Shearing Boxes. *The Astrophysical Journal Letters*, *787*, L13.

Bondi, H. (1952). On spherically symmetrical accretion. *Monthly Notices of the Royal Astronomical Society*, *112*, 195.

Brandenburg, A., Nordlund, A., Stein, R. F., & Torkelsson, U. (1995). Dynamo-generated Turbulence and Large-Scale Magnetic Fields in a Keplerian Shear Flow. *The Astrophysical Journal*, *446*, 741.

Brio, M., & Wu, C. C. (1988). An upwind differencing scheme for the equations of ideal magnetohydrodynamics. *Journal of Computational Physics*, *75*, 400–422.

Buat-Ménard, V., Hameury, J.-M., & Lasota, J.-P. (2001). The nature of dwarf nova outbursts. *Astronomy and Astrophysics*, *366*, 612–622.

Burch, J. L., Moore, T. E., Torbert, R. B., & Giles, B. L. (2015). Magnetospheric Multiscale Overview and Science Objectives. *Space Science Review*, .

Cannizzo, J. K., Shafter, A. W., & Wheeler, J. C. (1988). On the outburst recurrence time for the accretion disk limit cycle mechanism in dwarf novae. *The Astrophysical Journal*, *333*, 227–235.

Chandran, B. D. G., Dennis, T. J., Quataert, E., & Bale, S. D. (2011). Incorporating Kinetic Physics into a Two-fluid Solar-wind Model with Temperature Anisotropy and Low-frequency Alfvén-wave Turbulence. *The Astrophysical Journal*, *743*, 197.

Chandrasekhar, S. (1960). The Stability of Non-Dissipative Couette Flow in Hydromagnetics. *Proceedings of the National Academy of Science*, *46*, 253–257.

Chen, J., & Palmadesso, P. (1984). Tearing instability in an anisotropic neutral sheet. *Physics of Fluids*, *27*, 1198–1206.

Chew, G. F., Goldberger, M. L., & Low, F. E. (1956). The Boltzmann Equation and the One-Fluid Hydromagnetic Equations in the Absence of Particle Collisions. *Proceedings of the Royal Society of London Series A*, *236*, 112–118.

Ciesielski, A., Wielgus, M., Kluźniak, W., Sądowski, A., Abramowicz, M., Lasota, J.-P., & Rebusco, P. (2012). Stability of radiation-pressure dominated disks. I. The dispersion relation for a delayed heating α-viscosity prescription. *Astronomy and Astrophysics*, *538*, A148.

Davis, S. W., Stone, J. M., & Pessah, M. E. (2010). Sustained Magnetorotational Turbulence in Local Simulations of Stratified Disks with Zero Net Magnetic Flux. *The Astrophysical Journal*, *713*, 52–65.

Degond, P. (2013). Asymptotic-Preserving Schemes for Fluid Models of Plasmas. *Panoramas et Synthèses*, *39-49*, 1–90.

Degond, P., Deluzet, F., Sangam, A., & Vignal, M.-H. (2009). An Asymptotic Preserving scheme for the Euler equations in a strong magnetic field. *Journal of Computational Physics*, *228*, 3540–3558.

Del Sarto, D., Marchetto, C., Pegoraro, F., & Califano, F. (2011). Finite Larmor radius effects in the nonlinear dynamics of collisionless magnetic reconnection. *Plasma Physics and Controlled Fusion*, *53*, 035008.

Doeleman, S. S., Weintroub, J., Rogers, A. E. E., Plambeck, R., Freund, R., Tilanus, R. P. J., Friberg, P., Ziurys, L. M., Moran, J. M., Corey, B., Young, K. H., Smythe, D. L., Titus, M., Marrone, D. P., Cappallo, R. J., Bock, D. C.-J., Bower, G. C., Chamberlin, R., Davis, G. R., Krichbaum, T. P., Lamb, J., Maness, H., Niell, A. E., Roy, A., Strittmatter, P., Werthimer, D., Whitney, A. R., & Woody, D. (2008). Event-horizon-scale structure in the supermassive black hole candidate at the Galactic Centre. *Nature*, *455*, 78–80.

Dubus, G., Hameury, J.-M., & Lasota, J.-P. (2001). The disc instability model for X-ray transients: Evidence for truncation and irradiation. *Astronomy and Astrophysics*, *373*, 251–271.

Dumbser, M., & Balsara, D. S. (2016). A new efficient formulation of the HLLEM Riemann solver for general conservative and non-conservative hyperbolic systems. *Journal of Computational Physics*, *304*, 275–319.

Dumin, Y. V. (2002). The corotation field in collisionless magnetospheric plasma and its influence on average electric field in the lower atmosphere. *Advances in Space Research*, *30*, 2209–2214.

Evans, C. R., & Hawley, J. F. (1988). Simulation of magnetohydrodynamic flows - A constrained transport method. *The Astrophysical Journal*, *332*, 659–677.

Falcke, H., & Markoff, S. (2000). The jet model for Sgr A*: Radio and X-ray spectrum. *Astronomy and Astrophysics*, *362*, 113–118.

Fragile, P. C., & Blaes, O. M. (2008). Epicyclic Motions and Standing Shocks in Numerically Simulated Tilted Black Hole Accretion Disks. *The Astrophysical Journal*, *687*, 757–766.

Frank, J., King, A., & Raine, D. J. (2002). *Accretion Power in Astrophysics: Third Edition*.

Fromang, S., & Papaloizou, J. (2007). MHD simulations of the magnetorotational instability in a shearing box with zero net flux. I. The issue of convergence. *Astronomy and Astrophysics*, *476*, 1113–1122.

Galeev, A. A., & Zelenyĭ, L. M. (1976). Tearing instability in plasma configurations. *Soviet Journal of Experimental and Theoretical Physics*, *43*, 1113.

Gardiner, T. A., & Stone, J. M. (2005). An unsplit Godunov method for ideal MHD via constrained transport. *Journal of Computational Physics*, *205*, 509–539.

Genzel, R., Thatte, N., Krabbe, A., Kroker, H., & Tacconi-Garman, L. E. (1996). The Dark Mass Concentration in the Central Parsec of the Milky Way. *The Astrophysical Journal*, *472*, 153.

Ghez, A. M., Duchêne, G., Matthews, K., Hornstein, S. D., Tanner, A., Larkin, J., Morris, M., Becklin, E. E., Salim, S., Kremenek, T., Thompson, D., Soifer, B. T., Neugebauer, G., & McLean, I. (2003). The First Measurement of Spectral Lines in a Short-Period Star Bound to the Galaxy's Central Black Hole: A Paradox of Youth. *The Astrophysical Journal Letters*, *586*, L127–L131.

Goodman, J., & Xu, G. (1994). Parasitic instabilities in magnetized, differentially rotating disks. *The Astrophysical Journal*, *432*, 213–223.

Guan, X., Gammie, C. F., Simon, J. B., & Johnson, B. M. (2009). Locality of MHD Turbulence in Isothermal Disks. *The Astrophysical Journal*, *694*, 1010–1018.

Hada, T., Jamitzky, F., & Scholer, M. (1999). Consequences of nongyrotropy in magnetohydrodynamics. *Advances in Space Research*, *24*, 67–72.

Hammett, G. W., & Perkins, F. W. (1990). Fluid moment models for Landau damping with application to the ion-temperature-gradient instability. *Physical Review Letters*, *64*, 3019–3022.

Harten, A., Lax, P. D., & van Leer, B. (1983). On Upstream Differencing and Godunov-Type Schemes for Hyperbolic Conservation Laws. *SIAM Review*, *25*, 1–149.

Hau, L.-N., & Sonnerup, U. O. (1993). On slow-mode waves in an anisotropic plasma. *Geophysical Research Letters*, *20*, 1763–1766.

Hau, L.-N., & Wang, B.-J. (2007). On MHD waves, fire-hose and mirror instabilities in anisotropic plasmas. *Nonlinear Processes in Geophysics*, *14*, 557–568.

Hawley, J. F., & Balbus, S. A. (1991). A Powerful Local Shear Instability in Weakly Magnetized Disks. II. Nonlinear Evolution. *The Astrophysical Journal*, *376*, 223.

Hawley, J. F., & Balbus, S. A. (1992). A powerful local shear instability in weakly magnetized disks. III - Long-term evolution in a shearing sheet. *The Astrophysical Journal*, *400*, 595–609.

Hawley, J. F., Gammie, C. F., & Balbus, S. A. (1995). Local Three-dimensional Magnetohydrodynamic Simulations of Accretion Disks. *The Astrophysical Journal*, *440*, 742.

Hawley, J. F., Gammie, C. F., & Balbus, S. A. (1996). Local Three-dimensional Simulations of an Accretion Disk Hydromagnetic Dynamo. *The Astrophysical Journal*, *464*, 690.

Heinemann, M. (1999). Role of collisionless heat flux in magnetospheric convection. *Journal of Geophysical Research*, *104*, 28397–28410.

Hesse, M., Kuznetsova, M., & Birn, J. (2004). The role of electron heat flux in guide-field magnetic reconnection. *Physics of Plasmas*, *11*, 5387–5397.

Hesse, M., & Winske, D. (1993). Hybrid simulations of collisionless ion tearing. *Geophysical Research Letters*, *20*, 1207–1210.

Hesse, M., & Winske, D. (1994). Hybrid simulations of collisionless reconnection in current sheets. *Journal of Geophysical Research*, *99*, 11177–11192.

Hietala, H., Drake, J. F., Phan, T. D., Eastwood, J. P., & McFadden, J. P. (2015). Ion temperature anisotropy across a magnetotail reconnection jet. *Geophysical Review Letters*, *42*, 7239–7247.

Hirabayashi, K., & Hoshino, M. (2013). Magnetic reconnection under anisotropic magnetohydrodynamic approximation. *Physics of Plasmas*, *20*, 112111.

Hirabayashi, K., & Hoshino, M. (2016). Instability of Non-uniform Toroidal Magnetic Fields in Accretion Disks. *The Astrophysical Journal*, *822*, 87.

Hirabayashi, K., Hoshino, M., & Amano, T. (2016). A new framework for magnetohydrodynamic simulations with anisotropic pressure. *Journal of Computational Physics*, *327*, 851–872.

Hollweg, J. V. (1976). Collisionless electron heat conduction in the solar wind. *Journal of Geophysical Research*, *81*, 1649–1658.

Holzer, T. E., Fedder, J. A., & Banks, P. M. (1971). A comparison of kinetic and hydrodynamic models of an expanding ion-exosphere. *Journal of Geophysical Research*, *76*, 2453.

Hoshino, M. (2013). Particle Acceleration during Magnetorotational Instability in a Collisionless Accretion Disk. *The Astrophysical Journal*, *773*, 118.

Hoshino, M. (2015). Angular Momentum Transport and Particle Acceleration During Magnetorotational Instability in a Kinetic Accretion Disk. *Physical Review Letters*, *114*, 061101.

Hoshino, M., Saito, Y., Mukai, T., Nishida, A., Kokubun, S., & Yamamoto, T. (1997). Origin of hot and high speed plasmas in plasma sheet: plasma acceleration and heating due to slow shocks. *Advances in Space Research*, *20*, 973–982.

Ichimaru, S. (1977). Bimodal behavior of accretion disks - Theory and application to Cygnus X-1 transitions. *The Astrophysical Journal*, *214*, 840–855.

Jiang, G.-S., & Shu, C.-W. (1996). Efficient Implementation of Weighted ENO Schemes. *Journal of Computational Physics*, *126*, 202–228.

Jin, S. (1999). Efficient asymptotic-preserving (ap) schemes for some multiscale kinetic equations. *SIAM Journal on Scientific Computing*, *21*, 441–454.

Karimabadi, H., Roytershteyn, V., Vu, H. X., Omelchenko, Y. A., Scudder, J., Daughton, W., Dimmock, A., Nykyri, K., Wan, M., Sibeck, D., Tatineni, M., Majumdar, A., Loring, B., & Geveci, B. (2014). The link between shocks, turbulence, and magnetic reconnection in collisionless plasmas. *Physics of Plasmas*, *21*, 062308.

King, A. R., & Ritter, H. (1998). The light curves of soft X-ray transients. *Monthly Notices of the Royal Astronomical Society*, *293*, L42–L48.

Kowal, G., Falceta-Gonçalves, D. A., & Lazarian, A. (2011). Turbulence in collisionless plasmas: statistical analysis from numerical simulations with pressure anisotropy. *New Journal of Physics*, *13*, 053001.

Kulsrud, R. M. (1983). MHD description of plasma. In A. A. Galeev, & R. N. Sudan (Eds.), *Basic Plasma Physics: Selected Chapters, Handbook of Plasma Physics, Volume 1* (p. 1).

Kunz, M. W., & Lesur, G. (2013). Magnetic self-organization in Hall-dominated magnetorotational turbulence. *Monthly Notices of the Royal Astronomical Society*, *434*, 2295–2312.

Kunz, M. W., Stone, J. M., & Bai, X.-N. (2014). Pegasus: A new hybrid-kinetic particle-in-cell code for astrophysical plasma dynamics. *Journal of Computational Physics*, *259*, 154–174.

Kusunose, M., & Takahara, F. (2012). A Leptonic Model of Steady High-energy Gamma-Ray Emission from Sgr A*. *The Astrophysical Journal*, *748*, 34.

Levy, D., Puppo, G., & Russo, G. (2000). Compact Central WENO Schemes for Multidimensional Conservation Laws. *SIAM Review*, *22*, 656–672.

Lightman, A. P., & Eardley, D. M. (1974). Black Holes in Binary Systems: Instability of Disk Accretion. *The Astrophysical Journal Letters*, *187*, L1.

Liu, X.-D., Osher, S., & Chan, T. (1994). Weighted Essentially Non-oscillatory Schemes. *Journal of Computational Physics*, *115*, 200–212.

Liu, Y.-H., Drake, J. F., & Swisdak, M. (2012). The structure of the magnetic reconnection exhaust boundary. *Physics of Plasmas*, *19*, 022110–022110.

Londrillo, P., & del Zanna, L. (2004). On the divergence-free condition in Godunov-type schemes for ideal magnetohydrodynamics: the upwind constrained transport method. *Journal of Computational Physics*, *195*, 17–48.

Lynden-Bell, D., & Pringle, J. E. (1974). The evolution of viscous discs and the origin of the nebular variables. *Monthly Notices of the Royal Astronomical Society*, *168*, 603–637.

Machida, M., Hayashi, M. R., & Matsumoto, R. (2000). Global Simulations of Differentially Rotating Magnetized Disks: Formation of Low-β Filaments and Structured Coronae. *The Astrophysical Journal Letters*, *532*, L67–L70.

Machida, M., Matsumoto, R., & Mineshige, S. (2001). Convection-Dominated, Magnetized Accretion Flows into Black Holes. *Publication of the Astronomical Society of Japan*, *53*, L1–L4.

Marscher, A. P. (2006). X-ray and radio emission in the nuclei of radio galaxies and the disk-jet connection. *Astronomische Nachrichten*, *327*, 217–222.

Matsumoto, R., & Tajima, T. (1995). Magnetic viscosity by localized shear flow instability in magnetized accretion disks. *The Astrophysical Journal*, *445*, 767–779.

Matsumoto, R., Uchida, Y., Hirose, S., Shibata, K., Hayashi, M. R., Ferrari, A., Bodo, G., & Norman, C. (1996). Radio Jets and the Formation of Active Galaxies: Accretion Avalanches on the Torus by the Effect of a Large-Scale Magnetic Field. *The Astrophysical Journal*, *461*, 115.

McKinney, J. C., Tchekhovskoy, A., Sadowski, A., & Narayan, R. (2014). Three-dimensional general relativistic radiation magnetohydrodynamical simulation of super-Eddington accretion, using a new code HARMRAD with M1 closure. *Monthly Notices of the Royal Astronomical Society*, *441*, 3177–3208.

Mignone, A., Bodo, G., Massaglia, S., Matsakos, T., Tesileanu, O., Zanni, C., & Ferrari, A. (2007). PLUTO: A Numerical Code for Computational Astrophysics. *The Astrophysical Journal Supplement Series*, *170*, 228–242.

Mignone, A., Rossi, P., Bodo, G., Ferrari, A., & Massaglia, S. (2010). High-resolution 3D relativistic MHD simulations of jets. *Monthly Notices of the Royal Astronomical Society*, *402*, 7–12.

Mignone, A., Ugliano, M., & Bodo, G. (2009). A five-wave Harten-Lax-van Leer Riemann solver for relativistic magnetohydrodynamics. *Monthly Notices of the Royal Astronomical Society*, *393*, 1141–1156.

Miller, K. A., & Stone, J. M. (2000). The Formation and Structure of a Strongly Magnetized Corona above a Weakly Magnetized Accretion Disk. *The Astrophysical Journal*, *534*, 398–419.

Minoshima, T., Hirose, S., & Sano, T. (2015). Dependence of the Saturation Level of Magnetorotational Instability on Gas Pressure and Magnetic Prandtl Number. *The Astrophysical Journal*, *808*, 54.

Mizuno, Y., Hardee, P. E., & Nishikawa, K.-I. (2014). Spatial Growth of the Current-driven Instability in Relativistic Jets. *The Astrophysical Journal*, *784*, 167.

Moffatt, H. K. (1978). *Magnetic field generation in electrically conducting fluids*.

Narayan, R., Igumenshchev, I. V., & Abramowicz, M. A. (2003). Magnetically Arrested Disk: an Energetically Efficient Accretion Flow. *Publication of the Astronomical Society of Japan*, *55*, L69–L72.

Narayan, R., & Yi, I. (1994). Advection-dominated accretion: A self-similar solution. *The Astrophysical Journal*, *428*, L13–L16.

Narayan, R., Yi, I., & Mahadevan, R. (1995). Explaining the spectrum of Sagittarius A* with a model of an accreting black hole. *Nature*, *374*, 623–625.

O'Neill, S. M., Beckwith, K., & Begelman, M. C. (2012). Local simulations of instabilities in relativistic jets - I. Morphology and energetics of the current-driven instability. *Monthly Notices of the Royal Astronomical Society*, *422*, 1436–1452.

Papaloizou, J. C. B., & Pringle, J. E. (1984). The dynamical stability of differentially rotating discs with constant specific angular momentum. *Monthly Notices of the Royal Astronomical Society*, *208*, 721–750.

Parker, E. N. (1955). The Formation of Sunspots from the Solar Toroidal Field. *The Astrophysical Journal*, *121*, 491.

Pessah, M. E., Chan, C.-k., & Psaltis, D. (2007). Angular Momentum Transport in Accretion Disks: Scaling Laws in MRI-driven Turbulence. *The Astrophysical Journal Letters*, *668*, L51–L54.

Pessah, M. E., & Goodman, J. (2009). On the Saturation of the Magnetorotational Instability Via Parasitic Modes. *The Astrophysical Journal Letters*, *698*, L72–L76.

Piran, T. (1978). The role of viscosity and cooling mechanisms in the stability of accretion disks. *The Astrophysical Journal*, *221*, 652–660.

Pringle, J. E. (1981). Accretion discs in astrophysics. *Annual Review of Astronomy and Astrophysics*, *19*, 137–162.

Quataert, E. (2003). Radiatively Inefficient Accretion Flow Models of Sgr A*. *Astronomische Nachrichten Supplement*, *324*, 435–443.

Quataert, E., Dorland, W., & Hammett, G. W. (2002). The Magnetorotational Instability in a Collisionless Plasma. *The Astrophysical Journal*, *577*, 524–533.

Rembiasz, T., Obergaulinger, M., Cerdá-Durán, P., Müller, E., & Aloy, M. A. (2016). Termination of the magnetorotational instability via parasitic instabilities in core-collapse supernovae. *Monthly Notices of the Royal Astronomical Society*, *456*, 3782–3802.

Riquelme, M. A., Quataert, E., Sharma, P., & Spitkovsky, A. (2012). Local Two-dimensional Particle-in-cell Simulations of the Collisionless Magnetorotational Instability. *The Astrophysical Journal*, *755*, 50.

Sano, T., & Inutsuka, S.-i. (2001). Saturation and Thermalization of the Magnetorotational Instability: Recurrent Channel Flows and Reconnections. *The Astrophysical Journal Letters*, *561*, L179–L182.

Sano, T., Inutsuka, S.-i., Turner, N. J., & Stone, J. M. (2004). Angular Momentum Transport by Magnetohydrodynamic Turbulence in Accretion Disks: Gas Pressure Dependence of the Saturation Level of the Magnetorotational Instability. *The Astrophysical Journal*, *605*, 321–339.

Sano, T., & Stone, J. M. (2002). The Effect of the Hall Term on the Nonlinear Evolution of the Magnetorotational Instability. I. Local Axisymmetric Simulations. *The Astrophysical Journal*, *570*, 314–328.

Sądowski, A. (2009). Slim Disks Around Kerr Black Holes Revisited. *The Astrophysical Journal Supplement Series*, *183*, 171–178.

Schödel, R., Ott, T., Genzel, R., Hofmann, R., Lehnert, M., Eckart, A., Mouawad, N., Alexander, T., Reid, M. J., Lenzen, R., Hartung, M., Lacombe, F., Rouan, D., Gendron, E., Rousset, G., Lagrange, A.-M., Brandner, W., Ageorges, N., Lidman, C., Moorwood, A. F. M., Spyromilio, J., Hubin, N., & Menten, K. M. (2002). A star in a 15.2-year orbit around the supermassive black hole at the centre of the Milky Way. *Nature*, *419*, 694–696.

Schreiber, M. R., Hameury, J.-M., & Lasota, J.-P. (2003). Delays in dwarf novae I: The case of SS Cygni. *Astronomy and Astrophysics*, *410*, 239–252.

Shakura, N. I., & Sunyaev, R. A. (1973). Black holes in binary systems. Observational appearance. *Astronomy and Astrophysics*, *24*, 337–355.

Sharma, P., Hammett, G. W., Quataert, E., & Stone, J. M. (2006). Shearing Box Simulations of the MRI in a Collisionless Plasma. *The Astrophysical Journal*, *637*, 952–967.

Shirakawa, K., & Hoshino, M. (2014). Asymmetric evolution of magnetic reconnection in collisionless accretion disk. *Physics of Plasmas*, *21*, 052903.

Shu, C.-W., & Osher, S. (1988). Efficient Implementation of Essentially Non-oscillatory Shock-Capturing Schemes. *Journal of Computational Physics*, *77*, 439–471.

Simon, J. B., Beckwith, K., & Armitage, P. J. (2012). Emergent mesoscale phenomena in magnetized accretion disc turbulence. *Monthly Notices of the Royal Astronomical Society*, *422*, 2685–2700.

Simon, J. B., & Hawley, J. F. (2009). Viscous and Resistive Effects on the Magnetorotational Instability with a Net Toroidal Field. *The Astrophysical Journal*, *707*, 833–843.

Smak, J. (1999). Dwarf Nova Outbursts. III. The Viscosity Parameter alpha. *Acta Astronomica*, *49*, 391–401.

Smak, J. I. (1998). Dwarf Nova Outbursts. I. The UV Delay. *Acta Astronomica*, *48*, 677–693.

Snyder, P. B., Hammett, G. W., & Dorland, W. (1997). Landau fluid models of collisionless magnetohydrodynamics. *Physics of Plasmas*, *4*, 3974–3985.

Spitzer, L. (1956). *Physics of Fully Ionized Gases*.

Stone, J. M., & Gardiner, T. A. (2010). Implementation of the Shearing Box Approximation in Athena. *The Astrophysical Journal Supplement Series*, *189*, 142–155.

Stone, J. M., Gardiner, T. A., Teuben, P., Hawley, J. F., & Simon, J. B. (2008). Athena: A New Code for Astrophysical MHD. *The Astrophysical Journal Supplement Series*, *178*, 137–177.

Stone, J. M., Hawley, J. F., Gammie, C. F., & Balbus, S. A. (1996). Three-dimensional Magnetohydrodynamical Simulations of Vertically Stratified Accretion Disks. *The Astrophysical Journal*, *463*, 656.

Stone, J. M., & Norman, M. L. (1994). Numerical simulations of magnetic accretion disks. *The Astrophysical Journal*, *433*, 746–756.

Suresh, A., & Huynh, H. T. (1997). Accurate Monotonicity-Preserving Schemes with Runge Kutta Time Stepping. *Journal of Computational Physics*, *136*, 83–99.

Suzuki, T. K., & Inutsuka, S.-i. (2014). Magnetohydrodynamic Simulations of Global Accretion Disks with Vertical Magnetic Fields. *The Astrophysical Journal*, *784*, 121.

Tassoul, J.-L. (1978). *Theory of rotating stars*.

Tassoul, J.-L. (2000). *Stellar Rotation*.

Tchekhovskoy, A., Narayan, R., & McKinney, J. C. (2011). Efficient generation of jets from magnetically arrested accretion on a rapidly spinning black hole. *Monthly Notices of the Royal Astronomical Society*, *418*, L79–L83.

Tóth, G. (2000). The $\nabla \cdot B = 0$ Constraint in Shock-Capturing Magnetohydrodynamics Codes. *Journal of Computational Physics*, *161*, 605–652.

Velikov, E. P. (1959). Stability of an ideally conducting liquid flowing between cylinders rotating in a magnetic field. *Soviet Physics Journal of Experimental and Theoretical Physics*, *36*, 995.

Wang, L., Hakim, A. H., Bhattacharjee, A., & Germaschewski, K. (2015). Comparison of multi-fluid moment models with particle-in-cell simulations of collisionless magnetic reconnection. *Physics of Plasmas*, *22*, 012108.

Warner, B. (2003). *Cataclysmic Variable Stars*.

Winters, W. F., Balbus, S. A., & Hawley, J. F. (2003). Chaos in turbulence driven by the magnetorotational instability. *Monthly Notices of the Royal Astronomical Society*, *340*, 519–524.

Wollman, E. R., Geballe, T. R., Lacy, J. H., Townes, C. H., & Rank, D. M. (1977). NE II 12.8 micron emission from the galactic center. II. *The Astrophysical Journal Letters*, *218*, L103–L107.

Yin, L., & Winske, D. (2003). Plasma pressure tensor effects on reconnection: Hybrid and Hall-magnetohydrodynamics simulations. *Physics of Plasmas*, *10*, 1595–1604.

Zdziarski, A. A., Gierliński, M., Mikołajewska, J., Wardziński, G., Smith, D. M., Harmon, B. A., & Kitamoto, S. (2004). GX 339-4: the distance, state transitions, hysteresis and spectral correlations. *Monthly Notices of the Royal Astronomical Society*, *351*, 791–807.

Zhu, Z., Stone, J. M., & Bai, X.-N. (2015). Dust Transport in MRI Turbulent Disks: Ideal and Non-Ideal MHD With Ambipolar Diffusion. *The Astrophysical Journal*, *801*, 81.

Zouganelis, I., Maksimovic, M., Meyer-Vernet, N., Lamy, H., & Issautier, K. (2004). A Transonic Collisionless Model of the Solar Wind. *The Astrophysical Journal*, *606*, 542–554.